Czech Technical University in Prague

Faculty of Electrical Engineering

Doctoral Thesis

August 2013   *Michal Šimůnek*

Czech Technical University in Prague

Faculty of Electrical Engineering
Department of Electromagnetic Field

PROPAGATION CHANNEL MODELING FOR LOW ELEVATION LINKS IN URBAN AREAS

Doctoral Thesis

Michal Šimůnek

Prague, August 2013

Ph.D. Programme: Electrical Engineering and Information Technology
Branch of study: *Radioelectronics*

Supervisor: *Prof. Pavel Pechač, Ph.D.*
Consultant: *Prof. Fernando Pérez-Fontán*

Acknowledgement

Contents

Chapter 1

Introduction

Civilian applications such as air surveillance, remote sensing, and search operations are, nowadays, more often implemented by means of remote controlled Unmanned Aerial Vehicles (UAV). These aircraft are inexpensive and safe to operate. Increased demand for UAV applications correspondingly increase the need for extensive research and development. Most recent research lay in the development of hardware and software systems for developing methods for more precise and effective target acquisition in search operations [1], methods for video gathering [2] or UAV flight modeling [3], however, many of these applications need a transmission link with a ground station to immediately evaluate or store data which the control link cannot provide.

Propagation phenomena study is essential for planning and developing any link; the influence of these phenomena can then be quantified using propagation models. Many propagation models were developed for Satellite and Terrestrial links over the last few decades, however, the links for UAV communications are quite new applications and these links differ in many aspects from satellite or terrestrial links.

One of the main differences is the elevation angle which usually is at about 1 to 5 degrees. Links with this type of geometry can be classified as Low Elevation Links. Another significant difference is the geometrical configuration of the transmitter and receiver where the transmitter is in motion in a homogeneous environment while the receiver is set in a static position in the middle of the scattering environment. For this type of link no propagation models have yet been published, but some research has been done. For example, in [4] an analysis of signal coverage using deterministic model is presented, or, in [5] a UAV measurement and link enhancement possibilities are described. However, it can be stated that the UAV link propagation has not been properly analyzed nor were any models developed for this type of link.

When developing new models, a well-known model for satellite and terrestrial links should first be studied, despite any presumptions of incompatibility with low elevation links, as these models are based on extensive knowledge of propagation phenomena, yet simplified using several approximations to be suitable for these particular applications. These approximations are assumed to be the main reason of incompatibility then the propagation theory should be studied from the very beginning, followed by a study of approximations and method applicability and validity for this type of link.

The greatest need for propagation analysis and modeling is in an urban environment as it is highly inhomogeneous and many obstacles can obstruct the link. The simplified geometry of this link in urban areas is shown in Fig. 1.1.
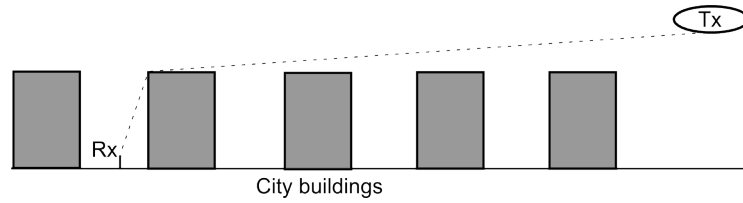
Figure 1.1: Low elevation link example

From the perspective of applications, low elevation links are considered as links with a "nomadic user": the receiver is placed in a static position while in use, but the position can change. In this work only narrow-band mechanisms, those relevant to UAV links at UHF, will be taken into account.

In chapter two the phenomena affecting signal propagation are presented together with analytical methods and subsequently known models of signal propagation for satellite and terrestrial links. Chapter three describes the goals of this work while the main body of this work lies in following chapters. In chapter four a new path-loss model for UAV links is developed and validated while in chapter five a statistical analysis of the propagation channel is performed, together with the development of a time-series generator for this type of link. Chapter six is related to enhancing the UAV link reliability and presents an analysis of the feasibility and effectiveness of diversity methods. The conclusions are presented in chapter seven.

Chapter 2

Signal propagation modeling

Phenomena affecting signal propagation, relevant to UAV links, are presented in this chapter followed by a description of the methods to quantify and model these phenomena. Generally, the link can be analyzed from two points of view: Either, studied in a way of average received power, where a mechanism's effect on the loss of power from transmitter to receiver are analyzed over a sufficiently long period of time, or, the link can be studied in a way of received power time variations where the speed of envelope variations and amplitude distribution in time are analyzed.

2.1   Phenomena affecting signal propagation

As the signal is propagated through the environment several physical mechanisms influence its average power and received spectrum. Moreover, they can change its phase and polarization indirectly causing additional attenuation. In this section the mechanisms which have the most influence on the propagated signal in UAV links are presented.

2.1.1   Reflection

If the wave which is propagating in one environment encounters an infinitely large boundary with another environment with different properties, part of the wave reflects back and another part transmits to the other medium [6]. In a real environment the boundaries are not infinite in size, however, if the boundary - reflecting surface is smooth and significantly larger than the wavelength, the geometry of reflection and transmission can be given by geometrical optics i.e. Snell's laws and the amount of transmitted and reflected field strength is given by the difference in the properties of the media. It can be quantified using reflection and transmission coefficients Γ and T. The situation of TE wave reflection is depicted in Fig. 2.1.
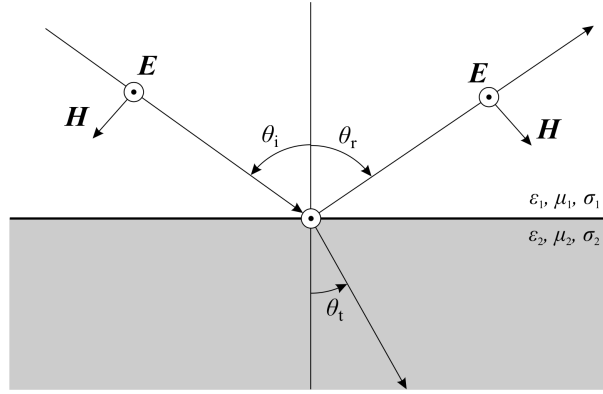
Figure 2.1: TE polarized plane wave reflection and transmission on the boundary of two different environments

The medium is characterized by permittivity ε, permeability μ and electrical conductivity σ and for TE wave the coefficients are defined as [7]:

$$\Gamma_{\mathrm{E}} = \frac{Z_2 \cos(\theta_{\mathrm{i}}) - Z_1 \cos(\theta_{\mathrm{t}})}{Z_2 \cos(\theta_{\mathrm{i}}) + Z_1 \cos(\theta_{\mathrm{t}})} \tag{2.1}$$

and

$$T_{\mathrm{E}} = \frac{2 Z_2 \cos(\theta_{\mathrm{i}})}{Z_2 \cos(\theta_{\mathrm{i}}) + Z_1 \cos(\theta_{\mathrm{t}})} \tag{2.2}$$

Where Z is a wave impedance

And for TM polarized waves (Fig. 2.2) these coefficients are defined as:

$$\Gamma_{\mathrm{M}} = \frac{Z_2 \cos(\theta_{\mathrm{t}}) - Z_1 \cos(\theta_{\mathrm{i}})}{Z_2 \cos(\theta_{\mathrm{t}}) + Z_1 \cos(\theta_{\mathrm{i}})} \tag{2.3}$$

and

$$T_{\mathrm{M}} = \frac{2 Z_2 \cos(\theta_{\mathrm{i}})}{Z_2 \cos(\theta_{\mathrm{t}}) + Z_1 \cos(\theta_{\mathrm{i}})} \tag{2.4}$$
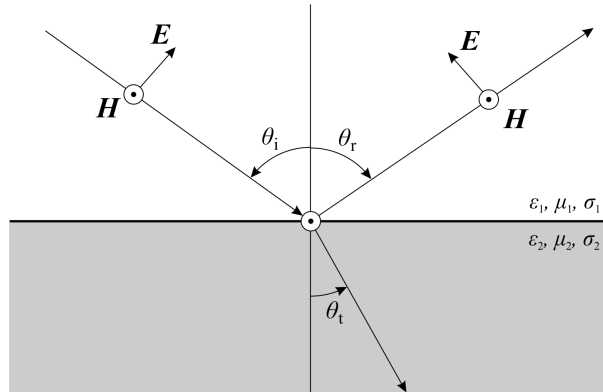
Figure 2.2: TH polarized plane wave reflection and transmission on the boundary of two different environments

For a general angle between $\boldsymbol{E}$ and the boundary plane, a superposition of both polarizations is needed.

2.1.2 Scattering

Scattering occurs when a wave is spread in several directions after encountering an object significantly smaller than its wavelength. This is also observed when a plane wave encounters a rough surface where each small piece has a different incident angle. The rough surface scattering is considered in building reflection. An example of this modeling is a three-component model [8] (Fig. 2.3). It decomposes the reflection into three parts: Specular reflection from a smooth building face; back scattering reflection which is a double reflection on smooth window or door edges; diffuse scattering which simplifies the rough surface of a building face by a limited area of small plates used as sources whose contribution at the point studied is computed using the expression for the unit-surface radar cross section [9]. It should be noted that the point studied must be located in a far-field.
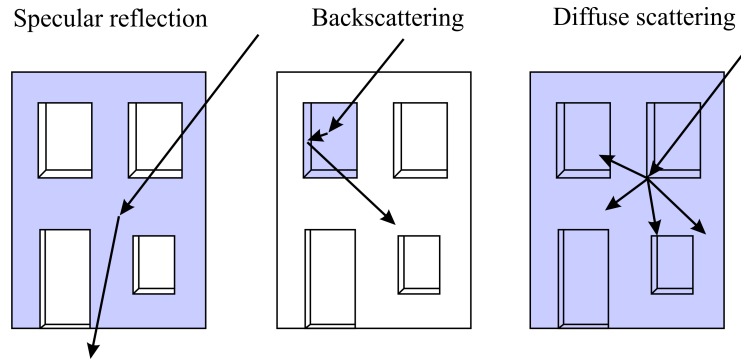
Figure 2.3: Decomposition of building face into three scattering components

2.1.3 Diffraction

Huygens' principle

The reflection theory assumes that reflection surfaces are infinite in size, or, at least significantly larger than the wavelength of the incident wave. Situations where a wave encounters the edge of a finite large obstacle can be described using Huygens' principle. This principle assumes that the wavefront can be considered as an infinite number of sources of wavelets, and, at each point in front of the waveform all these sources are added to make another source of wavelet. An illustration of Huygens' principle can be found in Fig. 2.4.
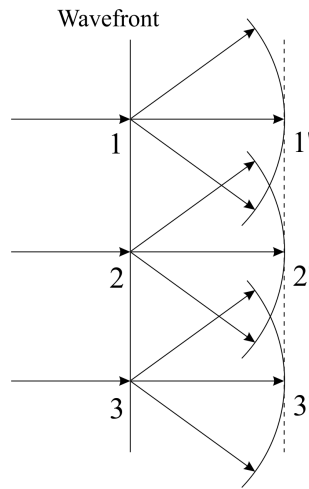
Figure 2.4: Huygens' principle demonstration on plane wave propagation

In the illustration the wavefront is composed of three sources, infinitely close together, 1, 2 and 3. A new source arises from the contributions of all three sources at point 2' and together with new sources 1' and 3' forms a new wavefront.

Assume that a wavefront encounters a finitely long, but impenetrable obstacle. Using simple ray theory, it can be stated that wavelets above the obstacle continue in their direction while other wavelets are absorbed or reflected from the obstacle. However, according to the Huygens' principle the wavelets above the obstacle propagate to all directions including the shadowed area behind the obstacle (Fig. 2.5). The wave "bending" around the edge is called Diffraction.
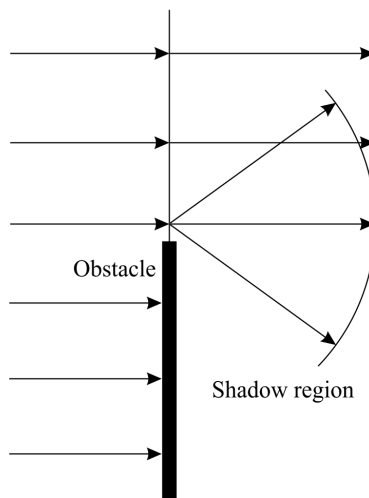
Figure 2.5: Plane wave encountering the edge of an obstacle

Fresnel Integrals approach

The basic method of approach for modeling diffraction on a thin, perfectly absorbing screen (called a "knife-edge"), Fresnel diffraction or Fresnel integrals[10] is presented first.

First assume a general wavefront in open space. According to Huygens' principle it is composed of an infinite number of equal sources of electromagnetic waves. At one point in front of the waveform, the rays from all sources will be summed. In this approximation, the only difference in phase, the different path-length, is taken into account and other differences are omitted. If a contributing phasor from each source is plotted into a phasor diagram, it will have the shape of a spiral as the contributing phasors rotate with increasing phase difference. This shape is called the Cornu spiral (Fig. 2.6). The center of the spiral corresponds to the ray with the shortest path-distance from waveform to the studied point. In the end it converges into two points $0.5 + j0.5$ and $-0.5 - j0.5$.
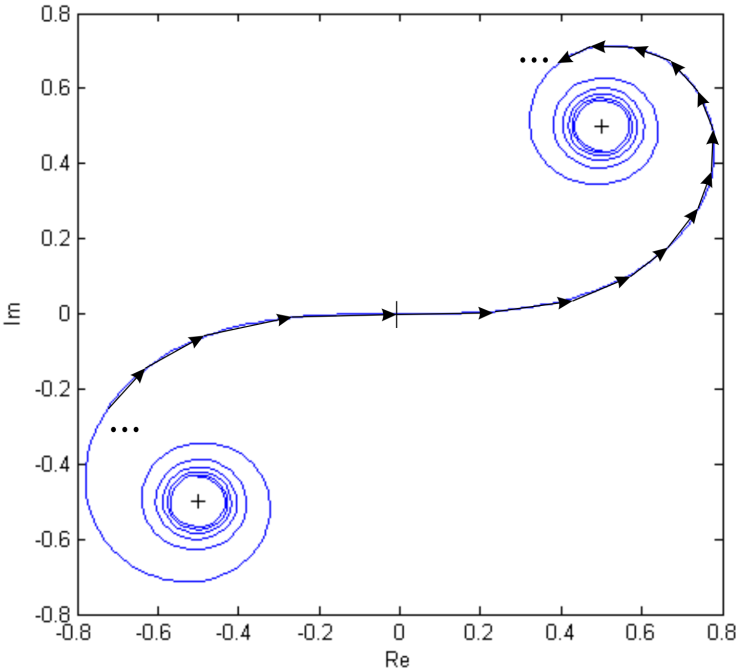
Figure 2.6: The Cornu spiral

A contribution from one source yields a basic element in a Cornu spiral δs. It can be decomposed into two components: $\delta s \cos(\phi)$ and $\delta s \sin(\phi)$ (Fig. 2.7). The phase difference of one contributor ϕ is given by an additional path-length of each ray Δd [10]
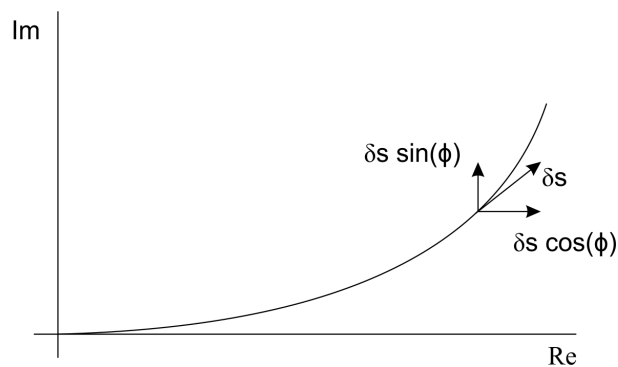
Figure 2.7: Basic contribution along the Cornu spiral

An infinite integration of all elements δs yields the total sum of contributions E_0. In the case of unobstructed propagation, the field strength in studied point E_0 is then:

$$E_0 = \int_{-\infty}^{\infty} \exp(j\phi)ds = 1 + j \tag{2.5}$$

However, in case of diffraction, a integration is limited from one side by the obstacle. Now let us assume that the wavefront is above an obstacle as in Fig. 2.5. A geometry of whole link can be found in Fig. 2.8.
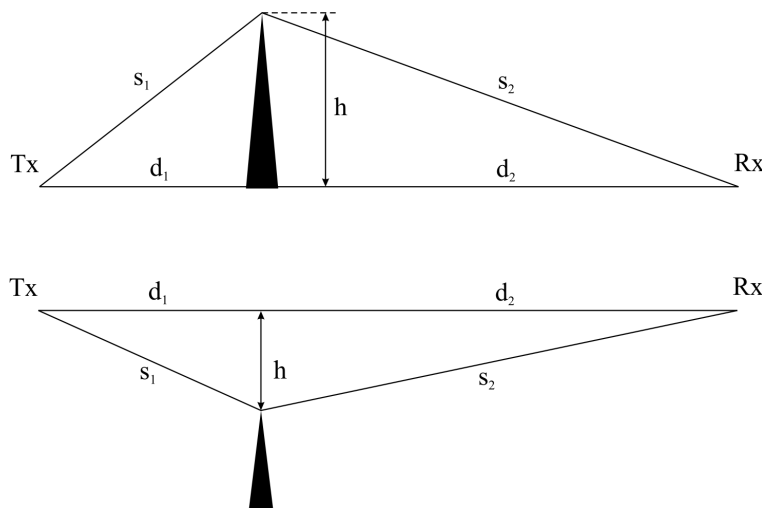
Figure 2.8: Geometry of Fresnel diffraction

Now the Δd, under a condition that $h \ll d_1, d_2, \lambda$, is expressed using parabolic approximation:

$$\Delta d = \frac{h^2}{2d} \tag{2.6}$$

Then the phase difference is given by:

$$\phi = \frac{2\pi\Delta d}{\lambda} = \frac{\pi h^2}{\lambda d} \tag{2.7}$$

10

So, lets define a dimensionless parameter ν which is a curved length along the spiral from its center [10]. It is defined using parabolic approximation as:

$$\nu = 2\sqrt{\frac{\Delta d}{\lambda}} = h\sqrt{\frac{2}{\lambda}\left(\frac{1}{d_1} + \frac{1}{d_2}\right)} \tag{2.8}$$

Hence the phase difference can be written as:

$$\phi = \frac{\pi\nu^2}{2} \tag{2.9}$$

Therefore, the total sum of contributions up to ν is written as:

$$F(\nu) = \int_0^\nu \exp(j\frac{\pi s^2}{2})ds \tag{2.10}$$

Or, using the decomposition by:

$$F(\nu) = C(\nu) + jS(\nu) \tag{2.11}$$

where

$$C(\nu) = \int_0^\nu \cos(\frac{\pi s^2}{2})ds \quad S(\nu) = \int_0^\nu \sin(\frac{\pi s^2}{2})ds \tag{2.12}$$

Then the ν is used as the top of an obstacle and the sum of contributions above the obstacle, which gives the field strength at the point studied, is expressed as follows:

$$E = \int_\nu^\infty \exp(j\frac{\pi s^2}{2})ds \tag{2.13}$$

Assuming that the value of the Cornu spiral for infinity is $0.5 + j0.5$. The field strength E can be also expressed using finite integral as [10]:

$$E = (0.5 + j0.5) - \int_0^\nu \exp(j\frac{\pi s^2}{2})ds = [0.5 - C(\nu)] + j[0.5 - S(\nu)] \tag{2.14}$$

Finally, the field strength relative to free-space is given by:

$$E_{\mathrm{f}} = \frac{E}{E_0} = \frac{[1 - C(\nu) - S(\nu)] + j[-C(\nu) - S(\nu)]}{2} \tag{2.15}$$

In Fig. 2.9 the E_f in logarithmic units - path-gain due to diffraction - is depicted as a function of ν. Note that values above zero are only theoretical and were not observed in measurements.
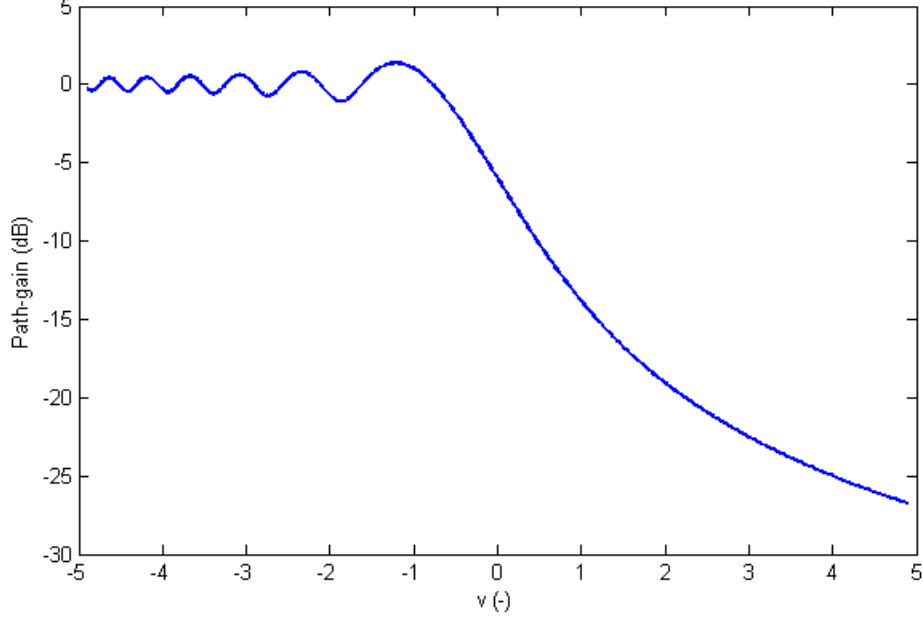
Figure 2.9: Path-gain as a function of parameter ν

It can be seen that the edge causes a diffraction loss even if it does not fully obstruct the line of sight as the field strength is composed from only a part of the wavelets. This leads to a definition of discrete circular zones around the line of sight, called Fresnel zones, for classifying the approaching obstacle to the line of sight. The greatest influence on the link has the zone closest to the line of sight the first Fresnel zone. The radius of Fresnel zones is given by the following formula:

$$F_{\mathrm{n}} = \sqrt{\frac{n\lambda d_1 d_2}{d_1 + d_2}} \tag{2.16}$$

where n is the number of zones and d_1 and d_2 distances from the obstacle.

It can be difficult to fast compute the entire integration process of Fresnel diffraction. For the purposes of simplification in ITU-R Recommendation [11] an approximation of path-gain for $\nu > -0.78$ is presented

$$L(\mathrm{dB}) = 6.9 + 20\log(\sqrt{(\nu - 0.1)^2 + 1} + \nu - 0.1) \tag{2.17}$$

In addition, Lee in his work [12] presented other widely used approximations:

$$
\begin{array}{lll}
L(\mathrm{dB}) = 0 & \nu \leq -1 & (2.18) \\
L(\mathrm{dB}) = 20\log(0.5 - 0.62\nu) & -1 < \nu \leq 0 & (2.19) \\
L(\mathrm{dB}) = 20\log(0.5\exp(-0.95\nu)) & 0 < \nu \leq 1 & (2.20) \\
L(\mathrm{dB}) = 20\log(0.4 - \sqrt{0.1184 - (-0.1\nu + 0.38)^2}) & 1 < \nu \leq 2.4 & (2.21) \\
L(\mathrm{dB}) = 20\log\left(\dfrac{0.225}{\nu}\right) & 2.4 \leq \nu & (2.22)
\end{array}
$$

12

A general obstacle can have various shapes. One of the possible ways to approximate an obstacle is to use the afore-mentioned knife-edge. Other possibilities are described in ITU-R recommendation P.526 [11] where a rounded obstacle or finite-wide edge (wedge) solution can also be found.

More precise methods are Ray-based diffraction methods, such as the Geometrical theory of diffraction (GTD) and the Uniform theory of diffraction (UTD). The concept is based on the assumption of direct, reflected and diffracted rays. While direct and reflected rays are treated by geometrical optics, the diffracted ray is given by a diffraction coefficient which is set for each polarization [10]. The UTD includes Fresnel integrals in the diffraction coefficient.

Multiple diffraction

Solving a diffraction with more obstacles is difficult for after encountering the obstacle, the wave is no longer consistent in space. Therefore, in many solutions the knife-edge simplification is used. A method where Fresnel integrals are computed using repeated integrals of error function was presented by Vogler [13]. Otherwise, for simplifying computations several approximation methods were developed [14]. Three example methods are described below:

Bullington's equivalent knife-edge   This method replaces several obstacles by one knife-edge whose height is given by the intersection of lines: the transmitter-top of the first obstacle and the top of the last obstacle the receiver (Fig. 2.10) However, this method ignores the obstacles below the intersection, thus giving overly optimistic results.
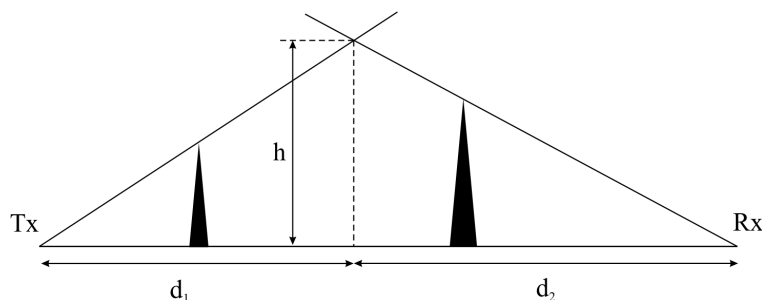
Figure 2.10: Bullington's equivalent knife-edge method

The Epstein-Peterson method   In this method a propagation path is divided into particular subpaths, each of which has one knife-edge diffraction and their power sum gives the total loss caused by diffraction. The sub-path is given by the single obstacle whose height is computed from the connection between two adjacent obstacles. (Fig. 2.11)
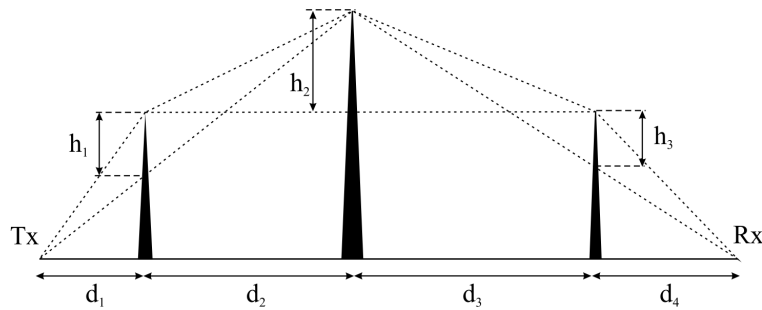
Figure 2.11: The Epstein-Peterson method

The Deygout method   The first step in the Deygout method is choosing a dominant edge, which is the obstacle with the highest parameter ν. The diffraction loss caused only by this obstacle is then summed with the loss from other obstacles whose height is given by the line between the transmitter or receiver and the top of the dominant edge (Fig. 2.12). If there are more obstacles between the dominant edge and transmitter or receiver than another dominant edge among these secondary edges is chosen and the loss is expressed using the same principles as for the general dominant edge recursively. This method shows good agreement, especially in cases with one dominant obstacle where other methods are too optimistic. On the other hand, for a large number of obstacles this method's results are too pessimistic.
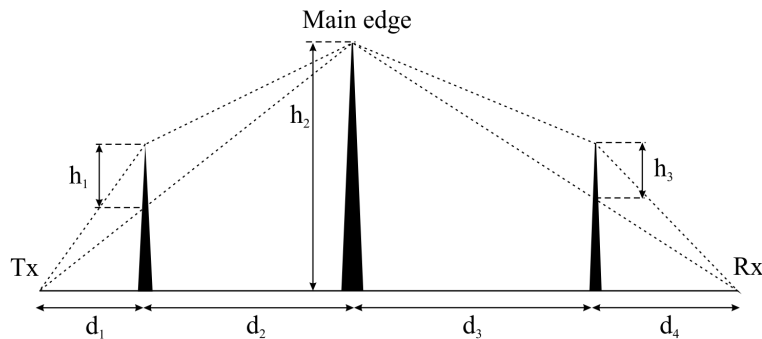
Figure 2.12: The Deygout method

2.1.4   Shadowing

As the receiver is moving along the buildings in an urban area or the trees in a rural environment, a direct line between the transmitter and receiver can be broken off, hence, the received power temporarily decreases. This phenomenon is called shadowing. Shadowing causes drops in received power, depending on motion speed, that can last several seconds. If the signal is shadowed by an impenetrable obstacle where the drop level is several tens of dB lower, it is usually called "blockage" instead.

In a satellite system shadowing causes serious difficulties due to a tense link budget. The blockage conditions usually mean that the link is broken. Many studies were performed for tree shadowing along roads, but an even more complicated situation arises in urban areas where shadowing and blockage occur more often. In land mobile satellite

models shadowing and blockage is usually modeled as a cause of amplitude distribution shape (section 2.3.1) or by a probability of occurrence (State oriented models in section 2.4.4). In terrestrial mobile systems the link is usually shadowed most of the receiving time, so the probability of occurrence is not as important, therefore, shadowing is usually modeled as variations in average loss.

2.1.5 Multipath fading

Another cause of variations is multipath propagation. The signal from the transmitter can travel by several routes, reflected from obstacles or diffracted. The signal from each route comes to the receiver, each with a different phase due to different path length and with different strength. They constructively or destructively interfere and their sum creates variations in received signal. This phenomenon is called multipath fading.

The speed and shape of variations is dependent on the number of rays from which the signal is composed. If there are a few strong rays, the variations will have deep fades and be Rayleigh distributed (see subsection 2.3.1), whereas if the signal is composed from many weaker rays, the variations will be normally distributed around the average received signal.

A demonstrative illustration of path-gain, where both shadowing and multipath fading with normal distribution are depicted, is shown in Fig. 2.13 (transition effects were omitted).
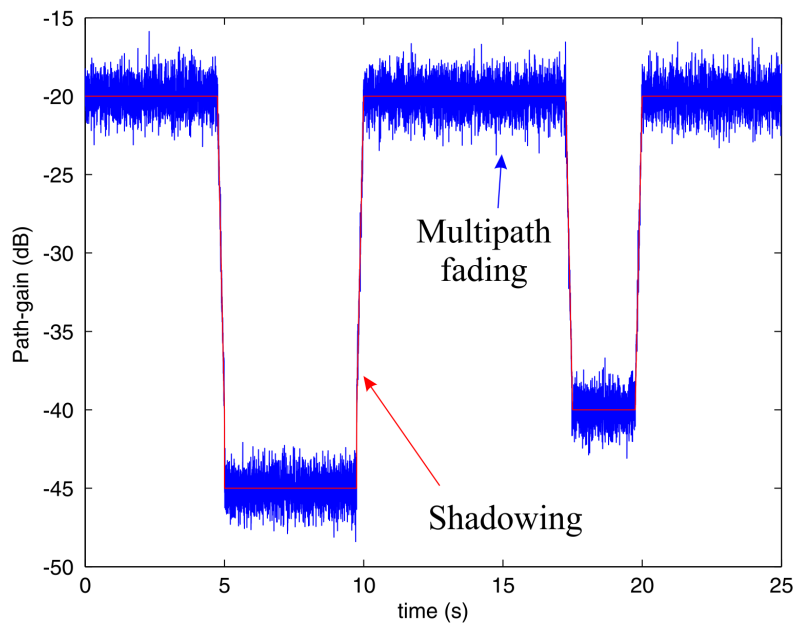
Figure 2.13: An illustration of Shadowing and Multipath fading

2.1.6 Doppler shift

Another phenomenon which influences the frequency is the Doppler shift and it can be defined as [15]. Assume a transmitter transmitting a harmonic signal is placed at a static

position and a receiver in motion towards the transmitter. The received frequency will be shifted up as the receiver receives the waves faster due to its motion towards them. Similarly when the receiver moves from the transmitter, the received frequency is shifted down. Generally, the amount of shift will be given by the speed of the receiver v, the wavelength λ and by the angle of motion between receiver and transmitter α.

$$F_{\mathrm{d}} = \frac{v}{\lambda} \cos \alpha = f_{\mathrm{c}} \frac{v}{c} \cos \alpha = f_{\mathrm{m}} \cos \alpha \tag{2.23}$$

where the f_{m} is defined as the maximum Doppler shift for $\alpha = 0$.

2.1.7 Doppler spread

Assume there is a random propagation environment between the transmitter and receiver which allows several propagation paths. The transmitted signal arrives to the receiver from several different paths i.e. different angles. Therefore, each path will suffer from a different Doppler shift, so instead of one frequency there is a spread of frequencies where the receiver is placed. This phenomenon is called Doppler spread (Fig. 2.14).
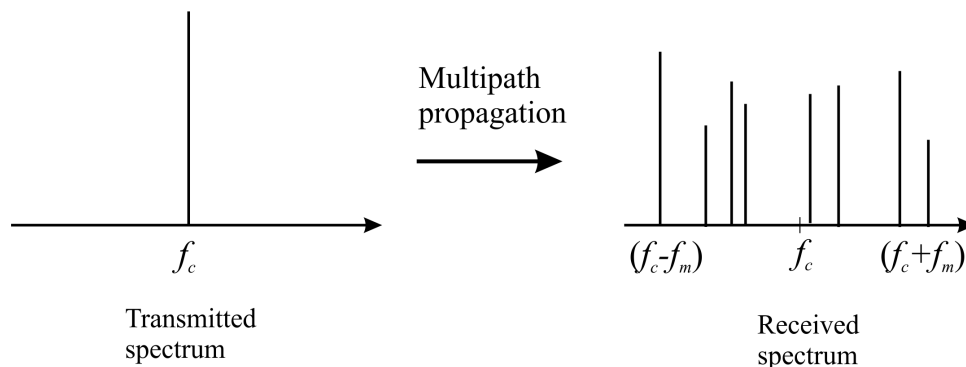
Figure 2.14: Effect of Doppler spread on transmitted impulse signal

2.2 Path-loss modeling in urban areas at UHF

Path-loss models estimate the average loss caused by phenomena described in section 2.1. These models are mainly used for terrestrial links because the link budget in satellite links does not allow any shadowed or blocked conditions for any substantial amount of time.

There are basically three types of path-loss models: Deterministic models which use the basic physical theories of wave propagation and give the most accurate results providing a detailed environment information is available; Empirical path-loss models which, in general, express path-loss by the mathematical regression of measured path-loss as a function of distance additionally extended by coefficients for various frequencies or environment types; Semi-empirical, or semi-deterministic models, which combines these two approaches. They use the deterministic modeling methods using several approximations for simplifying the expression. Additionally, in some models, the parameters are expressed in a empirical way for various environments and situations.

2.2.1 Deterministic path-loss models

So called Deterministic models use unapproximated theories, however, for computational feasibility, the scenarios are usually simplified. Integral equation methods and Parabolic equation methods use the wave equation and search for a path-loss function for every point between the transmitter and receiver [15]. These methods can sufficiently model the influence of terrain profile between the transmitter and receiver but the UAV link is assumed to be influenced mainly by the local environment so these methods are not suited for this type of link.

Better suited methods for local environment modeling are Optical models (Ray-tracing, Ray-launching), where a theory of diffraction and reflection, together with geometrical optics principles, are applied to a finite number of rays launched and tracked from the receiver. A detailed model of obstacle shapes and their electrical parameters is needed, together with high computational power and time [14].

2.2.2 Empirical path-loss models

A large number of empirical models were developed for various environments, geometries of link and other link parameters. These models can provide quickly and easily estimate path-loss, but they are only relevant for the environment from which the model was developed. The empirical modeling principle will be presented on well-known models:

COST 231 - Hata model

The basic empirical model is the Hata model and in the COST 231 project an improved Hata model was developed [16]. The Hata model was extended to higher frequencies from 1,500 MHz to 2,000 MHz from Okumuras propagation curves analysis. This model is designed for macro-cell units and is purely empirical, so it can be used in cases where only limited information about surrounding terrain is available. The type of terrain is defined by parameter C_m which was added to the basic equation. This model has four parameters: frequency, distance, base station antenna height and mobile station antenna height. The basic path-loss is defined as:

$$L_b = 46.3 + 33.9 \log_{10}(f) - 13.82 \log_{10}(H_{bs}) - a_{hm} + (44.9 - 6.55 \log_{10}(H_{bs})) \log_{10}(d) + C_m \tag{2.24}$$

where:

$$a_{hm} = (1.1 \log_{10} f - 0.7) H_{mt} - (1.56 \log_{10}(f) - 0.8) \tag{2.25}$$

and $C_m = 0$ dB for medium-sized city and suburban centers with medium tree density or $C_m = 3$ dB for metropolitan centers, f is frequency in MHz, d is distance in km, H_{bs} is base station height above ground in meters and H_{mt} is receiver station height above ground in meters.

This model is restricted to:

$$f : 1500...2000 \text{ MHz}$$
$$H_{\text{bs}} : 30...200 \text{ m}$$
$$H_{\text{mt}} : 1...10 \text{ m}$$
$$d : 1...20 \text{ km}$$

Stanford University Interim SUI model

The Stanford University Interim, SUI, model [17] is more suitable for smaller cells, lower base station antenna heights and higher frequencies. This model is appropriate for three types of terrain: Type A, hilly terrain with moderate to heavy tree densities with maximum path-loss; Type B, mostly flat terrain with moderate to heavy tree densities or hilly terrain with light tree densities; Type C, flat terrain with light tree densities with minimum path-loss. The model was derived from measurements at 1.9 GHz with a receiver antenna height of 2 m and is restricted to these conditions. This model has similar parameters as Hata plus it uses some statistical parameters. The basic equation of path loss in dB as a function of distance for $d \geq d0$ is:

$$PL = A + 10\gamma log_{10}\left(\frac{d}{d_0}\right) + s \tag{2.26}$$

where A is a free space loss parameter:

$$A = 20 \log_{10}\left(\frac{4\pi d_0}{\lambda}\right) \tag{2.27}$$

with $d_0 = 100$m and λ is wavelength in meters and γ is a path loss exponent defined as:

$$\gamma = \left(a - bh_b + \frac{c}{h_{\text{b}}}\right) + x\sigma_\gamma \tag{2.28}$$

where h_{b} is base station height in meters with restriction from 10 to 80 meters. The entire parentheses content is the mean of γ. σ_γ is the standard deviation of γ. a, b, c and σ_γ are constants derived from measurement. Variable x has zero-mean and Gaussian distribution. Parameter s is a shadow fading component and it has also zero mean and Gaussian distribution. In the case of path-loss modeling, averaged over time, as a function of the distance and the elevation angle, there is no need to use any statistical variables, therefore, it is possible to simplify this model to this equation:

$$PL = A + 10\gamma \log_{10}\left(\frac{d}{d_0}\right) + X_{\text{mt}} \quad d \geq d_0 \tag{2.29}$$

where:

$$\gamma = \left(a - bh_{\text{b}} + \frac{c}{h_{\text{b}}}\right) \tag{2.30}$$

and X_{mt} is an extension for different mobile station antenna heights expressed for terrain types A and B as:

$$X_{\mathrm{mt}} = -10.8 \log_{10} \left(\frac{H_{\mathrm{mt}}}{2000} \right) \tag{2.31}$$

and for Terrain types C:

$$X_{\mathrm{mt}} = -20 \log_{10} \left(\frac{H_{\mathrm{mt}}}{2000} \right) \tag{2.32}$$

where H_{mt} is receiver antenna height above street level in meters.

2.2.3   Semi-empirical path-loss models

Empirical models can give fast path-loss estimations. However, in situations where the parameters of obstacles have a higher influence on diffraction - when the obstacles are large and close to the receiver or transmitter - the empirical models can be inaccurate. On the other hand, the most accurate estimation can be given by deterministic models, but there is usually a lack of information regarding obstacle details and the computational time is long. As a compromise between these two approaches many semi-empirical or sometimes semi-deterministic models were presented. They essentially came from a deterministic approach where several approximations of environment and propagation mechanisms are used for simplicity and time efficiency. In some models the influence of some phenomena is expressed using purely empirical formulas. Semi-empirical path-loss models have several advantages: They give insight to physical principles causing the loss; depending on the amount of approximations, they are more versatile for various shapes of obstacles and environments; their parameter ranges can be extended according to theories applied.

Ikegami model

In this approach the Fresnel Integrals theory and reflection theory are applied and approximated for simplicity [18]. This model assumes that the ray from the transmitter propagates to the closest obstacle near the receiver without any additional loss and then from the top of this last obstacle the multipath propagation is approximated by the two strongest rays which propagate in the street corridor to the receiver assumed to be in the center of the street. One propagates directly from the edge of an obstacle to the receiver, the other propagates to the next building behind the receiver and reflects back to the receiver (Fig. 2.15). A diffraction loss on the last obstacle is computed using Fresnel Integrals theory for each ray separately using an approximation for $\nu > 2.4$. The reflection loss is approximated to be constant. These two rays are finally power summed giving the total field strength.
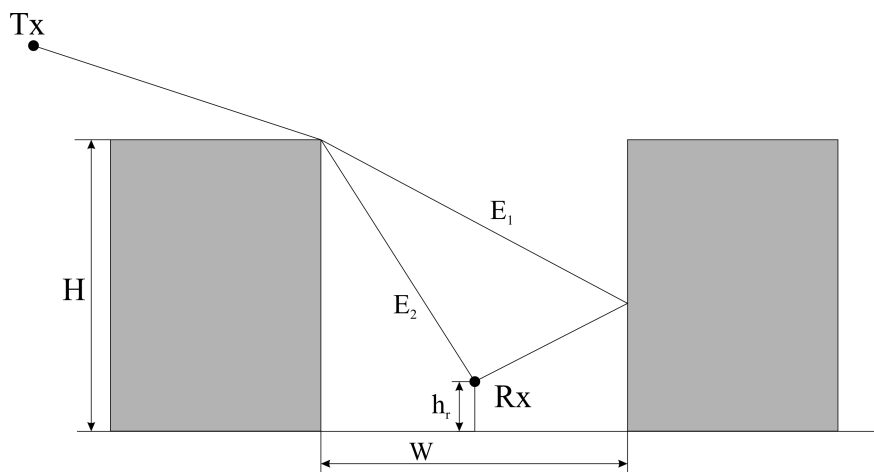
Figure 2.15: The Ikegami model geometry

Additionally, an angle of street orientation was assumed and after several arrangements the final field strength can be expressed in dB as:

$$E = E_0 + 5.8 + 10 \log \left(1 + \frac{3}{L_r^2}\right) + 10 \log W - 20 \log(H - h_r) - 10 \log(\sin \Phi) - 10 \log f \quad (dB)$$

(2.33)

where L_r is the reflection loss in dB, W is the street width in meters, H is the height of the last obstacle above the street level in meters, h_r is the height of a mobile receiver in meters, Φ is an angle of street orientation to the line between the transmitter and receiver and f is a frequency in MHz.

Saunders flat-edge model

In situations where the elevation angle between the last obstacle and the transmitter is low, the sole Ikegami approach is not fully capable of predicting path-loss due to neglecting the loss between the transmitter and the last obstacle. For terrestrial macrocell systems it is standard to compute the diffraction loss for two sections: the diffraction caused by the last obstacle and the diffraction caused by multiple diffraction over the rooftops. A well-used model of this was presented by Saunders as the Flat edge model [15]. In this model the urban environment is simplified to equal-spaced buildings with the same height [10]. The geometry can be found in Fig. 2.16.
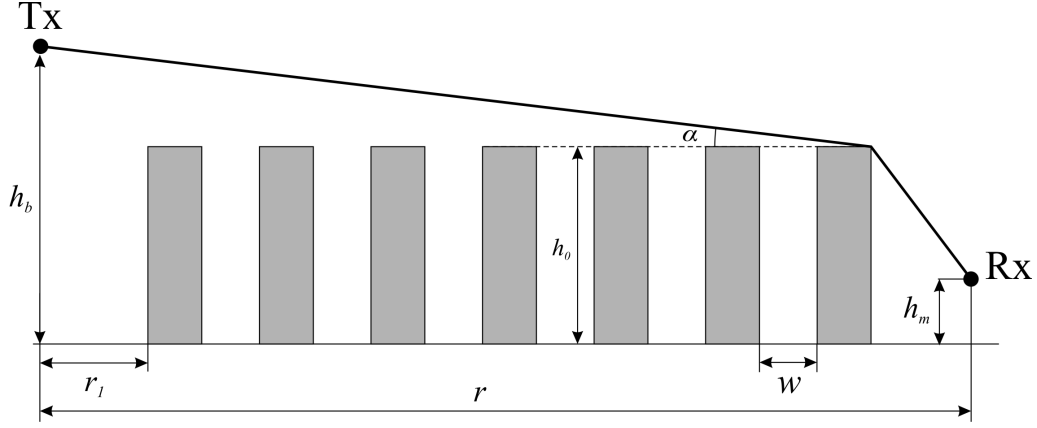
Figure 2.16: Geometry of Flat-edge model

The excess path-loss is given by:

$$L_{\text{ex}} = L_{n-1}(t)L_{\text{ke}} \tag{2.34}$$

where L_{ke} is a loss due to the diffraction over the last obstacle and L_{n-1} is a loss due to multiple diffraction over remaining obstacles. The L_{n-1} can be solved using Fresnel integrals method if only a limited number of obstacles positioned relatively distant from the transmitter ($r_1 \gg nw$) is considered. The L_{n-1} is a function of only one parameter t which is defined as:

$$t = -\alpha\sqrt{\frac{\pi w}{\lambda}} \tag{2.35}$$

Then the multiple diffraction loss is expressed as:

$$L_n(t) = \frac{1}{n}\sum_{m=1}^{n-1} L_m(t)F_{\text{s}}(-jt\sqrt{n-m}) \quad n \geq 1 \quad L_0(t) = 1 \tag{2.36}$$

where

$$F_{\text{s}}(jx) = \frac{e^{-jx^2}}{\sqrt{2j}}\left\{\left[S\left(x\sqrt{\frac{2}{\pi}}\right) + \frac{1}{2}\right] + j\left[C\left(x\sqrt{\frac{2}{\pi}}\right) + \frac{1}{2}\right]\right\} \tag{2.37}$$

where S and C are standard Fresnel integrals. This formula provides a relatively quick solution even for large number of obstacles. For even simpler and faster solution the resulting curve can be approximated by the following formula:

$$L_n(t) = -(c_1 + c_2\log n)\log(-t) - (c_3 + c_4\log n) \tag{2.38}$$

with $c_1 = 3.29$, $c_2 = 9.90$, $c_3 = 0.77$ and $c_4 = 0.26$. This approximation gives results with an accuracy of more than 1.5 dB for $1 \leq n \leq 100$ and $-1 \leq t \leq 0$

With an increasing number of obstacles the loss due to multiple diffraction settles to a constant value. This number n_{s} corresponds to the number of obstacles which influence the first Fresnel zone.

A similar approach was presented in the Walfish-Bertoni model [19] where the power law formula was fitted to settled field results. It uses both approaches: The flat edge model approximations for multiple diffraction and Ikegami model for last obstacle diffraction.

COST 231 Walfish-Ikegami model

Based on the Walfish-Bertoni model, Ikegami approach, and, with several empirical modifications, a Walfish-Ikegami model [16] was developed as another output of the COST-231 project. The path-loss is divided into three parts. They are:

Free-space loss L_0, which relates only to loss, caused by the distance between the receiver and transmitter for $d > 20m$ expressed as:

$$L_0(dB) = 32.4 + 20 \log_{10}(d) + 20 \log_{10}(f) \tag{2.39}$$

where: d is distance in km, f is frequency in MHz.

Roof-top-to-street diffraction L_{rts} is loss which results from multipath propagation on the last segment where a receiver is located. It is defined as:

$$L_{\text{rts}} = -16.9 - 10 \log_{10}(w) + 10 \log_{10}(f) + 20 \log_{10}(\Delta h_{\text{Mobile}}) + L_{\text{Ori}} \tag{2.40}$$

where w is street width in meters, f is frequency in MHz and:

$$\Delta h_{\text{Mobile}} = h_{\text{Roof}} - h_{\text{Mobile}} \tag{2.41}$$

where h_{Roof} is height of last rooftop above street level in meters and h_{Mobile} is height of receiver above street level in meters. L_{Ori} is a part of loss describing the influence of street orientation and is defined as:

$$L_{\text{Ori}} = \begin{cases} -10 + 0.354\phi & \text{for } 0° \leq \phi < 35° \\ 2.5 + 0.075(\phi - 35) & \text{for } 35° \leq \phi < 55° \\ 4.0 - 0.114(\phi - 55) & \text{for } 55° \leq \phi < 90° \end{cases} \tag{2.42}$$

where ϕ is an angle between incident wave and street orientation.

The last part of model is derived from the Walfisch-Bertoni model [19] which was extended for transmitter heights lower than building height. It can be expressed as:

$$L_{\text{msd}} = L_{\text{bsh}} + k_a + k_d \log_{10}(d) + k_f \log_{10}(f) - 9 \log_{10}(b) \tag{2.43}$$

where:

$$L_{\text{bsh}} = \begin{cases} -18 \log(1 + \Delta h_{\text{Base}}) & \text{for } h_{\text{Base}} > h_{\text{Roof}} \\ 0 & \text{for } h_{\text{Base}} \leq h_{\text{Roof}} \end{cases} \tag{2.44}$$

$$k_a = \begin{cases} 54 & \text{for } h_{\text{Base}} > h_{\text{Roof}} \\ 54 - 0.8\Delta h_{\text{Base}} & \text{for } d \geq 0.5 \text{ km and } h_{\text{Base}} \leq h_{\text{Roof}} \\ 54 - 0.8\Delta h_{\text{Base}}d/0.5 & \text{for } d < 0.5 \text{ km and } h_{\text{Base}} \leq h_{\text{Roof}} \end{cases} \tag{2.45}$$

$$k_d = \begin{cases} 18 & \text{for } h_{\text{Base}} > h_{\text{Roof}} \\ 18 - 15\Delta h_{\text{Base}} & \text{for } h_{\text{Base}} \leq h_{\text{Roof}} \end{cases} \tag{2.46}$$

For medium-sized cities and suburban areas with medium tree density the parameter k_f is:

$$k_\mathrm{f} = -4 + 0.7 \left(\frac{f}{925} - 1 \right) \tag{2.47}$$

and for metropolitan centers:

$$k_\mathrm{f} = -4 + 1.5 \left(\frac{f}{925} - 1 \right) \tag{2.48}$$

The total path-loss is given by:

$$L_\mathrm{b}(dB) = L_0 + L_\mathrm{rts} + L_\mathrm{msd} \tag{2.49}$$

This model has these restrictions:

$$f : 800...2000 \, \mathrm{MHz}$$
$$h_\mathrm{Base} : 4...50 \, \mathrm{m}$$
$$h_\mathrm{Mobile} : 1...3 \, \mathrm{m}$$
$$d : 0.02...5 \, \mathrm{km}$$

2.3   Statistical analysis methods

The influence of the phenomena related to signal time variations (shadowing, multipath fading, Doppler shift and Doppler spread) is usually quantified in statistical analysis. Common statistical tools for channel analysis are presented with these analysis methods being used for both terrestrial and satellite links.

2.3.1   Amplitude distribution analysis methods

First, a tool describing the amplitude variations in time are introduced.

The probability density function (PDF) is a function that describes the probability that a random variable will have a given value. It provides useful information about the distribution of a random variable (received envelope) around its mean value. Its integral over the entire space is equal to one. In this work the PDF will be denoted as $p(x)$

The cumulative sum of PDF values gives a cumulative distribution function (CDF). It provides important information on the probability that a random value is less than or equal to a specified ordinate. The given value can be expressed in the form of received power which is often used to quantify the reliability of a link. It is denoted as $F(x)$ and:

$$F(x) = \int_c^x p(t)dt \tag{2.50}$$

where c is the lowest limit of the values of t.

The analyzed signal can have various distributions of received voltage or power. These are usually described by the PDF and CDF and compared with known defined distributions, many of which are described in statistical theory. In this work distributions

presented reflect some physical phenomena, therefore, they are often used in radio wave propagation modeling.

Gaussian or normal distribution

Gaussian distribution (sometimes called normal) [20] occurs when a large amount of slightly important random causes are added according to the central limit theorem. In radiowave propagation this situation occurs as a result of multipath propagation where the received signal is composed of a large amount of weak contributions. Its PDF can be expressed as:

$$p(x) = \frac{1}{\sigma\sqrt{2\pi}} \exp\left[-\frac{1}{2}\left(\frac{x-m}{\sigma}\right)^2\right] \tag{2.51}$$

where m and σ are the mean and standard deviations of input variable x.

$$F(x) = \frac{1}{\sigma\sqrt{2\pi}} \int_{-\infty}^{x} \exp\left[-\frac{1}{2}\left(\frac{t-m}{\sigma}\right)^2\right] = \frac{1}{2}\left[1 + \mathrm{erf}\left(\frac{x-m}{\sigma\sqrt{2}}\right)\right] \tag{2.52}$$

with

$$\mathrm{erf}(z) = \frac{2}{\sqrt{\pi}} \int_{0}^{z} e^{-t^2} dt \tag{2.53}$$

The Gaussian distribution is symmetrical and covers both negative and positive values of input variable. Therefore it cannot be used directly for many radiowave propagation related variables (voltage, power, fading time etc.) because they have only positive values. However it can be used for the logarithmic form of these values.

Log-normal distribution

Log-normal distribution happens when a large amount of slightly important random causes are multiplied. A random variable has a log-normal distribution if it has Gaussian distribution in logarithmic units. Therefore it can be used directly for positive value variables and its PDF and CDF are following:

$$p(x) = \frac{1}{\sigma\sqrt{2\pi}} \frac{1}{x} \exp\left[-\frac{1}{2}\left(\frac{\ln(x)-m}{\sigma}\right)^2\right] \tag{2.54}$$

and

$$F(x) = \frac{1}{\sigma\sqrt{2\pi}} \int_{-\infty}^{x} \frac{1}{t} \exp\left[-\frac{1}{2}\left(\frac{\ln(t)-m}{\sigma}\right)^2\right] = \frac{1}{2}\left[1 + \mathrm{erf}\left(\frac{\ln(x)-m}{\sigma\sqrt{2}}\right)\right] \tag{2.55}$$

However, here the m and σ are the mean and standard deviations of logarithm of input variable x.

Rayleigh distribution

Rayleigh distribution is given by the sum of a large number of vectors with low amplitudes and uniformly distributed phases. A sum of these vectors creates a complex vector whose real and imaginary parts are Gaussian distributed and the magnitude of this vector is a Rayleigh distributed random variable [21]. Therefore it is defined as:

$$\zeta = \sqrt{\mu_1^2 + \mu_2^2} \tag{2.56}$$

where μ_1 and μ_2 are independent zero-mean Gaussian distributed random variables. The Rayleigh distribution applies to non-limited continuous positive variables such as Log-normal distribution (Fig. 2.17). Its PDF and CDF are:

$$p(x) = \frac{x}{\sigma^2} \exp\left(-\frac{x^2}{2\sigma^2}\right) \tag{2.57}$$

and

$$F(x) = 1 - \exp\left(-\frac{x^2}{2\sigma^2}\right) \tag{2.58}$$
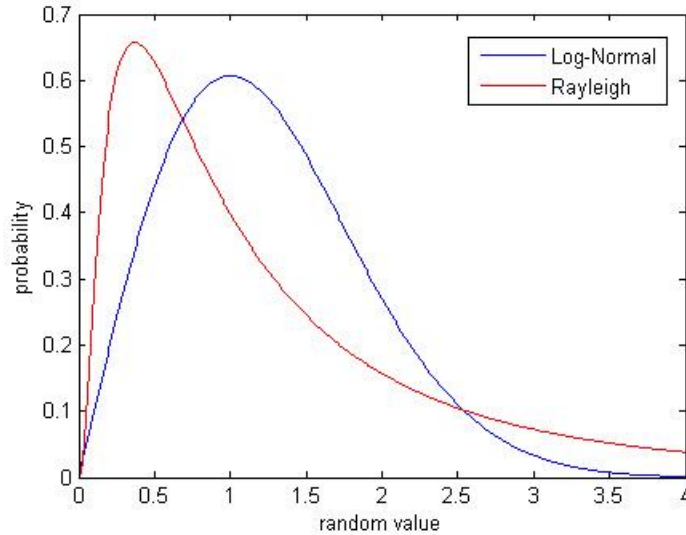
Figure 2.17: PDF comparison of Log-normal and Rayleigh distribution

Rice distribution

The Rice distribution (sometimes called Nakagami-Rice or Nakagami-n distribution) is the distribution of a vector which is the sum of a fixed vector and a vector whose length has Rayleigh distribution. The fixed vector represents a strong ray in received signal composition, usually under line of sight conditions, and it is usually called the direct or coherent component. On the other hand, the random vector represents a large amount of weak rays - the result of multipath propagation - and it is often called the multipath

25

or diffuse component. The presence of a direct ray is the reason for using this distribution primarily in satellite links because the LOS conditions are usually not considered in terrestrial links.

The assumption can also be expressed as the magnitude of a complex vector whose real and imaginary parts are independent Gaussian distributed random variables each summed with a constant. In figure 2.18 a phasor representation can be found.
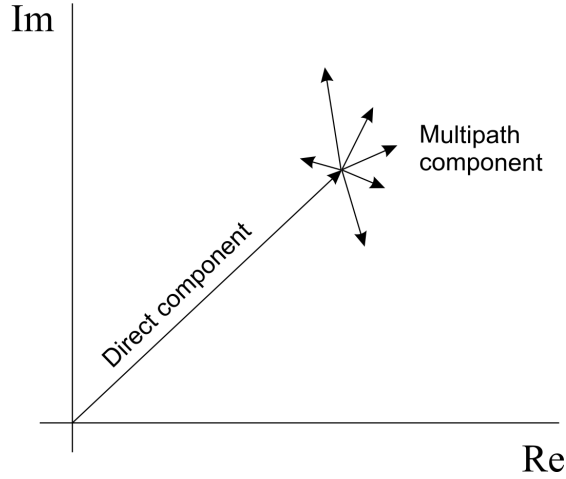
Figure 2.18: Phasor representation of Rice distribution

The components are often expressed by these parameters: normalized direct ray amplitude a^2 and normalized average power of multipath component $2\sigma^2$.

Rice distribution has the following PDF expression [20].:

$$p(x) = \frac{x}{\sigma^2} \exp\left[-\frac{x^2 + a^2}{2\sigma^2}\right] I_0\left(\frac{xa}{\sigma^2}\right) \tag{2.59}$$

where a is the length of a fixed vector, σ is the most probable length of Rayleigh vector and I_0 is the zero order Bessel function.

There can be two assumptions from the definition:

1. The power of the direct component is constant, while the overall power of the combination of the direct and multipath component varies. This assumption is frequently used for studying the composition of received signal and for this purpose a ratio between the direct and multipath component is used. It is quantified by parameter K called the K-factor.

$$K(\mathrm{dB}) = 10\log\left(\frac{a^2}{2\sigma^2}\right) \tag{2.60}$$

2. The power of both components varies, but the overall power of the combination remains constant. This is normally used for studying multipath propagation through the atmosphere.

The Rice distribution collapses to a Rayleigh distribution when a is null ($k = 0 \equiv -\infty$ dB)

Several other propagation related distributions are described in [20].

2.3.2 Second order statistical analysis methods

The above mentioned statistical tools are usually called first order statistics. They quantify the amplitude distribution of a received signal. So called second order statistics provides information about the speed of variations in a signal.

Auto-correlation function

The time domain Auto-correlation function describes the repeating patterns in a signal. It is defined as [21]:

$$\tilde{r}_{\mu\mu}(\tau) = \lim_{T \to \infty} \frac{1}{2T} \int_{-T}^{T} \tilde{\mu}^*(t)\tilde{\mu}(t+\tau)dt, \quad t \in \mathbb{R} \tag{2.61}$$

where $\tilde{\mu}$ is a deterministic signal and τ is a time shift.

Power spectral density

A Fourier transform of the autocorrelation function gives a Power Spectral Density $\tilde{S}_{\mu\mu}$ (PSD), which describes how power is distributed with frequency. It can be written as:

$$\tilde{S}_{\mu\mu}(f) = \int_{-\infty}^{\infty} \tilde{r}_{\mu\mu}(\tau)e^{-j2\pi f\tau}d\tau, \quad f \in \mathbb{R} \tag{2.62}$$

Beside the above mentioned functions there are other tools which describe variations in a more detailed way.

Level crossing rate

Level crossing rate (LCR) provides information how often a given ordinate in average from down to up (or from up to down) within a one second interval is crossed. In mobile systems the LCR can be defined as the average number of crossings within a time during which the receiver travels a distance of one wavelength.

Average fade duration

Average fading duration (AFD) describes the mean duration of a signal under a specific ordinate in seconds (resp. traveled wavelengths).

The received signal can have various spectral shapes. The LCR and AFD methods are often used for direct analysis of link performance. On the other hand the Power spectrum or auto-correlation function are usually used for the quantification of Doppler spread.

2.4 Channel modeling

In terrestrial links the models solve shadowing and blocked situations and the influence of obstacles on statistical properties of the link. In this section models for satellite links are exclusively presented because the UAV link shows more geometrical similarities with them.

2.4.1 Amplitude distribution modeling

First, models concerning the amplitude distribution are presented.

Suzuki model

The Suzuki model assumes that a direct component is not present [22] and concerns only multipath component. It uses an assumption that multipath component is Rayleigh distributed but its average power, described by parameter $2\sigma^2$ varies with log-normal distribution for longer sections of series. Its PDF can be written as:

$$p(x) = \frac{8.686x}{\Sigma\sqrt{2\pi}} \int_0^\infty \frac{1}{\sigma^3} \exp\left[-\frac{(20\log\sigma - M)^2}{2\Sigma^2}\right] \exp\left(-\frac{x^2}{2\sigma^2}\right) d\sigma, \quad (x \geq 0) \qquad (2.63)$$

Loo model

The Loo model [23] is based on Rice distribution using the first assumption that the direct component is constant while the combination of direct and multipath component varies. For short sections of traveled route it should follow the Rice distribution. For longer sections the assumption is that a direct component is not a fixed vector but varies according to Log-Normal distribution. This variation of the direct component is meant to be caused by shadowing. Loo distribution is very versatile and includes special cases as normal and Rice distribution for large values of a direct component and Rayleigh distribution when direct component is suppressed. Its PDF can be expressed as:

$$p(x|a) = \frac{8.686x}{\sigma^2 \Sigma_{dB}\sqrt{2\pi}} \int_0^\infty \frac{1}{a} exp\left[-\frac{(20\log(a) - M_{dB})^2}{2\Sigma_{dB}^2}\right] exp\left[-\frac{x^2 + a^2}{2\sigma^2}\right] I_0\left(\frac{xa}{\sigma^2}\right) da$$

$$(2.64)$$

where M and Σ are the mean and the standard deviations of its associated normal distribution for the direct signals amplitude in dB.

Several other models combining the known distributions with direct and multipath component have been published e.g. Corraza and Vatalaro [24] proposed a model where shadowing affects both direct and diffuse components. S. H. Hwang [25] introduced a channel model where each of the components - direct and diffuse - is independently affected by shadowing. However, the two mentioned above are the most applied in practice. The Suzuki models can also be used in terrestrial macrocell units as a benchmark for system performance and Base station deployment studies and on the other hand, the Loo model is often used for modeling land mobile satellite channels [26].

2.4.2 Second order statistics modeling

In mobile systems the phenomena which have the main influence on the variation speed are considered to be Doppler spread. There are basically two approaches how to synthesize the Doppler spread: The sum of sinusoids method and the filtered Gaussian noise method.

Sum of sinusoids

Generally the Sum of Sinusoids (SoS) method creates a complex Gaussian fading process by superposing many waves with different parameters (amplitude, phase, angle of arrival). The resulting process tends to be Gaussian distributed according to the central limit theorem [27].

The basis of SoS methods is the Rice method where an infinite number of waves are superposed with each having constant gains, equidistant frequencies and a random phase uniformly distributed. Mathematically it can be described as:

$$\mu_i(t) = \lim_{N_i \to \infty} \sum_{n=1}^{N_i} c_{i,n} \cos(2\pi f_{i,n} t + \theta_{i,n}) \tag{2.65}$$

where the gains $c_{i,n}$ and frequencies $f_{i,n}$ are constants defined as:

$$c_{i,n} = 2\sqrt{\Delta f_i S_{\mu_i \mu_i}(f_{i,n})} \tag{2.66}$$

and

$$f_{i,n} = n\Delta f_i \tag{2.67}$$

The SoS simulation models can be deterministic or stochastic. Deterministic models use the deterministic parameters (amplitude, angle of arrival, phase), therefore, every simulation run gives the same resulting series. Other ones are stochastic models where at least one of parameters is randomly generated at the beginning of the process.

Filtered Gaussian noise simulators

Other method how to generate a complex Gaussian fading process is by directly generating a complex Gaussian variable and filtering it to simulate the desired Doppler spread (Doppler filter) First, a complex Gaussian variable is generated. It is composed of two independent, discrete, random Gaussian distributed variables $x_{G,R}[n]$ and $x_{G,I}[n]$ with zero mean and variance $1/2$. Then the complex Gaussian variable can be denoted as:

$$x_G[n] = x_{G,R}[n] + j x_{G,I}[n] \tag{2.68}$$

The desired shape of Doppler spectra is expressed by Power spectral density or by autocorrelation function. Some possible spectra are introduced:

The Jakes Doppler spectrum, sometimes called the Classical Doppler spectrum presented by Clarke [28] and Gans [29], is commonly used. It assumes that radio waves propagate horizontally with uniform angle of arrival distribution between $-\pi$ and π which was found to be a good model for long-term conditions. Its baseband normalized spectrum is expressed as:

$$S_j(f) = \frac{1}{\pi f_m \sqrt{1 - \left(\frac{f}{f_m}\right)^2}}, \quad |f| \leq f_m \tag{2.69}$$

Where f_m is maximum Doppler shift and autocorrelation function as:

$$r_{\mathrm{j}}(\tau) = J_0(2\pi f_{\mathrm{m}}\tau) \tag{2.70}$$

Where J_0 is a zero order Bessel function of the first kind.

Another possibility is the Gaussian Doppler spectrum. It is well-suited for cases with long delays [30]. Its baseband normalized spectrum is expressed as:

$$S_{\mathrm{g}}(f) = \frac{1}{\sqrt{2\pi\sigma_{\mathrm{g}}^2}} \exp\left(-\frac{f^2}{2\sigma_{\mathrm{g}}^2}\right) \tag{2.71}$$

and autocorrelation function is:

$$r_{\mathrm{g}}(\tau) = \exp(-2\pi^2\sigma_{\mathrm{g}}^2\tau^2) \tag{2.72}$$

where σ_{g} is the standard deviation of the Gaussian Doppler spectrum.

Several other spectra can be used e.g. Flat Doppler spectrum, Symmetrical and Asymmetrical restricted Jakes Doppler spectrum, Bi-Gaussian Doppler spectrum. Details with corresponding power spectra and autocorrelation function can be found in [27]

A square root of Power spectral density yields a filter frequency response $H(f)$ and an inverse Fourier transform of $H(f)$ gives the desired impulse response of the filter $h(t)$ as follows:

$$\rho_\Gamma(t) = \xrightarrow{\ F\ } S(f) \tag{2.73}$$

$$h(t) = \xleftarrow{\ F^{-1}\ } H(f) = \sqrt{S(f)} \tag{2.74}$$

Both finite and infinite impulse response digital filters can be used for obtaining the desired shape. An autocorrelation function or Power spectral density can be expressed by a closed form formula which yields to a continuous impulse response. The sampling should be performed after Fourier transform to mitigate errors.

2.4.3   Generative models

The models mentioned up to this point can only simulate some of the phenomena affecting the channel. So called generative models or time series generators can generate the received signal with the same statistical characteristics as if it was measured with most influences taken into account: amplitude distribution and spectral properties by combining the synthesizing methods described above. The assumptions from models are expressed in circuit form. An example of circuit implementation of the Loo model is found in Fig. 2.19[31].
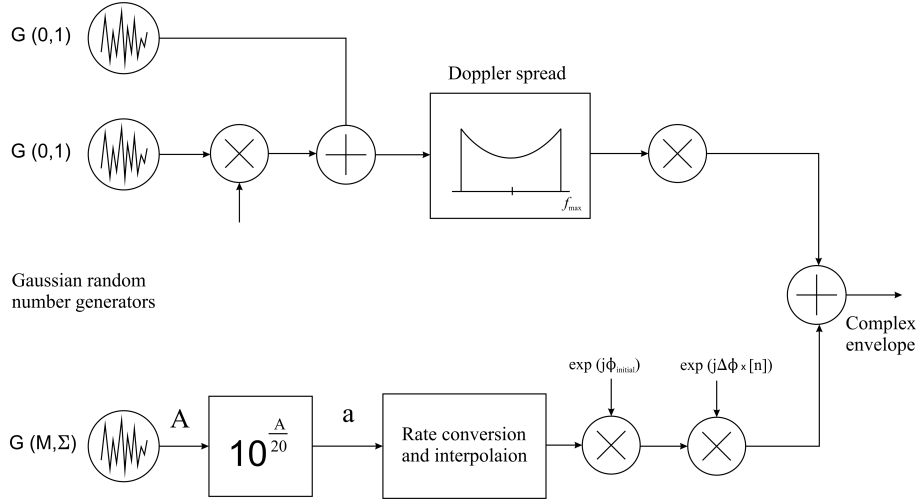
Figure 2.19: Time series generator using Loo model

The division of direct and multipath components, used in amplitude distribution modeling, is shown here in generative models represented by two parallel rails. In the lower rail a direct component rises from a Gaussian random number generator with a defined level and standard deviation. After conversion to linear units it is log-normal distributed. In generative models, in addition to amplitude distribution, that is to say first order statistics, spectral properties, or second order statistics, are modeled. Additionally, the spectrum is modified to the specific rate of changes in direct component amplitude (shadowing frequency). Finally at the end of the direct component rail a Doppler shift is presented.

In the upper rail a multipath component is generated. Using two independent zero-mean Gaussian random number generators, a complex Gaussian random number is constructed, whose absolute value at the end yields Rayleigh distribution. As in the lower rail, second order statistics are also presented here by modeling the Doppler spread by the Jakes Doppler filter. Finally, the standard deviation of the multipath component is set by parameter σ.

At the right part both rails are added forming a complex envelope. The circuit can be realized in a signal processing environment (e.g. Matlab).

Alternatively, synthesizing Doppler spread by a Butterworth filter can be done [31], where the transfer function can be written as:

$$|H_{\text{Butt}}(f)|^2 = \frac{A}{1 + (f/f_{\text{c}})^{2k}} \tag{2.75}$$

where f_{c} represents the cut-off frequency and k the order of the filter.

2.4.4 State oriented models

Time series generators are capable of modeling most short term properties of a received signal. However, in long term observations sudden changes in the environment can be found as the receiver is in motion, e.g. line-of-sight shadowing and blockage by buildings or trees. In Fig. 2.20 an illustration of these changes is depicted.

31
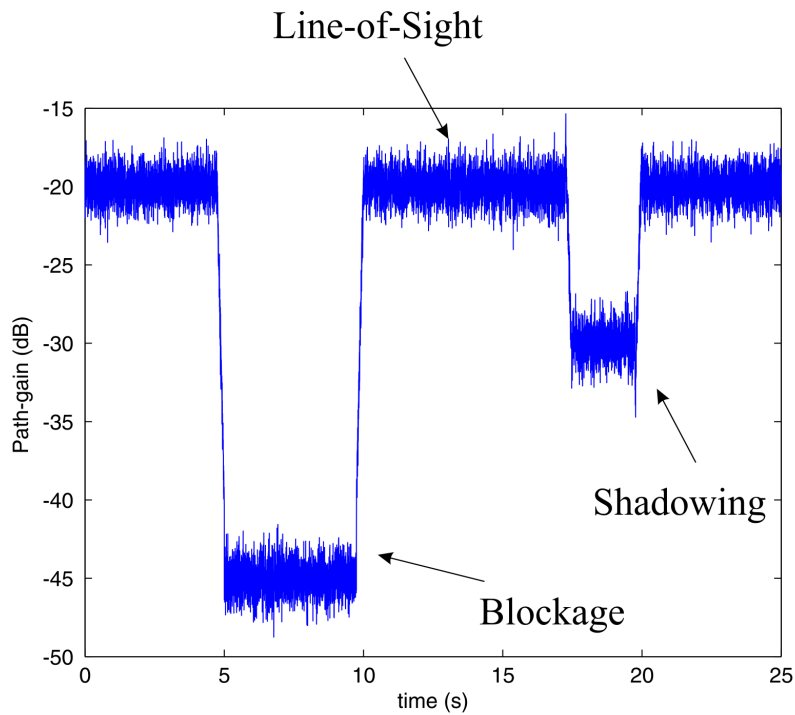
Figure 2.20: Line-of-sight shadowing and blockage illustration

In these cases a Markov chain [32] can be used as a discrete random process in which the sample data are divided into several states and the probability that the next sample will be in the current state is not dependent on previous events. For a full Markov chain two matrices are necessary. Firstly, a state probability array, which contains probabilities of each state occurrence, and, secondly, a matrix which contains the probabilities of transfer between states.

For modeling applications it is possible to use a semi-Markov chain in the following way: Divide the received signal into several states (Fig. 2.21) such as is shown here:

$$A - \text{ Line of sight condition}$$
$$B - \text{Shadowed condition}$$
$$C - \text{Blocked condition}$$

Figure 2.21: State transition scheme

According to the average received power, each state is modeled by a single, different, statistical model with different parameters. Each model provides a probability function f_A, f_B, f_C and the final total probability function (PDF or CDF) is defined as:

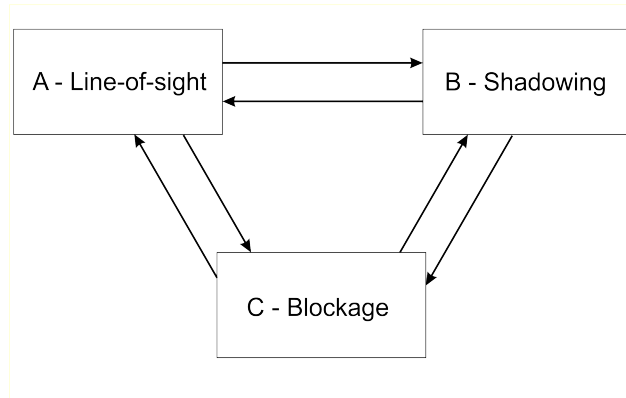$$f_{\text{total}} = P_a f_a + P_b f_b + P_c f_c \qquad (2.76)$$

where P_a, P_b, P_c are probabilities of each state occurrence [33].

Lutz et. al. [34] introduced a two-state model representing a "good state" when the envelope of the received signal follows Rice PDF, and a "bad state" when the envelope of the received signal follows a combination of Rayleigh and Log-normal distribution. This model is also known as the DLR model. Karasawa et. al. [35] proposed a model with three states: LOS clear, LOS shadowed and complete blockage. LOS clear is represented by Ricean distribution, LOS shadowed by the Loo model and blockage by Rayleigh distribution. The overall probability distribution is a weighted linear combination of all three states as described in Rec. ITU-R P.681-6 [33] as a semi-Markov chain. The probabilities of each state occurrence are derived from measurement.

F. P. Fontan et. al. [32] presented a three-state model concentrating on fading modeling where the multipath propagation influence is first removed by a low-pass filter. Then, the measured data are classified into three states dependent upon fading level. Each state is described by the Loo model and parameters for all measuring scenarios are found. In this work a state machine capable of simulating a random channel with fading by a Markov chain was presented with matrices with statistical data being gained from measurement. For a sufficiently large data set, probability matrices were duplicated and merged.

2.5 Diversity

In the previous sections phenomena which degrade the link performance were analyzed, quantified and modeled. It can be stated that the problem of signal degradation is defined and well-described for land mobile satellite and terrestrial links. Moreover, several methods for mitigating the degradation were developed and their influence on links was studied in literature. In this section one of the methods is presented.

2.5.1 Link reliability enhancement principle

There are many ways how to enhance link reliability and improve the budget. In this work a diversity methods were chosen for enhancing the studied link. The possible use of diversity techniques are the topic of interest of many publications e.g. [36] [37] . But no study has been done for UAV links.

The diversity methods take the multipath propagation phenomenon - which usually has a bad influence on the received signal - and use it to enhance the link performance. The basic principle lies in the following assumption: At each moment of receiving, different places, frequencies, polarizations, angles of arrival or delayed signals can yield a different received power. If a link is divided into several uncorrelated branches, each with different properties, the deep fades will be at a different position at the time of receiving. If, at each moment, the strongest signal is chosen, or, the signals are combined, the deep fades can be mitigated and average received power can be enhanced (Fig. 2.22).
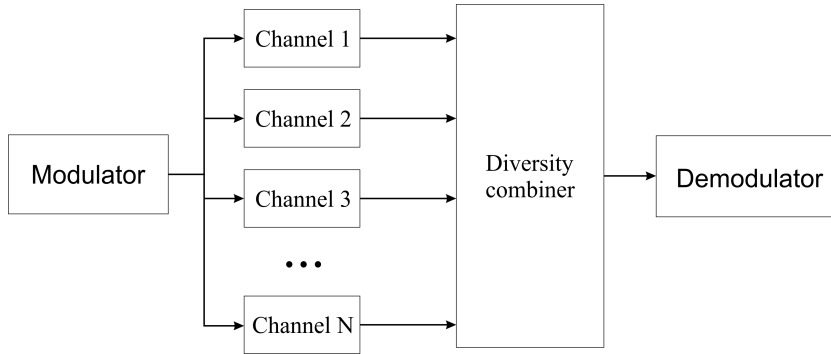

Figure 2.22: Diversity combining scheme [15]

2.5.2 Criteria of efective use

The efficiency of diversity methods is strongly dependent on cross-correlation between the channels which is mainly given by the variety of environment. The less the channels are correlated, the less the probability of fades being at one place are, and the better the results given by diversity methods. Thus, it may not be easy to get uncorrelated channels for performing diversity. The most feasible method is space diversity [14] where multiple receiving or transmitting antennas can generate sufficiently uncorrelated channels. Another condition of effective diversity method use is when the signal from branches has similar mean power.

The amount of enhancement is usually quantified by Diversity gain which is taken from the difference between single and combined signal CDFs for each probability level. Another parameter is Diversity enhancement which is derived from the difference between single and combined signal CDFs for each received power level. In statistical analysis it is assumed that the single branches are Gaussian processes of equal mean power, giving their envelope a Rayleigh distribution.

2.5.3 Combining methods

Signals can be combined in several possible ways [14]. The most common are: Selective Combining (SC); Maximal Ratio Combining (MRC); Equal Gain Combining (EGC).

Selective Combining

Selective combining is the simplest of all diversity methods. At each moment of reception, the strongest channel is chosen and composes the final signal. In Fig. 2.23 an example of Selection combining is shown. It can be seen how the combined signal is free from any deep fades, strongly enhancing the link reliability.
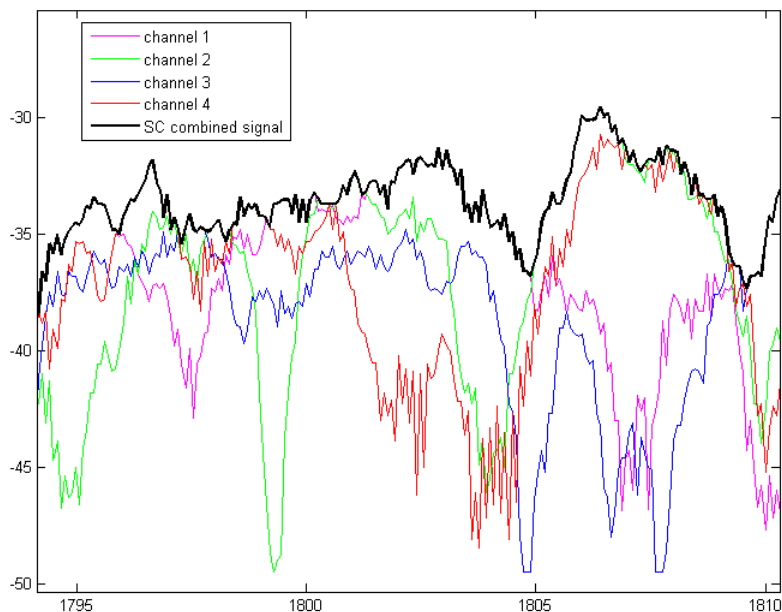
Figure 2.23: Example of Selective combining method

However, the strongest channel evaluation mechanism must be faster than the speed of fade occurrence which limits the usefulness of this method depending on the bandwidth used in the receiving system [14]. Usually for diversity feasibility analysis an ideal selector is considered.

Then the combined signal can be expressed as:

$$r_0 = \max\{r_1, r_2, ..., r_M\} \tag{2.77}$$

where r_0 is the resulting effective signal envelope and the r_i are individual branch effective envelopes as in Appendix D of [14] where the concept of an effective signal envelope is defined.

The CDF of a simultaneously chosen strongest signal from M branches can be written as:

$$P_M(\gamma_s) = \left[1 - \exp\left(-\frac{\gamma_s}{\gamma_0}\right)\right]^M \tag{2.78}$$

where γ_s is specific carrier-to-noise ratio, CNR and γ_0 is the mean of CNR.

Maximal Ratio Combining

This method performs a sum of branches weighted before summation by their own signal voltage to noise power, but it is necessary to co-phase the signals from branches. Again, for analysis purposes, the signals from branches are considered as co-phased. Apart from mitigating deep fades, combining all branches slightly raises the average CNR.

The envelope of the combined signal can be written as:

$$r_R = \sum_{k=1}^{M} a_k r_k \tag{2.79}$$

where a_k represents the weighting coefficient

Using effective signal envelopes, the combined signal is expressed in the following way:

$$r_0 = \sqrt{r_1^2 + r_2^2 + ... + r_M^2} \tag{2.80}$$

Then the CDF of the combined signal from M branches is:

$$P_M(\gamma_R) = 1 - \exp\left(-\frac{\gamma_r}{\gamma_0}\right) \sum_{k=1}^{M} \frac{\left(\frac{\gamma_r}{\gamma_0}\right)^{k-1}}{(k-1)!} \tag{2.81}$$

Equal Gain Combining

The Equal Gain Combining method is similar to Maximal Ration Combining but without any weighting mechanism. This method yields slightly worse results than the MRC method. The resulting envelope is expressed as:

$$r_R = \sum_{k=1}^{M} r_k \tag{2.82}$$

and using effective signal envelopes:

$$r_0 = \frac{r_1 + r_2 + ... + r_M}{\sqrt{M}} \tag{2.83}$$

It is difficult to analytically express the CDF of a combined signal from more than two branches and results must be obtained by numerical integration techniques [14]. For two branch systems, the CDF of the resulting signal can be written as:

$$p(\gamma_n) = 1 - \exp(-2\gamma_n) - \sqrt{\pi\gamma_n} \exp(-\gamma_n) \operatorname{erf} \sqrt{\gamma_n} \tag{2.84}$$

where γ_n is an output CNR relative to the single-branch mean.

Chapter 3

Goals

Expanding applications of UAV need extensive research in communication link modeling. As explained above, the corresponding low elevation link for a selected case of an urban nomadic user terminal is, from several aspects, very different from classic satellite and terrestrial links which has been investigated for decades. It is namely the geometry, movements of the elevated terminal and fixed position of the ground terminal resulting in a scenario where no relevant propagation models are available in the literature to date.

For this reason, the main goal of the thesis was defined to develop new propagation models for planning UHF narrow-band low elevation links between a slow speed UAV and a nomadic user in an urban area.

Generally there are two aspects which should be followed in wireless link planning: a model to estimate the link path loss for power budget calculations and tools to characterize the narrow-band propagation channel. Due to the expected nature of fast fading in the urban environment, a study on space diversity would be highly appropriate. It is clear that, first, the usefulness of known modeling approaches for terrestrial and satellite wireless systems should be tested for the given scenario. However, as was shown in previous chapters, most of the available propagation models, as well as experimental datasets, are out of their validity range due to the differences in link geometry and propagation environment. It is urgent for measurement trials to provide appropriate experimental data to develop and validate the new propagation models.

The main goal of the thesis can be divided into several constituent tasks:

1. To design and conduct a propagation measurement campaign to address the given scenario of UHF narrow-band low elevation links between a slow speed UAV and a nomadic user in an urban area. The resulting experimental datasets should support the three following tasks.

2. To develop and validate the path loss propagation model for the given scenario (Chapter 4).

3. To characterize the propagation channel for the given scenario by means of both first and second order statistics and to develop and validate a corresponding time series generator (Chapter 5).

4. To analyze the space diversity gain for multiple antennas at the ground terminal for the given scenario (Chapter 6).

Chapter 4

Path-loss model

To develop a model capable of providing information on the path loss for a specified geometry, there is need to understand the principles which influence the final received signal. In this chapter the diffraction, reflection and multipath propagation phenomena are studied for this specific geometry and, based on this information, a new path-loss model is developed.

This model should provide guidance on expected attenuation levels when the nomadic receiving terminal in urban areas is at street level; this can be considered as a worst-case scenario where the terminal is totally surrounded by buildings and no alignment of the street with the link exist (waveguide effect). Alternative settings for the terminal above the nearby rooftops may not be possible in some operational cases.

It is essential to conduct an experiment simulating a link to develop a path-loss model. In such a complex environment as an urban area many unknown details can influence link performance and any application of theoretic principles on an environment with approximated obstacle shapes, without any comparison to measurements, yields uncertain results. Therefore, the key to developing a trustworthy and widely used path-loss model is to connect the theory with measurement results by finding suitable approximations of link geometry and theory methods. This approach combines deterministic and empiric model methods to create a suitable solution for many applications - see Semi-empirical models in chapter 2.

A unique measurement campaign simulating an UAV by means of a remotely controlled airship was performed at 2 GHz. Based on these measurements a new path-loss model has been conducted.

The core of this chapter was published in [38] so parts of the text may be identical.

4.1 Experimental trials

In this section the experiment setup is discussed, data processing is reviewed and brief comments on the results are given.

4.1.1 Measurement equipment

A remotely controlled airship [39] was used to simulate a UAV (Fig. 4.1). The specifications of the airship can be found in Table 4.1. The airship followed pre-defined routes

carrying a transmitter while a receiver was placed in a static position on the ground. The transmitter was placed on the bottom side of the airship with an antenna placed under the receiver, it being the lowest part of the aircraft providing an omni-directional view. The transmitter's position on the airship allowed substantial pitch and roll without any influence on the link by payload shadowing (The body of airship is transparent for electromagnetic waves at this frequency). The airship system also had the capability of storing pitch and roll data which were used to check the values of pitch/roll angles for the eventual discarding of invalid data. During the flights, GPS position data were stored. To increase positioning accuracy, a separate GPS device was used with the ability to store the raw GPS data needed for differential GPS post-processing correction.

Figure 4.1: Remotely controlled airship used in measurements

Length	9 m
Maximal diameter	2.3 m
Volume	$27\,\mathrm{m}^3$
Propulsion	electrical 2 x 700 W @ 24 V
Maximum flight level	1000 m
Maximum flight time	60 min
Flight speed	3 to 10 m/s
Maximum payload	5.5 kg

Table 4.1: Airship specifications

A transmitter, developed at the Dept. of Electromagnetic Field, Czech Technical University, with a carrier frequency of 2 GHz and transmitted power of 27 dBm with a signal being an un-modulated carrier (CW). A quarter-wave monopole with rod ground plane was used as a transmitting antenna(Fig. 4.2).

Figure 4.2: A quarter-wave monopole with rod ground plane used as a transmitter antenna

A four-channel receiver, whose specifications can be found in Table 4.2, for performing diversity studies was setup (Fig. 4.3). The receiver allowed simultaneous measurements at four channels with a recording rate of 100 samples per second. The sensitivity was -126 dBm for a measurement bandwidth of 12.5 kHz. The receiver was also developed at the Dept. of Electromagnetic Field, Czech Technical University. The receiver was connected to four monopoles, similar as at the transmitter side, forming a square with 22.5 cm sides (1.5λ). The antennas were placed 1.5 m above street level (Fig. 4.4). In this chapter, data from a single antenna are analyzed while further studies including statistical modeling and diversity analysis are described in the following chapters. However, consistency checks between the path-loss values measured in all four channels were carried out to verify the accuracy of the measurements.
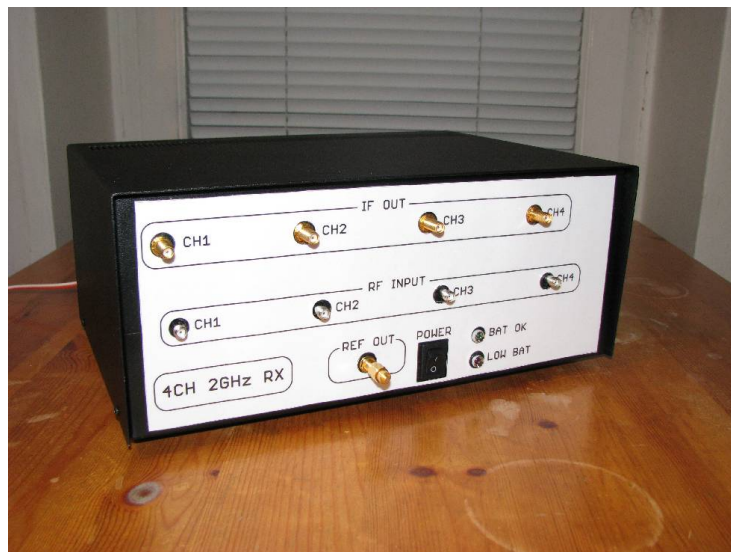

Figure 4.3: Four channel receiver

40

Input frequency	1990 to 2010 MHz
Number of channels	4
Itermediate frequencies	455 MHz / 10.7 MHz
Resolution bandwidth (HPBW)	12.5 kHz
Samples per second per channel	100
Calibrated linear dynamic range	-35 to -126 dBm
Resolution of measurement	0.1 dB
Immunity to image frequency	> 90 dB
Immunity to intermediate frequency	> 90 dB
SSB phase noise	-100 dBc/Hz (20 kHz offset)
frequency stability	$\pm$ 1ppm ($-20°$ C to $+70°$)
External power supply	10 to 18 V (18W)
Interface	USB

Table 4.2: Receiver specifications

Figure 4.4: Receiving antenna arrangement at street level.

Attention was also paid to the issue of possible mutual coupling between the antennas giving rise to distortions in the individual antenna radiation patterns. To analyze this possible issue a measurement of antenna radiation pattern in an anechoic chamber was performed. In Fig. 4.5 the vertical and horizontal pattern of one antenna in the diversity array is depicted.
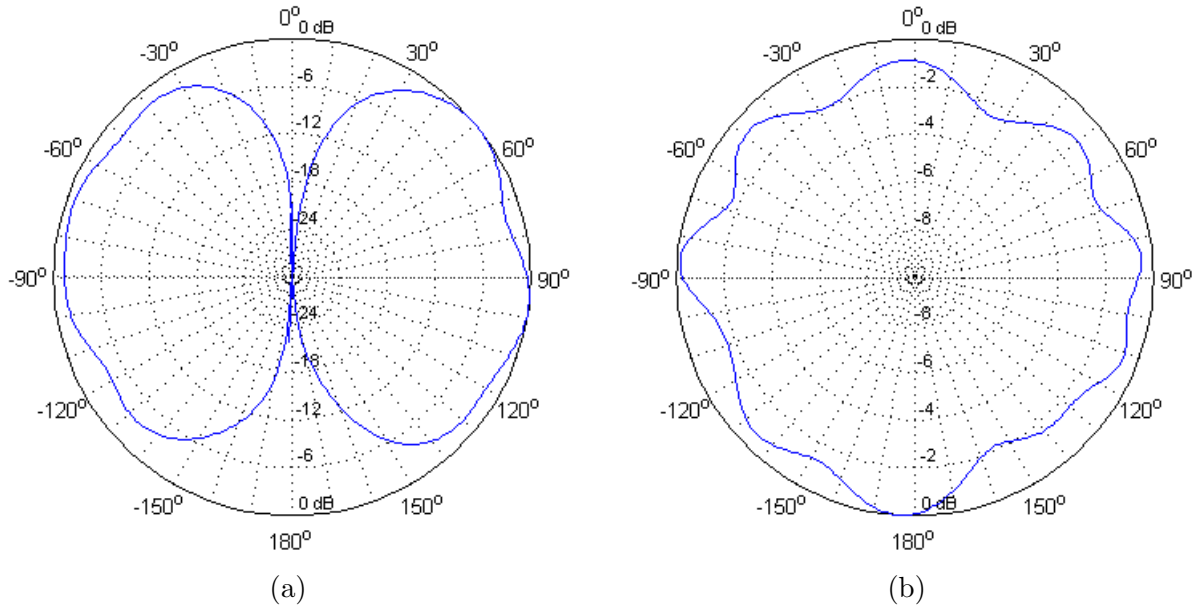
Figure 4.5: Vertical (a) and horizontal (b) pattern of one antenna in the diversity array

It is clear that the perfectly omni-directional pattern is slightly distorted showing peak-to-peak oscillations below 3 dB. However, due to a transmitter movement within limited azimuth angles, these oscillations do not affect the received power.

4.1.2 Measurement setup

To study the UAV channel in urban areas, a fairly flat and uniformly built-up district of the Dejvice neighborhood of the city of Prague was chosen. The area is approximately 570x580 m^2 in size, buildings are of a similar type, made of brick, of about 22 m in height, built in 1922. Street widths are in the order of 17 m.

The airship flew from and toward the receiver at approximately constant azimuths from a distance of 1.2 to 6.5 km in flight levels from 150 m to 300 m above ground (Fig. 4.6 and 4.7). Thus, from the ground terminal the UAV was seen under elevation angles from 1.6 to 6.5 degrees. In the study presented in this chapter, only the azimuths perpendicular to the street direction were considered for the analysis.
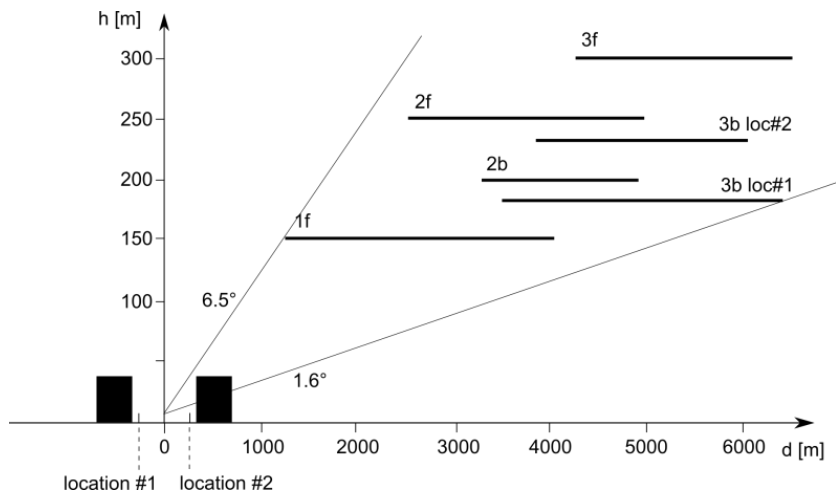
Figure 4.6: Flight and receiving antenna locations used in this study.

Figure 4.7: Flight route - Image from Google Earth

The receiver was placed at two different, representative locations simulating possible positions of the UAV receiving station (Fig. 4.8). The first position "location #1" was chosen by trying to get as far as possible from the nearest building in the direction of the UAV, thus minimizing the diffraction loss. The second position "location #2" corresponds to the worst-case scenario where the receiver is very close to the building in the direction of the UAV (Fig. 4.8 and Fig. 4.4). The airship flight paths were perpendicular to the street.

Figure 4.8: Receiver locations #1 and #2 (image from Google Earth), in Dejvice, city of Prague.

4.1.3 Data processing

During the measurements, received power data plus auxiliary information were recorded to different devices: position data was stored in a GPS device, flight data including pitch and roll were stored in the operator notebook through the airship control link and, finally, the received data was stored in a notebook attached to the test receiver. All data sources were time stamped for off-line synchronization at the post-processing stage. The clocks of the notebooks were synchronized to the GPS time prior to performing the measurements.

Position data were enhanced using system CZEPOS [40] raising accuracy up to 0.4 m which, considering the distances in terms of kilometers, can be considered as sufficient.

Once all data sources were synchronized, invalid data due to large pitch or roll values were flagged out. The acceptable limits for both angles were set to a maximum of 10 degrees, however, values higher than 5 were rare and the number of invalid data stamps is negligible. The fast, multipath-induced variations were removed by low pass filtering. The averaged signal series was used for comparison with model predicted levels as discussed later on. Several window sizes were tested; finally a size of 4,000 wavelengths (600 m) was found to adequately remove the slow and fast variations, leaving only the extremely slow variations. The window size is high due to link geometry where a rapid movement of a distant transmitter causes only a small, angular change at the place of receiver. Averaging was performed on linear power levels which were then converted to logarithmic units.

Finally, the total path loss was calculated from which the free space loss (FSL) was subtracted to calculate the excess loss, L (dB). Fig. 4.9 illustrates a path loss series as a function of the distance from the receiver for test flight 1f, Rx "location #2" (Fig. 4.7).
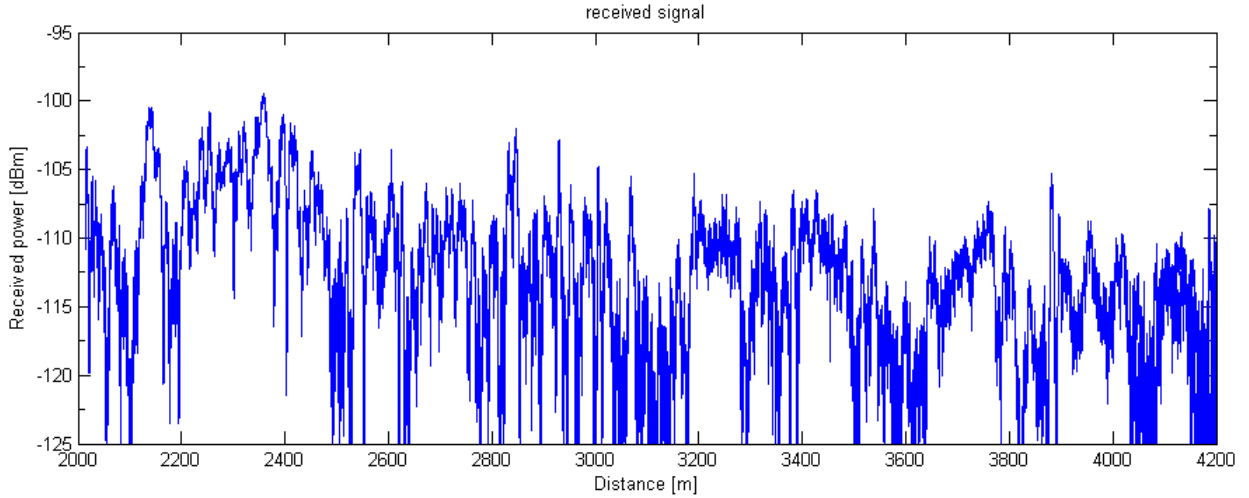
Figure 4.9: Example of path loss series as a function of distance for test flight 1f, Rx "location #2"

4.1.4 Results

The excess loss, L (dB), calculated from the measured data was plotted as a function of the distance to the airship. Significantly strong variations due to specular reflections, especially between 2 and 2.2 km (Fig. 4.9 and Fig. 4.10), and to diffuse multipath throughout, were observed in the measured series. These variations suggest that the received signal is composed of several strong rays rather than from many weaker ones. Therefore, a consideration of diffuse scattering from the rear building was omitted.

To facilitate the comparison between predicted and measured excess loss, a running mean filter was used to remove the slow and fast variations. Fig. 4.10 illustrates measured excess loss after low-pass filtering for the path loss series shown in Fig. 4.9. This figure also shows modeling results which will be discussed in section 4.2.

In Fig. 4.10, the data taken at "location #2" (Rx on the Tx side of the road, closest to the blocking building) are shown. The general behavior is that, once the free space component (which depends logarithmically on the distance as $20 \log(d)$) has been removed, a fairly distance-independent trend can be observed. It is the elevation that significantly determines excess loss. Standard terrestrial empirical models like Hata-COST 231 (section 2.2.2 in chapter 2) are strongly dependent on the distance; this makes this type of model not particularly suitable for use in low elevation links such as those found in UAV applications. The data taken at "location #1" (Rx on the Tx opposite side of the road) also confirmed the above observations.
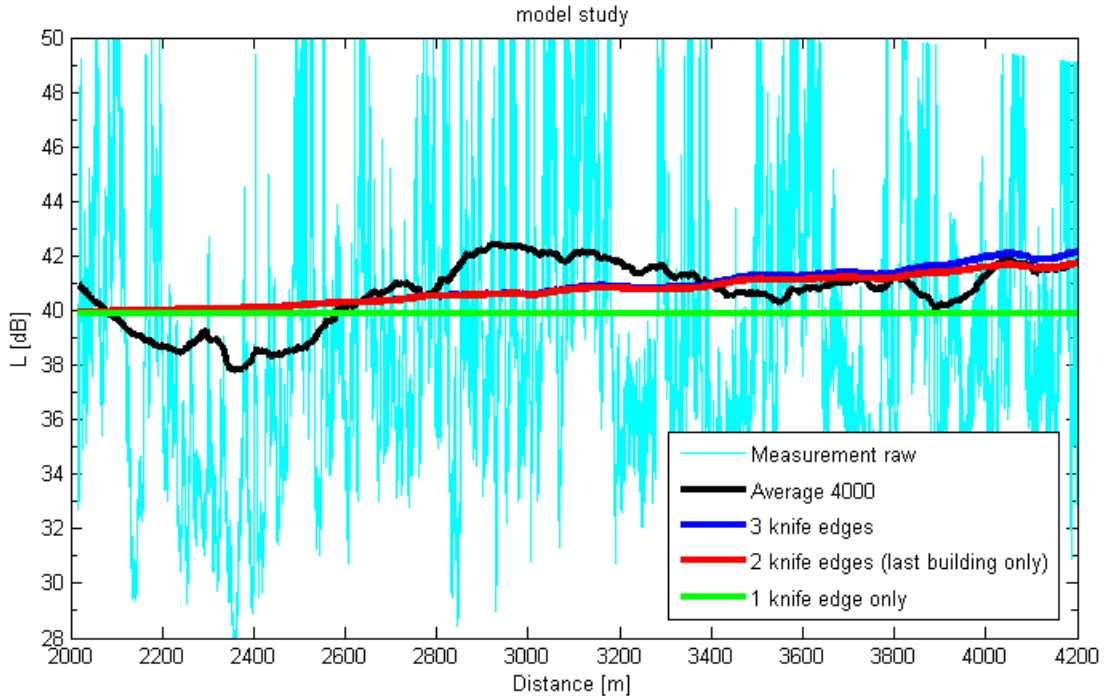
Figure 4.10: Model and measured data (row excess loss and filtered), "location #2", flight 1f.

4.2 New excess loss model

4.2.1 Basic approach

As a first step, a study on link geometry was performed to estimate the number and shape of possible obstacles. Unlike the terrestrial case, where multiple diffraction effects on the rooftops of several consecutive buildings must be taken into consideration due to the grazing angles involved, the last building in the path (the one closest to the receiver terminal in the direction of the UAV) is the only diffracting element to be taken into consideration. This last building can be well approximated by two adjacent knife edges. Additionally, it is important to include the effect of the ray reflected on the opposite side of the street. The power sum of these two rays provides an excellent approximation for estimating the excess loss. Moreover, for the diffraction study, this model was put in the context of other well-known models, mainly for terrestrial links, where from two to four rays are identified to have a significant influence on the excess loss. These additional rays will, in this case, have an impact on the slow and fast variations undergone by the signal.

To find a suitable method to model the excess loss, the physical mechanisms involved were considered. The main factor influencing the excess loss is diffraction. Following the well known COST 231 Walfisch-Ikegami model (section 2.2.3), the propagation path between transmitter and receiver can be broken down into two parts, each being affected by different diffraction mechanisms. Also in the proposed model, initially, the total contribution is divided into two components: the diffraction loss due to the last building, L_{lb}, and the diffraction loss due to the various buildings between the transmitter and the

last building, L_{rt} (roof tops), which are included the first Fresnel zone. Each of these two components should be computed separately, the total excess loss being their sum, i.e.:

$$L_t(dB) = L_{lb} + L_{rt} \tag{4.1}$$

This approach is used in several semi-empirical models such as the Flat Edge Model by Saunders [41], the Walfisch-Bertoni model [19], or the already mentioned Walfisch-Ikegami (COST 231) model.

4.2.2 Path-loss due to the last building

There are several methods which can be used to model the diffraction due to a building. In this case, the buildings of interest are old brick apartment buildings of about 22 meters in height with gable (triangular) roofs. These buildings are complex in shape with many non-uniformities such as windows, roof windows, chimneys, etc. Their effects will be considered statistically as pertaining to the slow variations superposed on slower ones included in the excess loss.

UAV links are unique in the short distances from the receiver to the obstructing edge. Most previous works assume that the distance between receiver and obstruction, and between transmitter and obstruction (d_1, d_2, Fig. 4.11) are much larger than the obstruction height (h). In this case, d_1 is much larger than h but d_2 is usually of similar or smaller magnitude than h. Hence, the last building cannot be modeled by means of a single knife-edge obstruction located in its center.

As a first step a UTD method was applied to a rectangular shaped building and then for a wedge with different rooftop angles. However, the modeled excess loss was overestimated and does not agree with values from the measurement. The values matching the measurement's correspond to a wedge with an angle of 17°. Moreover, the UTD method is computation demanding and one of the initial objectives was to develop a semi-empirical model with an easy-to-use formulation.

Another solution which takes into account the short distances from receiver to obstruction is proposed in Rec. ITU-R P.526 [11], which suggests modeling the building by means of two knife edges on both outer walls, Fig. 4.11.
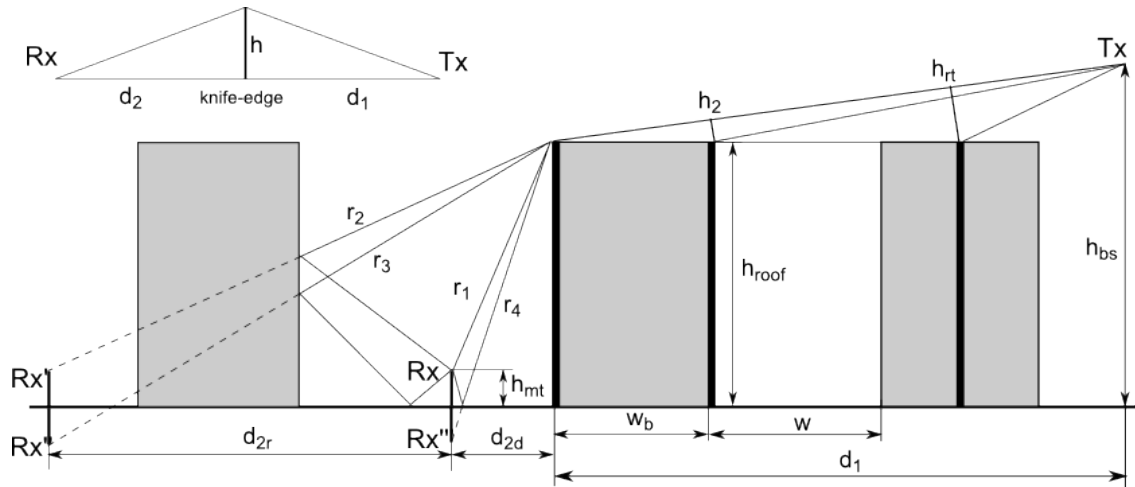

Figure 4.11: Overall propagation scenario and possible diffracted and reflected paths.

The excess attenuation due to the nearest building can be calculated using an approximate multiple knife-edge diffraction approach, Deygout's method being the optimum for the case where one edge dominates over the other [14]. This approximation identifies a main diffracting edge, the one closest to the receiver in this case, giving rise to a loss L_{lb1}. To this it is needed to add the attenuation due to the secondary knife-edge, L_{lb2}, which affects the line of sight between the top of the first knife-edge and the transmitter. The overall excess loss is thus given by

$$L_{\text{lb}}(\text{dB}) = L_{\text{lb1}} + L_{\text{lb2}} \tag{4.2}$$

So far, only one of the possible paths has been analyzed, however, the received signal at street level may be composed of many rays; of those, the most significant ones (Fig. 4.11) are [6] the direct ray (r_1) reaching the receiver after being diffracted on the building on the transmitter side, and two possible specular reflected rays, one on the building on the opposite side of the street (r_2) and another on the ground (r_4). These two contributions also undergo diffraction before being reflected. Another possible reflected contribution would be one suffering a double reflection on the building opposite and on the ground (r_3). As in [6] [18], for assessing, the excess loss can be considered as the power sum of the direct and one or more of the three reflected rays just discussed, Fig. 4.11. The general formula for the average received field, E, i.e., taking into account all possible reflections, can be expressed as a root mean square of the field strengths of components taken into consideration, as proposed Ikegami [18], i.e.,

$$E(\text{dBV/m}) = 10 \log \left(\sum_{n=1}^{4} e_n^2 \right) \tag{4.3}$$

The intensities in linear units are represented by lower-case letters and when in logarithmic units capital letters are used. In this paper the excess loss, L (dB), will be used instead of field strength, E, i.e.,

$$L(\text{dB}) = -10 \log \left(\sum_{n=1}^{4} \frac{1}{10^{\frac{L_n}{20}}} \right) \tag{4.4}$$

Thus, the general expression for the excess loss resulting from the combination of the four rays considered, all undergoing diffraction on the closest knife-edge on the transmitter side of the street is given by

$$L(\text{dB}) = -10 \log \left(\frac{1}{10^{\frac{L_1}{20}}} + \frac{r_{\text{b}}^2}{10^{\frac{L_2}{20}}} + \frac{r_{\text{b}}^2 r_{\text{g}}^2}{10^{\frac{L_3}{20}}} + \frac{r_{\text{g}}^2}{10^{\frac{L_4}{20}}} \right) \tag{4.5}$$

where the $L1$ to $L4$ (dB) are the diffraction attenuations affecting the individual rays, r_{b} (linear) is the magnitude of the building reflection coefficient and r_{g} is the magnitude of the ground reflection coefficient.

The excess loss caused by diffraction can be computed using Fresnel integrals [10]. For this geometry where the building height, h_{roof}, is larger than the street width, w, the normalized obstruction parameter,ν, is greater than 10; in this case the following approximation of the Fresnel integrals can be used,

$$\frac{e}{e_0} = \frac{0.225}{\nu} \tag{4.6}$$

where e is the actual received field and e_0 is the free space under line of sight conditions. The above expression in terms of the excess loss and in dB, is given by

$$L(\text{dB}) = -20 \log \left(\frac{0.225}{\nu} \right) \tag{4.7}$$

which shows a perfect agreement for $\nu > 2.5$. In general, the parameter v is defined as [11]

$$\nu = h \sqrt{\frac{2}{\lambda} \left(\frac{1}{d_1} + \frac{1}{d_2} \right)} \approx h \sqrt{\frac{2}{\lambda d_2}} \tag{4.8}$$

where its elements are graphically depicted in Fig. 4.11. The approximation is valid when $d_2 \gg d_1$.

As an approximation, out of the three reflected rays, only the wall reflected ray will be considered, i.e., ray r_2. Then the level and evolution of the notably slow variations is reproduced, i.e., smaller scale features have been removed. Unless the disagreement between measurements and model is unacceptable, further rays will not be introduced to keep the model simple. Also in [18] only two rays, the direct and the reflected, were considered.

For the main diffracting edge, $h \approx h_{roof} - h_{\text{mt}}$ and $d_2 \approx d_{2d} \approx d_w$, for direct ray and $d_2 \approx d_{2r} \approx (2w - d_\text{w})$, for reflected ray (Fig. 4.11). Therefore, using (4.7) and (4.8) a final form of the last building's main knife-edge attenuation L_{lb1} can be written as,

$$L_{\text{lb1}}(\text{dB}) = -10 \log \left[\frac{0.05\lambda}{2(h_{\text{roof}} - h_{\text{mt}})^2} (d_\text{w} + R_\text{b}^2(2w - d_\text{w})) \right] \tag{4.9}$$

The parameters for calculating the diffraction loss due to the second edge (secondary edge) can be computed following Deygout's method (Fig. 4.11). In this case, the excess height parameter, ν, for the second edge is negative. Here, a simple exponential approximation of the Fresnel Integral will be used which ignores oscillations in the field strength for $\nu < -1$, i.e.,

$$L_{\text{lb2}}(\text{dB}) = -20 \log(1 - e^k) \tag{4.10}$$

which shows sufficient agreement for $\nu < 0$, and where

$$k = -0.6038 \cdot 0.1094^\nu \tag{4.11}$$

with ν as defined in (4.8). The inverse of distance d_1, $1/d_1$, can be neglected; d_2 is represented by w_b, and h_2 (Fig. 4.11) is given by

$$h_2 \approx -w_\text{b} \sin \left(\tan^{-1} \left(\frac{h_{\text{bs}} - h_{\text{roof}}}{d - d_\text{w}} \right) \right) \tag{4.12}$$

The diffraction parameters for ray r_2 (and rays r_3 and r_4 if necessary) can be calculated in a similar way by considering the appropriate images of the receiver with respect to either the wall on the opposite side of the street or the ground.

4.2.3 Diffraction at multiple rooftops

For this scenario, given the low elevation angles involved, it might be necessary to take into account the additional diffraction loss introduced by the multiple buildings between the transmitter and the building nearest the receiver. This term is often found in propagation models such as the Walfisch-Ikegami (COST 231) model.

Given the geometry depicted in Fig. 4.11, where the elevation angle from the top of the last building may go from 1.4 to 5.6 degrees at most, it will be necessary to consider only one additional rooftop in the direction of the transmitter. All additional edges will introduce a negligible increase in the attenuation. Due to the large distances from the obstacle, it can be used a standard representation of the building by means of a knife-edge in the middle of the building. In this case, the excess height, h_{rt}, will also show negative values. Thus, the same method will be used as in the second knife-edge belonging to the last building, i.e.,

$$L_{\text{rt}}(dB) = -20 \log(1 - e^k) \tag{4.13}$$

where k is defined in (4.11) and ν in (8) (Fig. 4.11), h is given by

$$h_{\text{rt}} = -(1.5w_{\text{b}} + w) \sin \left(\tan^{-1} \left(\frac{h_{\text{bs}} - h_{\text{roof}}}{d - d_{\text{w}}} \right) \right) \tag{4.14}$$

the inverse distance, $1/d_1$, can be neglected and d_2 is equal to $1.5w_{\text{b}} + w$.

As said, the complete approach has been described above for completeness; however, some of the above terms are negligible and will be disregarded in the final model after its verification and validation.

4.3 Model verification and validation

4.3.1 Model verification

Before going on to compare measured data and model predictions, the heuristic approximations were verified for diffraction included in the proposed model, i.e., Deygout's approach. Thus, the guidelines in [42] were followed where the Fresnel-Kirchhoff (F-K) theory is applied to vertical 2D profiles using a par-axial approximation and performing a discrete integration over each successive screen (knife-edge). For this purpose the Matlab codes provided in [26]were modified and adapted to the UAV link geometry. Fig. 4.12 sketches the simulated scenario. The receiving antenna was kept at a constant height of 1.5 m while a UAV flight was simulated at a constant height of 150 m for a distance range from 1.2 to 4 km.
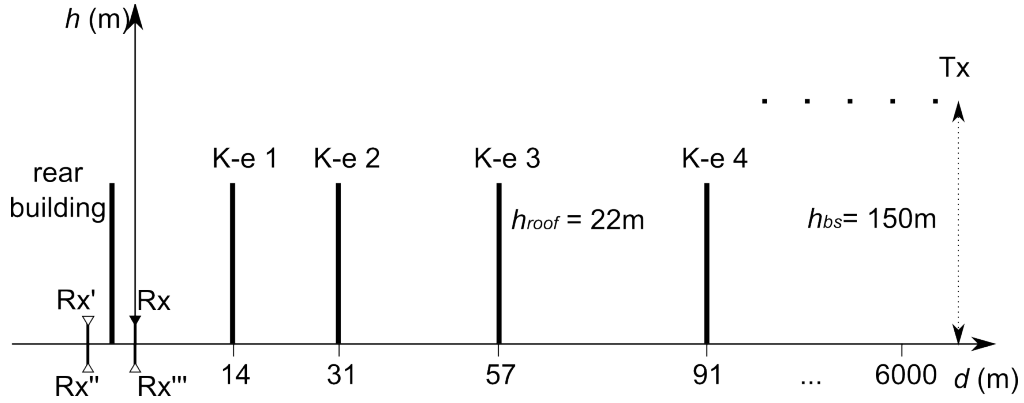
Figure 4.12: Simulated scenario using our model and F-K.

Fig. 4.13 shows a comparison between the predictions with the proposed model and those obtained using F-K for the direct ray only. It can be observed how the agreement between the F-K simulations for two edges is within one dB of our model's prediction assuming 2 edges. The figure also shows how introducing a third edge does not change the prediction. In the F-K calculations, introducing one or two further edges changes the loss only slightly. Thus, it can be concluded that, for the geometry under consideration, two edges should provide a reasonably good prediction.
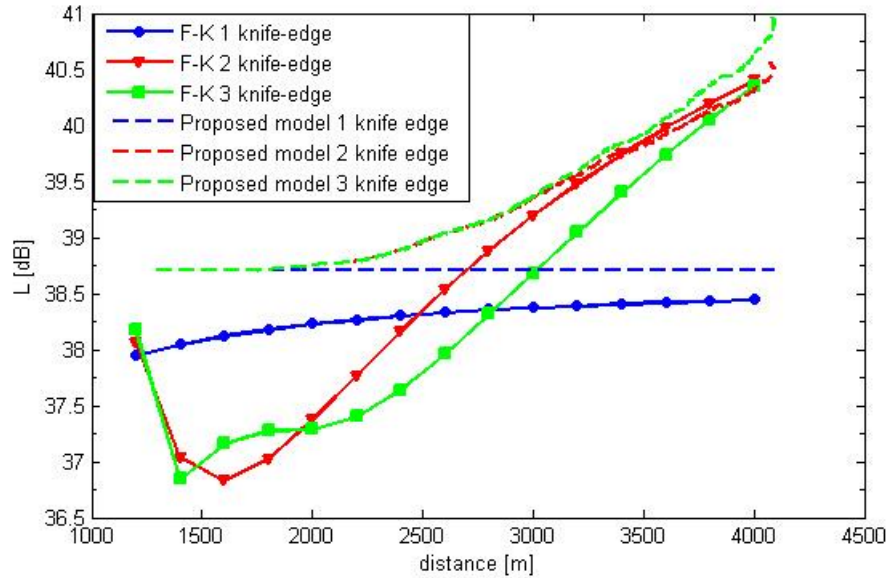

Figure 4.13: Evaluation of the importance of including more diffracting edges for assessing the direct signal level in our model and for F-K.

The difference between the F-K simulation and our model for only one knife-edge, where their values should follow the same trend, can also be noticed. This difference is due to the simplification in the expression for the ν parameter,(4.7), for the first diffracting edge. The theoretical gain of the knife edge diffraction for $\nu < 0$ [15] was not considered. As said before, this is for keeping the model as simple as possible.

Now, in Fig. 4.14, the model was analyzed assuming two rays, the direct and a reflected ray on the building on the opposite side of the street. Only two and three diffracting edges were considered in this case. In the figure it can be seen how the model and the F-K calculations tend to produce similar results for the longer simulated distances. For the shorter distances the error is no larger than 1.5 dB, considered to be acceptable, since there is a need for developing a simple mode valid for the whole distance range, with special emphasis on the longer distances (> 3 km).
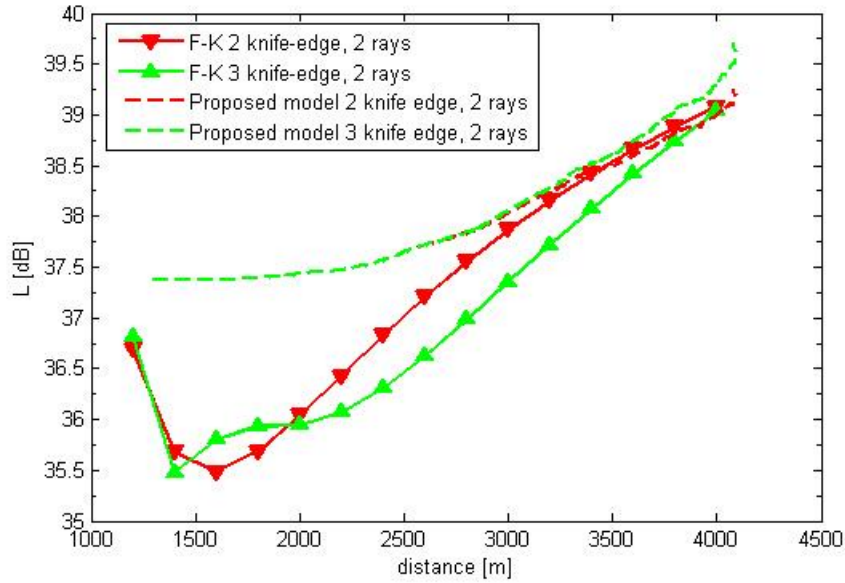

Figure 4.14: Comparison between our model and F-K for two and three diffracting edges, assuming two rays: direct and reflected.

4.3.2   Model validation

To verify the model, the excess loss from the low-pass filtered measured data was compared with predictions using the proposed model using only rays r_1 and r_2. Already in Fig. 4.10 measured excess losses are shown for test flight 1f, Rx location#2 (closest to the nearest building). The figure also shows predictions made assuming one, two or three diffracting edges. A very good agreement between the measurements and the predictions is shown in all three diffraction configurations. However, it is clear that introducing a third diffracting edge does not improve the prediction.

In the same way, in Fig. 4.15 the same flight path for Location #1 is shown (furthest from the nearest building in the direction of the transmitter). Observing both Fig. 4.10 and Fig. 4.15, a significant gain of about 5 dB can be noticed with increasing distance from the first building.
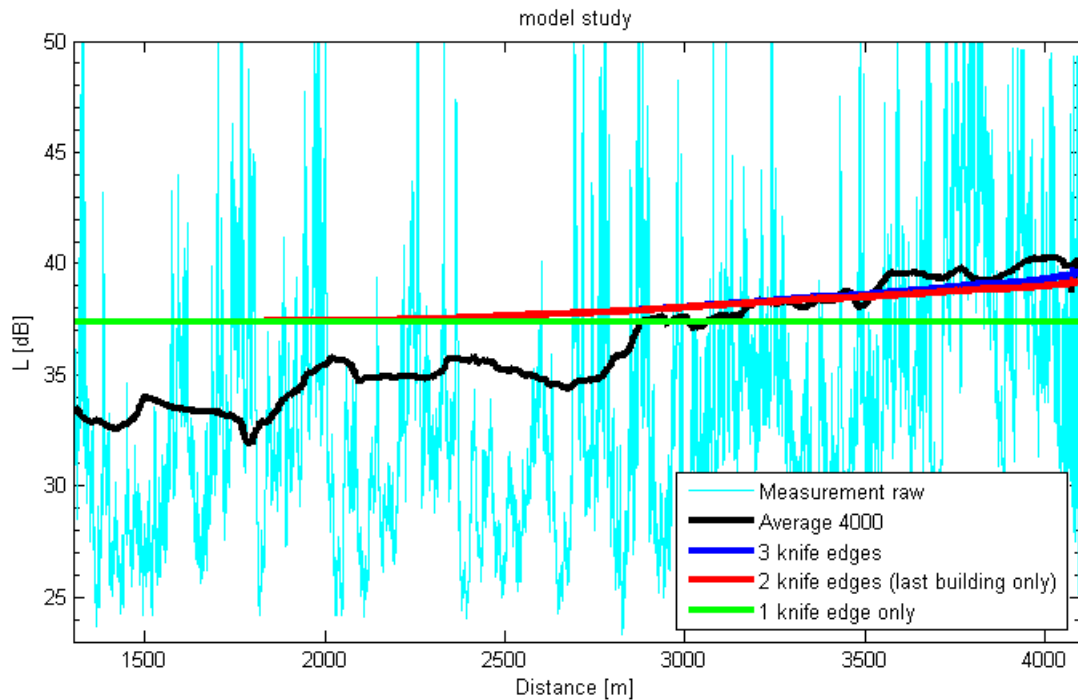
Figure 4.15: Model and measured data (raw excess loss and filtered). Location #1, flight 1f.

As for the differences between predictions and measurements in Fig. 4.15, an excellent match can be observed for distances in excess of 2.5 km, i.e., for the lowest elevations in the considered range. Differences not exceeding approximately 5 dB can be observed for shorter distances, i.e., for the highest elevations in the range under study. The model predicted higher losses than the actual ones. These differences could be compensated for by including rays r_3 and r_4. However, the goal is to develop a simple model providing accurate predictions throughout the elevation angle/distance range of interest, and the accuracy achieved is acceptable. This can also be confirmed by the results in Tab. 4.3, as discussed next.

Location#1	ME (dB)	STD (dB)	Path Length (m)
1f	-1.67	2.51	2810
2f	-0.42	1.35	2285
2b	1.54	2.42	1490
3f	-0.42	0.85	2154
3b	1.19	1.62	2800
Overall #1	-0.15	2.71	11539
Location#2	ME (dB)	STD (dB)	Path Length (m)
1f	-0.11	0.97	2158
2f	-0.01	0.79	1719
2b	1.29	2.28	877
3f	0.09	1.26	2046
3b	0.22	1.30	2328
Overall #2	0.29	1.70	9128
Overall #1&#2	0.06	2.20	20667

Table 4.3: Comparison results with objective parameters

The values in the table show good general agreement between the measured data and model. There are deviations caused by the slow and very slow variations which cannot be predicted with this model, but the model follows the observed trend quite well in its entirety. As in Fig. 4.15, the errors become larger for the highest elevations contained in the various flight paths. However, the overall error statistics are quite good, which leads us to accept the simplest model configuration, i.e., two diffracting edges and two rays: direct and wall reflected.

4.4 Conclusions

In this chapter the results from a measurement campaign were presented simulating typical conditions in UAV high data rate communication links in urban areas at frequencies of about 2 GHz. The concentration was set on assessing the average signal loss expressed as the excess loss with respect to free space, and its variations with distance and elevation. Also, two possible control station locations at street level within the urban area have been considered, one close to the nearest building in the direction of the UAV and the other on the opposite side of the street. A model based on existing models for terrestrial macro-cells for excess loss has been developed, although the elevation angles involved are larger in this case. The proposed model is a combination of diffraction on the nearest building and reflection off the building opposite. Building diffraction has been modeled by assuming two knife-edges set on both external walls of the building under consideration. Unlike in terrestrial links where grazing incidences are usual, no further buildings need to be taken into account.

The model was published in [38].

Chapter 5

Channel model

In this section the UAV propagation channel is analyzed together with the possible use of well-known models, even though the link is different from those of satellite and terrestrial links. Also, methods to generate a synthetic, received signal time-series for simulation purposes were analyzed. It was found necessary to develop a new time-series generator based on existing ones but fitting the dynamics of the channel in hand better.

As in the previous chapter such research needed to be based on a valid experiment. Therefore a measurement was conducted in an urban area for analyzing and then synthesizing purposes.

The core of this chapter was published in [43] so that parts of the text may be identical.

5.1 Experimental trials

In this part the measurements are described. The measurement equipment was the same as in the case of path-loss modeling.

5.1.1 Measurement setup

For the statistical analysis, different flight route had to be set to reach a variety in received signal corresponding to the worst case scenario in the surveillance operations in urban areas. The airship followed linear routes from 1 to 6 km distances and flight levels from 100 m to 170 m above ground (Fig. 5.1). From the receiver station the UAV was seen under elevation angles from approximately 1 to 6 degrees.

The configuration allowed the observation of variations in the shadowing conditions while the first configuration allowed us to keep a fairly constant geometry to look into the evolution of the path-loss. The shadowing conditions were, in general, fairly homogeneous, at least in the measurements performed, thus having the received signal in the same "state" (as in state oriented models section 2.4.4.). State variations are more likely to occur when the UAV is close to the receiver; in this case the path loss is likely to be dominated by a single urban feature: a building or a crossing. Further away, the observed shadowing is more likely to be due to a combination of several features at different distances along the radio path. This is likely to even out possible strong signal variations and produce a rather homogeneous series.

The effect of antenna radiation pattern distortion will be more important in this measurement and it cannot be separated from that of the propagation channel itself, without the antennas, though it represents realistic conditions. It must thus be borne in mind that the results presented in the sections below include the antenna pattern distortion effects. In general, a multipath channel is dealt where the angles of arrival will be very much uniform in azimuth, this should even out the peak-to-peak variations in the individual antenna radiation patterns.

The receiver was set at three different locations (Fig. 5.2). The first position "location #1" was in a street canyon close to the buildings. The second position "location #2" was a similar location in a neighboring street, with different orientation with respect to flight track. The third position "location #3" was in a small square in the same area.
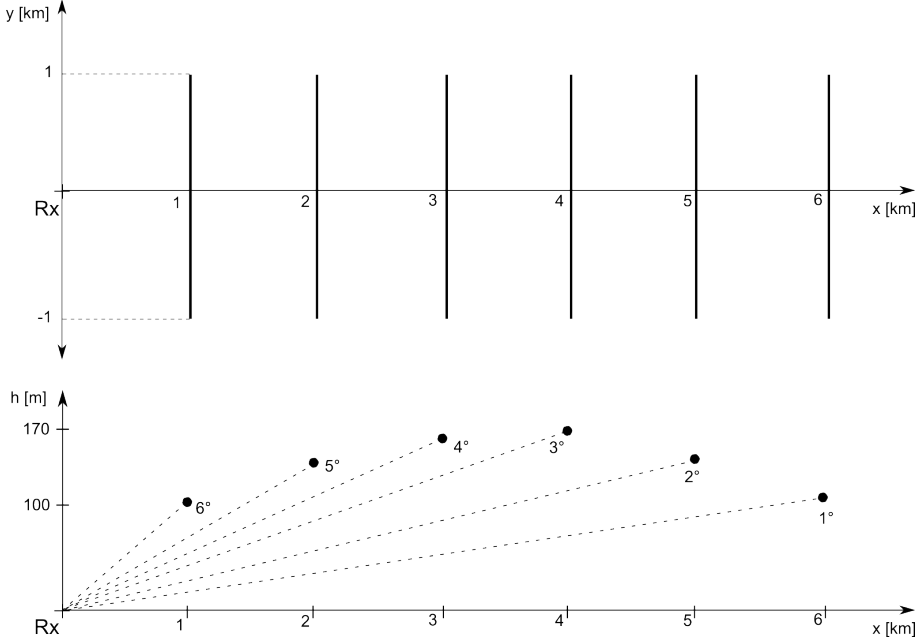

Figure 5.1: Flight routes

Figure 5.2: Receiver locations #1, #2 and #3 (image from Google Earth), in Dejvice, city of Prague.

The expected width of Doppler spread was low given that the radius of the ring of scatterers (mainly the street-side buildings and parked cars) around the static receiver would normally be limited by the width of the street while they trace a very small angular sector (2Δ deg., Fig. 5.3) toward the moving, far away transmitter. The Doppler spread values, obtained from calculations, did not exceed a few Hz in the worst-case scenario, which, when compared with the used sampling rate of 100 Hz, allowed us ample room for capturing the deep nulls in the signal. This was so while operating within the dynamic range of the receiver. Those flight sections where the signal went below the noise threshold were discarded in the analysis. Fig. 5.3 illustrates the assumptions made in the calculations of the expected Doppler spread.
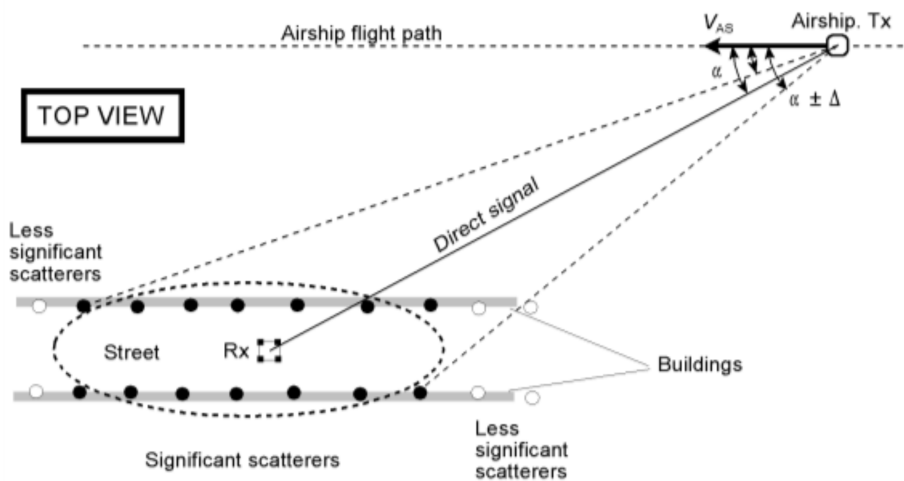

Figure 5.3: Geometry of the link to calculate the expected Doppler spread.

The Doppler shift depends on airship speed, $V_{\mathrm{AS}} \approx 8$ m/s, transmission wavelength, $\lambda \approx 0.15$ m and the angle of the direct signal with respect to the airship's velocity vector, α deg., i.e.

$$f_{\mathrm{shift}} = \frac{V_{\mathrm{AS}}}{\lambda} \cos(\alpha) \tag{5.1}$$

The largest Doppler shift is observed at the ends of the nearest flight, where $\alpha \approx 45$ deg., in this case $f_{\mathrm{shift}} \approx 37.7$ Hz.

As for the Doppler spread, a key factor in the rate of change of the fades, it is given by

$$\Delta f_{\mathrm{spread}} = \frac{V_{AS}}{\lambda} |\cos(\alpha - \Delta) - \cos(\alpha + \Delta)| \tag{5.2}$$

Assuming that the most important scatterers are within a 50 m radius of the receiver, angle Δ for the nearest flight, at the starting point, is

$$\Delta = \tan^{-1}\left(\frac{50}{\sqrt{1000^2 + 1000^2}}\right) = 2.02 \quad (\mathrm{deg.}) \tag{5.3}$$

this means that the Doppler spread in Hz is

$$\Delta f_{\mathrm{spread}} = \frac{8}{0.15} |\cos(45° - 2.02°) - \cos(45° + 2.02°)| = 2.66 \tag{5.4}$$

It can be concluded that the available sampling rate, 100 Hz, is more than enough to capture the fading variations as their rate is driven by very small Doppler spreads.

5.1.2 Data processing

Unlike path-loss modeling where all fast variations in a received signal were removed by averaging, here these variations are needed for channel analysis. Hence, a path-loss is computed from received power by similar methods as in path-loss modeling, but without any averaging. Also the data were checked for high pitch and roll values. Instead of working with path-loss or excess path-loss values throughout the analysis path-gains, R and r are used, where

$$R(\mathrm{dB}) = P_{\mathrm{r}}(\mathrm{dBm}) - P_{\mathrm{rFS}}(\mathrm{dBm}) \tag{5.5}$$

and

$$R(\mathrm{dB}) = 20 \log(r) \tag{5.6}$$

with P_r the actual received power in dBm, P_{rFS} the received power in dBm under free space conditions. Parameter R is the excess path gain or normalized signal level in logarithmic units, while r^2 is the path gain in linear units, where r is the received voltage normalized with respect to that of line-of-sight conditions. In the following sections the complex version of r,$\tilde{r}$, i.e. the narrow-band complex envelope will be simulated.

5.2　Statistical analysis

First of all, it is worth taking a close look at the measured series which are designed to characterize and simulate/synthesize. An example of measured path-gain series is shown in Fig. 5.4. Strong, slow variations of "arch"- like shape are observed, with each arch being approximately 30 wavelengths long. Superimposed on these slow, large-scale variations are other, faster ones. The fast variations present a small dynamic range with higher peak-to-peak excursions when they are superimposed on low level, slow-varying signals while, when the overall signal shows higher levels, the fast variations present smaller peak-to-peak ranges.
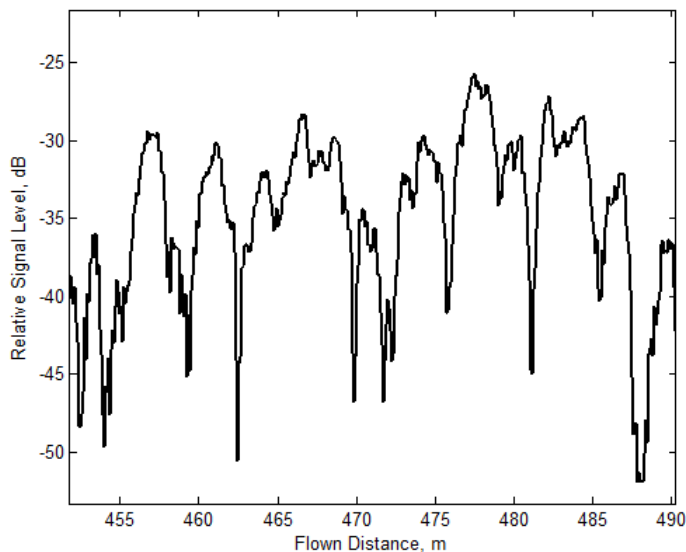

Figure 5.4: Path gain sample. Location 1, Flight 3km

The possibility of diffuse scattering from the rear building was studied in this geometry. A sum of contributions from many small plates using a unit-surface radar cross section was simulated in a Matlab environment but the variations in signal were negligible mainly due to a small change in incident angles. Hence, it can be stated that diffuse scattering does not have an influence on variations in received signal.

The geometry of this link is somewhere between that of terrestrial and LMS links. In the LMS case the received signal is assumed to be made up of the direct and multipath components. The direct component may be subjected to different levels of shadowing while the multipath component interferes with (coherently adds to) the direct signal giving rise to fast variations. The received complex envelope can be pictured as the complex sum of two phasors: direct and multipath, i.e.

$$\tilde{r} = r \exp(j\Phi) = r_{\mathrm{D}} \exp(j\Phi_{\mathrm{D}}) + r_{\mathrm{M}} \exp(j\Phi_{\mathrm{M}}) \tag{5.7}$$

In terrestrial links these assumptions are not used, especially in urban areas. The direct, LOS signal is normally not present and the overall received signal is assumed to be completely due to multipath whose average power changes slowly, i.e.

$$\tilde{r} = r \exp(j\Phi) = r_{\mathrm{M}} \exp(j\Phi_{\mathrm{M}}) \tag{5.8}$$

In the LMS case, different "states" or shadowing/blockage conditions are possible. In the "good state" there is normally a direct signal subjected to zero or limited shadowing effects. In the so-called "bad state", the direct signal is still present but may be comparable to or smaller than the multipath, i.e., k-factors normally below 0 dB.

An intermediate type of link was observed here where the preliminary analysis showed that negative k-factors were not very frequent. Thus, an analysis was carried out assuming that, locally, the received signal is Rice distributed with generally low k-factor values. The Rice distribution assumes the presence of a strong, coherent component plus a diffuse contribution. The coherent component, here sometimes called the direct signal, is a ray subjected to diffraction over multiple rooftops plus street-side tree shadowing.

Having made the Rice assumption, calculating the local/short-term Rice parameters by using the Method of Moments, MoM, is described in [44] as follows.

The MoM requires the signal to be windowed into sections of homogeneous characteristics so that the values of a and $2\sigma^2$ can be considered constant. There is a trade-off between window length, which should preferably be as small as possible, and the number of samples in a window, which should be large enough to compute statistically significant parameters. It was finally observed, by trying different window sizes, that a length of 0.26 s or, equivalently, 2.08 m (assuming an average flight speed of 8 m/s) fulfilled the requirements.

Moments in this context correspond to the "moments" of the measured series, more specifically, its mean and the standard deviation. The normalized absolute value of the complex envelope is r, the normalized power is then, $p = r^2$. Two intermediate parameters are calculated, G_m and G_v, corresponding to the mean and standard deviation of p for overlapping sections or windows of 0.26 s or, equivalently, 2.08 m, i.e.

$$G_{\mathrm{m}} = \mathrm{mean}(W(p)) \tag{5.9}$$

and

$$G_{\mathrm{v}} = \mathrm{std}(W(p)) \tag{5.10}$$

where W indicates the windowing operation. The results are two series of intermediate parameters G_m and G_v values. From these the Rice distribution parameters can be calculated for the section of data inside each window, i.e.

$$a^2 = \sqrt{G_{\mathrm{m}}^2 - G_{\mathrm{v}}^2} \tag{5.11}$$

and

$$\gamma = 2\sigma^2 = G_{\mathrm{m}} - \sqrt{G_{\mathrm{m}}^2 - G_{\mathrm{v}}^2} \tag{5.12}$$

The results are a series of a and γ values, representing the "local" direct signal amplitude and multipath power. Since the window slides over the original measurement, the resulting parameters are obtained with the same time/space resolution, i.e. the sampling rate. The carrier-to-multipath ratio or k-factor series is given by

$$k = \frac{a^2}{2\sigma^2} = \frac{a^2}{\gamma} \tag{5.13}$$

The above parameters in logarithmic units are as follows,

$$A(\text{dB}) = 20 \log(a) \tag{5.14}$$

and

$$\Gamma(\text{dB}) = 10 \log(2\sigma^2) = 10 \log(\gamma) \tag{5.15}$$

where Γ and γ stand for multipath power.

Problems occur when the MoM technique is applied to very sharp signal transitions. This problem was overcome by interpolating reliable parameters on both sides of a transition, however, sharp transitions were rare. The time-series of the above two parameters was obtained from the MoM method, an example of which is shown in Fig. 5.5. analyzing the distribution of A (dB) and Γ(dB). The analysis of A yielded a sufficient fit to the normal distribution (log-normal for the amplitude of the direct signal, a, in linear units) as shown in Fig. 5.6. For some flights, a better fit was found for the Rayleigh distribution (linear units, also shown in Fig. 5.6 in dB). In the figure a logarithmic scale was used on the ordinate axis (probabilities) so as to have a better look at the lower tail of the distribution. The normal distribution fit is better when considering very low probability levels and then it diverges.

A log-normal distribution implies the product of numerous random attenuators, i.e., multiple diffracting rooftop edges, other elements on the rooftops, trees, etc., whereas the Rayleigh hypothesis implies the coherent sum of several (at least six or so) random phasors of approximately the same magnitude and, in general, stronger than those included in the incoherent part. In chapter 4 a path-loss model was presented where a maximum of four "stronger"/deterministic contributions may be present, as illustrated in Fig. 5.7. Which goes along with conclusions from [45]. Simple calculations have, however, shown that, at most, only two rays actually contributed significant power. Moreover, geometrically, it is difficult to explain how these contributions may be drifting in phase fast enough to give rise to fast-varying interference effects following a Rayleigh distribution.

Thus the log-normal hypothesis was pursued after verifying that the obtained results yielded a good agreement both in the first- and second-order statistics, as shown in the next section where the time-series generator is described.
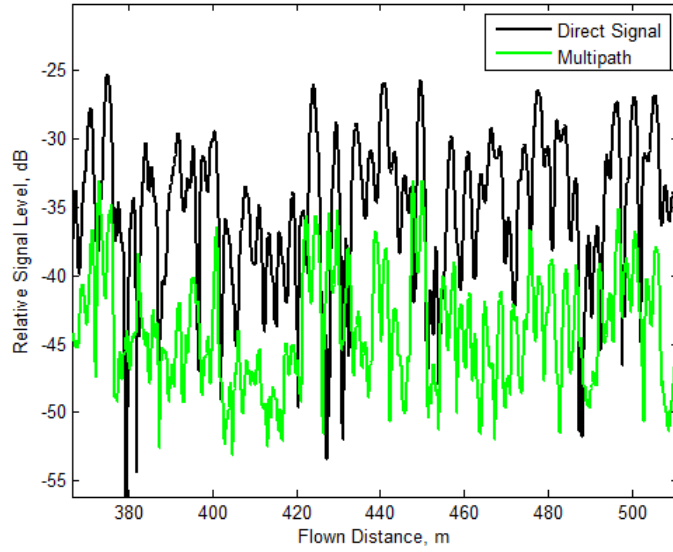
Figure 5.5: Evolution of A and Γ parameters for the time series in Fig. 5.4 ("location #1", flight #3) obtained with the MoM
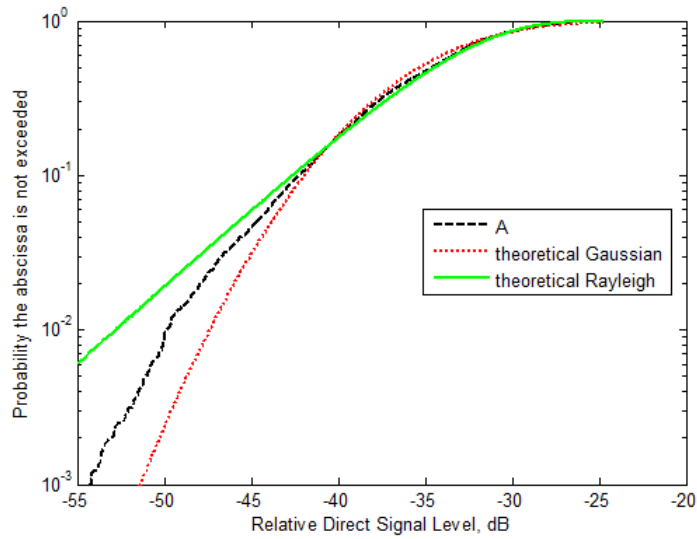

Figure 5.6: Measured and fitted Gaussian and Rayleigh distributions for the variations of A (dB) for location 1, flight 3km.
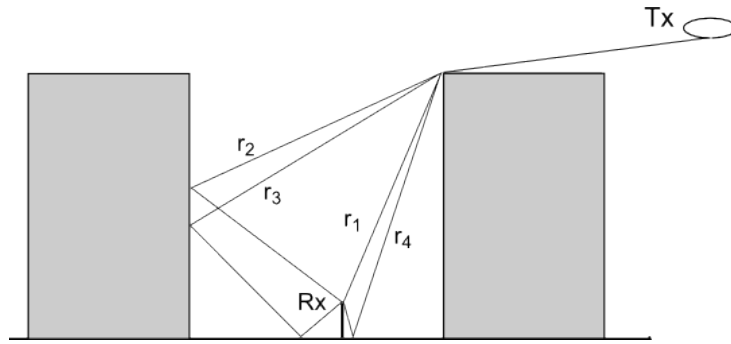
Figure 5.7: Four-ray sum scenario

Then the rate of variation of A was characterized; this is given by the autocorrelation function. Fig. 5.8 shows this function for one of the flights. Superimposed there are also shown a Gaussian and an exponential models. A better fit can be observed for the Gaussian model, i.e.

$$\rho_A(\Delta t) = \exp\left(-\frac{\Delta t^2}{2\xi_A^2}\right) \tag{5.16}$$

where $\rho(\Delta t)$ is the autocorrelation coefficient for time-lag Δt and where ξ_A is the correlation time in the variations of $A(\text{dB})$. Note in Fig. 5.8. how correlation times were replaced with correlation distances. The conversion between time-lags and distance-lags can be performed using the airship speed as a conversion constant. There is a particular interest in performing the study in the traveled distance domain since the speed used in the measurements may be completely unrealistic for some UAV applications. However, conversion from distance units to time units for different speeds is straightforward.
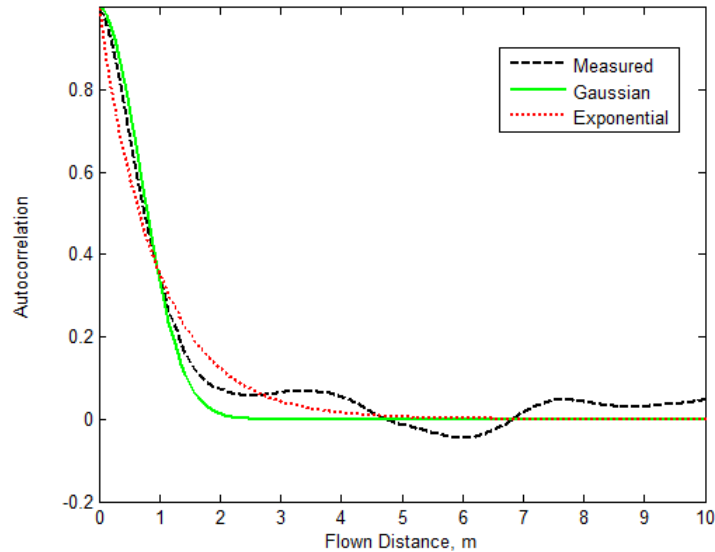

Figure 5.8: Measured and fitted Gaussian and exponential models for the autocorrelation in the variations of A (dB) for "location #1", flight #3.

Next, the results for the time-series of Γ (dB) are presented. Like in the case of A, a fairly good fit to the Gaussian distribution was observed as exemplified in Fig. 5.9 .
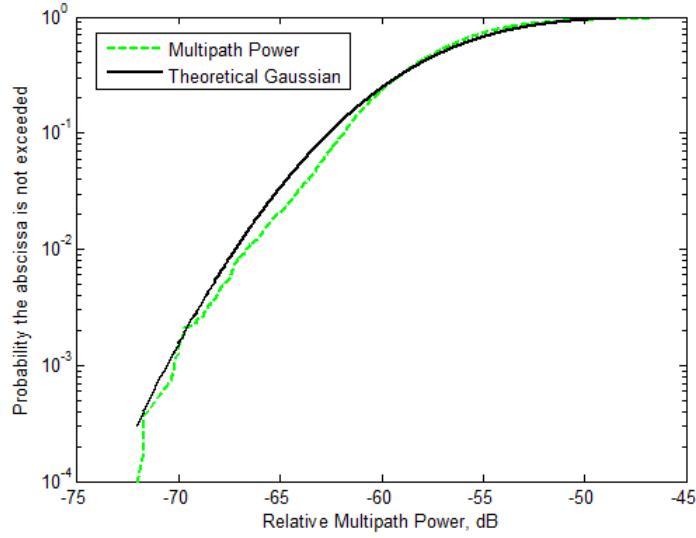

Figure 5.9: Measured and fitted Gaussian distribution for the variations of Γ (Multipath Power) (dB) for location 1, flight 3.

The fit is quite good down to the lower probability levels in the tail of the distribution. In a similar way to A, the autocorrelation function was also computed and fitted to a Gaussian model (Fig. 5.10), i.e.

$$\rho_\Gamma(\Delta t) = \exp\left(-\frac{\Delta t^2}{2\xi_\Gamma^2}\right) \tag{5.17}$$

where ξ_Γ is the correlation time in the variations of Γ(dB). Again time and space are related by the airship speed, and it is more convenient to work in the distance domain as it allows extrapolation to other speeds. The fit is reasonably good at least down to a value of 0.3, including the 1/e mark where the correlation distance/time is evaluated.
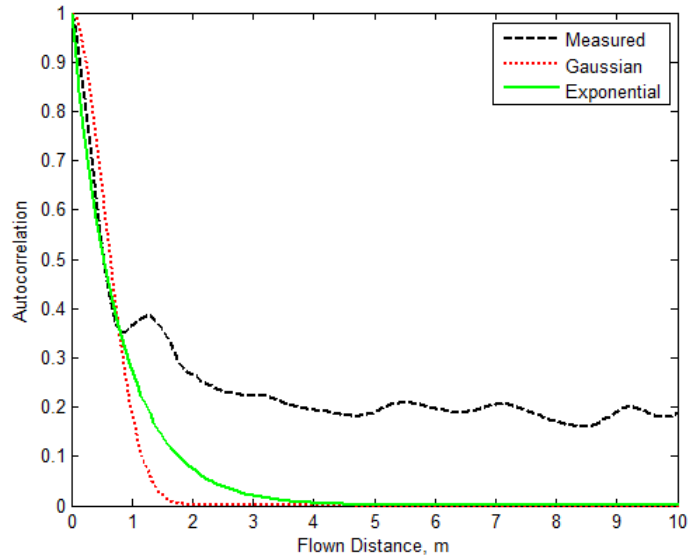
Figure 5.10: Measured and fitted Gaussian and exponential models for the autocorrelation function in the variations of Γ (dB).

Finally, the interdependence between the variations of all A and Γ was studied: the cross-correlation coefficient was relatively low, for example for "location #1", flight #3, the coefficient was 0.29. This is illustrated in Fig. 5.11, where a 2D histogram of A and Γ together with a linear regression fit is shown. The slope of the fitted line is very small confirming their relatively low correlation.
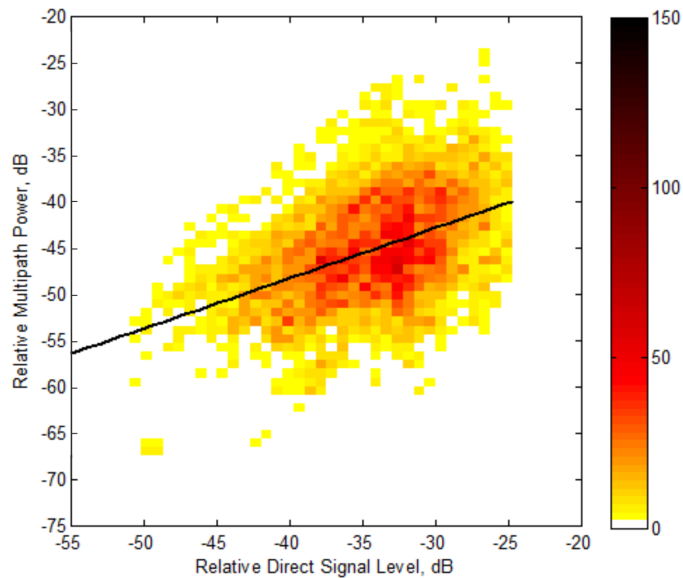

Figure 5.11: 2D histogram of A and Γ pairs ("location #1", flight #3) plus regression derived straight line.

65

In summary, there are Gaussian variations of A and Γ characterized by their respective means and standard deviations, their rate of change can be characterized by means of Gaussian functions, but their correlation times/distances are different, i.e., they fluctuate at different rates. It was considered that A and Γ are not sufficiently correlated to introduce their mutual dependence in a simulator.

Finally, in Tab. 5.1, the ranges for the various parameters are summarized. Location 2 was excluded as the obtained parameters are similar in magnitude to those in location 1 corresponding to a street canyon situation.

Table 5.1: Time series generator parameters overview

Parameter / Flight, km	location 3			location 1			
	3	4	6	3	4	5	6
ξ_A	0.848	0.876	1.700	0.678	0.912	1.018	0.863
ξ_Γ	0.453	0.396	0.679	0.540	0.460	1.004	0.848
Mean A, dB	-31.06	-31.27	-34.15	-34.89	-36.58	-38.50	-38.35
STD A, dB	4.70	4.83	4.16	4.74	4.86	4.50	3.93
Mean Γ, dB	-51.76	-52.85	-54.69	-56.80	-60.51	-62.20	-60.97
STD Γ, dB	3.36	2.65	2.18	3.78	2.77	3.22	3.26
CorrCoeff A, Γ	0.290	0.376	0.418	0.406	0.427	0.546	0.560

5.3 Time series generator

5.3.1 Loo model

The UAV link resembles the one found in the "bad state" LMS channel. In [46] the Loo model is proposed for its versatility for use in any possible LMS shadowing state. Thus, firstly, this model is reviewed and put in the framework of our observations.

In the Loo model[23], the received signal is assumed to vary according to a Rice distribution with parameters a and $2\sigma^2 = \gamma$. This is valid for short route sections (flight sections, in this case). For longer stretches of the route the direct signal's amplitude is assumed to vary according to a log-normal distribution, i.e.,

$$f(a) = \frac{1}{\Sigma_{Np}a\sqrt{2\pi}}exp\left[-\frac{(ln(a)-M_{Np})^2}{2\Sigma_{dB}^2}\right] = \frac{8.686}{\Sigma_{Np}a\sqrt{2\pi}}exp\left[-\frac{(ln(a)-M_{dB})^2}{2\Sigma_{dB}^2}\right] \quad (5.18)$$

where M and Γ are the mean and standard deviation of the normal distribution for the direct signal's amplitude in Nepers (ln) and in dB (20log), where the expression $ln(x) = (20/8.686)\log x$ was used for unit conversion. As in the Rice model, it assumes that the received complex envelope consists of the sum of two phasors.

The overall distribution, i.e., for longer stretches of mobile routes (flights) with homogeneous shadowing conditions, is given by

$$f(r) = \int_0^\infty f(r|a)f(a)da$$

$$= \frac{8.686r}{\sigma^2 \Sigma_A \sqrt{2\pi}} \int_0^\infty \frac{1}{a} \exp\left[-\frac{r^2 + a^2}{2\sigma^2}\right] \exp\left[-\frac{(20\log a - M_A)^2}{2\Sigma_A^2}\right] I_0\left(\frac{ra}{\sigma^2}\right) da \quad (5.19)$$

$$= \frac{(\frac{40}{ln10})r}{\gamma^2 \Sigma_A \sqrt{2\pi}} \int_0^\infty \frac{1}{a} \exp\left[-\frac{r^2 + a^2}{\gamma}\right] \exp\left[-\frac{(20\log a - M_A)^2}{2\Sigma_A^2}\right] I_0\left(\frac{ra}{\gamma}\right) da$$

with M_A and Σ_A in dB, and $\Gamma = 10\log(2\sigma^2)$, i.e. $\sigma = \sqrt{10^{\Gamma/10}/2}$ $(\gamma = 10^{\Gamma/10})$, is the mean squared value of the multipath component expressed in dB.

The Loo distribution is very practical as it includes, as special cases, the normal and the Rice distribution for large values of a, and the Rayleigh distribution for negligible values of a. As stated earlier, this property makes this distribution valid for a very wide range of shadowing/blockage conditions spanning from line-of-sight (LOS) to deep shadowed cases [31].

It can be observed how the Loo distribution has three parameters: M_A, Σ_A and Γ, all in dB. The first two describe the variations of A while only one parameter, Γ, the average multipath power, is used for the incoherent component. This implies that Γ does not change along the route/flight. This is in contradiction with the observations presented in the previous section.

5.3.2 New time-series generator

A slightly more complex model needs to be introduced to describe variations in the received signal accounting for variations in Γ or, rather, its version in linear units, γ. This requires the introduction of a second Gaussian distribution, i.e.

$$f(\gamma) = \frac{4.3429}{\Sigma_\gamma \gamma \sqrt{2\pi}} exp\left[-\frac{(10\log(\gamma) - M_\Gamma)^2}{2\Sigma_\Gamma^2}\right] \quad \gamma \geq 0 \quad (5.20)$$

One further assumption, supported by observations, is the practical independence between the distributions of A and Γ, thus, the resulting distribution should come from the integration below,

$$f(r) = \int_0^\infty \int_0^\infty f(r|a,\gamma)f(a)f(\gamma)da\,d\gamma = \int_0^\infty \int_0^\infty \exp\left[-\frac{r^2 + a^2}{\gamma}\right] I_0\left(\frac{2ra}{\gamma}\right) ...$$

$$\frac{(\frac{20}{ln10})}{a\Sigma_A\sqrt{2\pi}} \exp\left[-\frac{(20\log a - M_A)^2}{2\Sigma_A^2}\right] \frac{(\frac{10}{ln10})}{\gamma\Sigma_\Gamma\sqrt{2\pi}} \exp\left[-\frac{(20\log \gamma - M_\Gamma)^2}{2\Sigma_\Gamma^2}\right] da\,d\gamma \quad (5.21)$$

The above distribution only deals with amplitudes, however, it is also necessary to reproduce the rates of change in the various parameters. This is accomplished by using several low-pass filters, as shown in the schematic diagram of the time-series synthesizer associated with the model shown in Fig. 5.12. In the diagram there are two main blocks: the top one deals with generating the diffuse component while the bottom block oversees the generation of the direct signal. The outputs of both blocks can be complex; they are

finally added to generate the overall complex envelope. The magnitude of the simulated series can be derived by taking the absolute value.
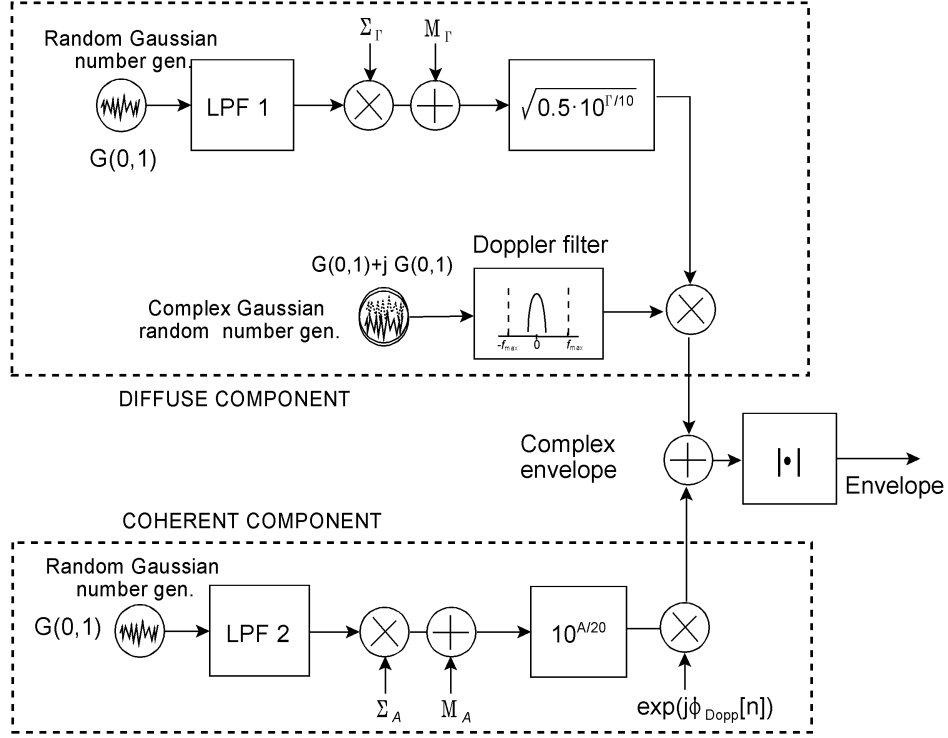

Figure 5.12: Generator scheme

The Doppler shift was introduced in the direct signal branch, which can be calculated from the link geometry since,

$$f_{\text{Doppler}} = (\nu/\lambda)\cos(\xi) \tag{5.22}$$

where ν is the UAV speed, λ is the wavelength and ξ is the angle between the radio path and the direction of flight.

Looking now into the top block, there are two branches: the upper with a Gaussian number generator followed by a low-pass filter (LPF1) implementing the wanted autocorrelation properties. The filter is a sampled and windowed Finite Impulse Response (FIR) version of the required impulse response.

Then, the filtered series was scaled to the adequate mean and standard deviation: M_Γ, Σ_Γ, and converted to linear units using

$$\sigma = \sqrt{\frac{10^{\frac{\Gamma}{10}}}{2}} \tag{5.23}$$

to modulate the modal value, σ, of the Rayleigh generator, in the lower branch in the diffuse component block. The first step when designing the filter is the autocorrelation

function, $\rho_\Gamma(\Delta t)$; its Fourier transform is the power spectral density, $S(f)$. The following assumption can be made [47],

$$H_\Gamma(f) = \sqrt{S_\Gamma(f)} \tag{5.24}$$

Thus, taking the Fourier transform of the correlation function and the square root and transforming back yield:

$$\rho_\Gamma(t) = \exp\left(-\frac{t^2}{2\xi^2}\right) \xrightarrow{\ F\ } S(f) = \xi \exp[-2(a\pi f)^2] \tag{5.25}$$

$$h(t) = \sqrt{2}\exp\left(-\frac{t^2}{\xi^2}\right) \xleftarrow{\ F^{-1}\ } H(f) = \sqrt{S(f)} \tag{5.26}$$

The sampling rate in this branch is also f_s (Hz) as in the case of the Doppler filter. The resulting impulse response is finally windowed using the Hanning window.

The lower branch of the top block is a Rayleigh series generator consisting of a complex Gaussian random number generator, each of its components (in-phase and quadrature) has zero mean and a standard deviation equal to one. The resulting complex signal, generated at a rate f_s (Hz), is filtered by means of a Butterworth filter to reproduce the Doppler spreading caused by multipath. There is no access to complex envelope measurements for computing the Doppler spectrum, however, the expected theoretical spreading from the geometry of the link is rather small, in the order of a few Hz. This means that a very narrow Doppler filter is necessary. The filter was parametrized by trial and error based on the expected Doppler bandwidth and comparing the results with the measurements. The expected Doppler bandwidth is determined by the angular sector between the transmitter and the ring of scatterers around the receiver which, most likely, are located in the same street/square the receiver is in. The radius of this ring of scatterers is much smaller that the Tx-Rx distance.

After filtering, there is a Rayleigh series of modal value equal to one. The wanted modal value is set by multiplying the resulting complex filtered signal by the output of the top branch in the incoherent component block which is a slowly varying log-normal series with Gaussian autocorrelation as discussed in the previous paragraphs.

As with the upper block, the lower block is responsible for reproducing variations in the direct/coherent component which are Gaussian in dB and show Gaussian correlation properties. Again, a filter, LPF2, for introducing the right rate of change in the variations of A must be used. The sampling rate is also f_s (Hz) as in the other branches.

As indicated above, there is an assumption that the variations of A and Γ are uncorrelated in this implementation of the simulator. As shown next, the agreement between synthesized and measured series is quite good. However, for general purposes, a comprehensive synthesizer should be able to force some degree of correlation between the two variables. For the general case where several Gaussian variables must be forced to be partially correlated, the uncorrelated series must be multiplied by the Cholesky decomposition of their cross-correlation matrix as discussed for example in [26] chapter 3. In the case of two Gaussian variables this can be achieved through the transformation

$$\begin{pmatrix} A \\ \Gamma \end{pmatrix} = \begin{pmatrix} M_A \\ M_\Gamma \end{pmatrix} + \begin{pmatrix} \Sigma_A & 0 \\ \Sigma\rho_{A\Gamma} & \Sigma_\Gamma\sqrt{1-\rho_{A\Gamma}^2} \end{pmatrix} \begin{pmatrix} X_1 \\ X_2 \end{pmatrix} \tag{5.27}$$

where X_1 and X_2 are two zero-mean, unit-standard deviation Gaussian, uncorrelated random generators.

5.3.3 Generator validation

Several tests are presented below to illustrate the similarity of the synthesized series first and second-order statistics with respect to those of the original experimental series. The synthesizer parameters were the ones extracted from the measured series used for comparison. In Fig. 5.13 a synthesized series is shown together with the original measured series. In the validation the simulator was run ten times and the corresponding statistics were plotted together with those of the measured series.

Thus, in Fig. 5.14 the CDFs (Cumulative Distribution Functions) are shown for the measured and simulated series. The similarity is quite good down to the tail of the distribution. The effectiveness of the filters introduced in the modeling can be observed by comparing the LCR (level crossing rate) and AFD (average fade duration) plots. These are illustrated in Fig. 5.15 and 5.16, respectively. The deviations between the experimental and synthesized series statistics can be considered to be sufficiently small. Similar fits could be observed for other flights and measurement locations.
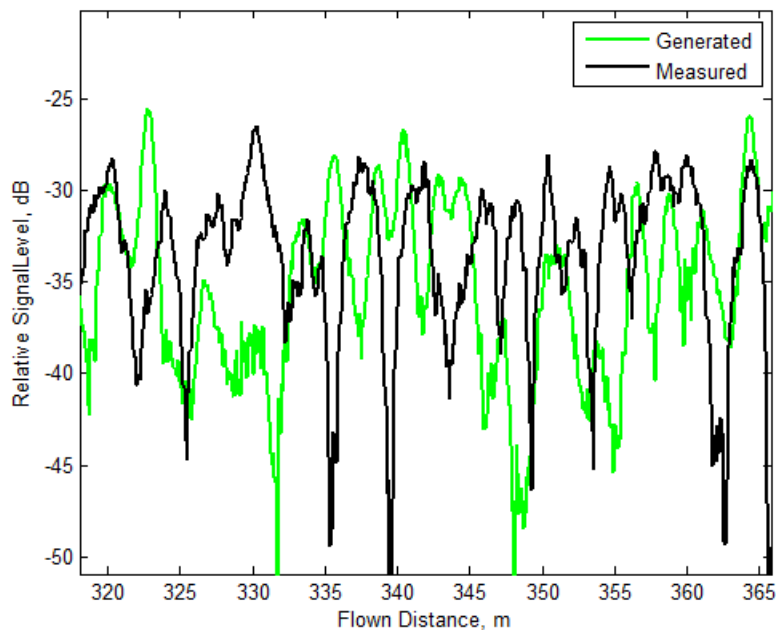

Figure 5.13: Measured and simulated series ("location #1", flight #3).
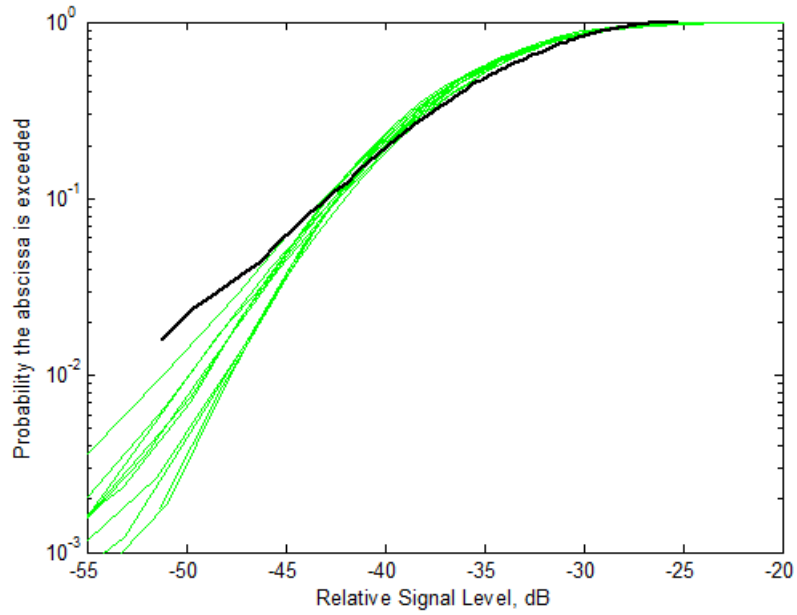
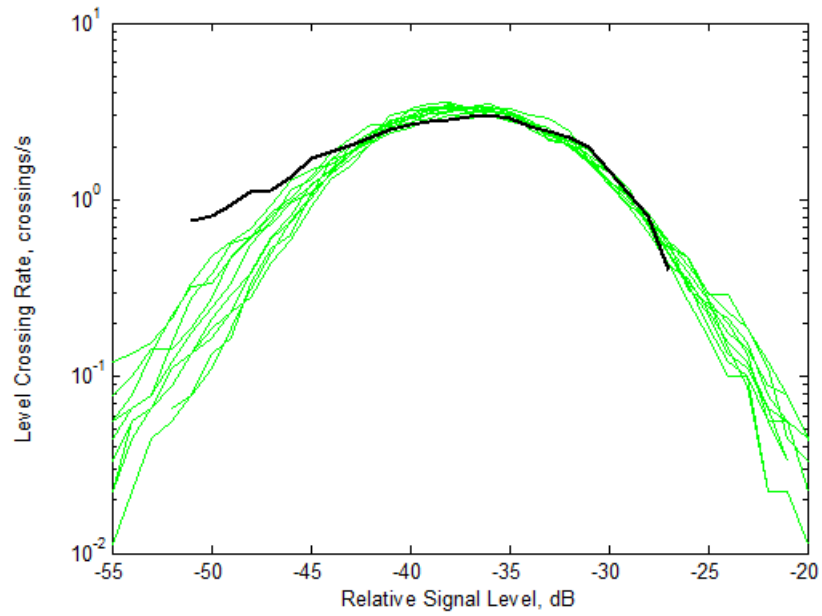Figure 5.14: CDFs of measured and ten simulated series ("location #1", flight #3).

Figure 5.15: LCR curves of measured and ten simulated series ("location #1", flight #3).
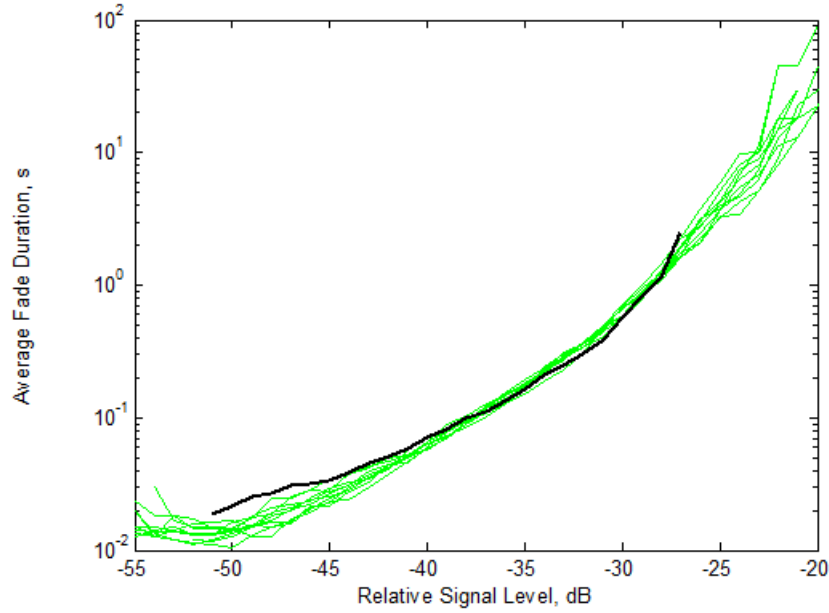
Figure 5.16: AFD curves of measured and ten simulated series ("location #1", flight #3).

It must be noted that, in this comparison exercise, it is quite difficult to achieve a perfect match when two phenomena (shadowing and multipath fading) are involved with completely different rates of change and dynamic ranges. To achieve statistical stability in the diffuse part, only small route recordings are necessary. However, for the larger scale, shadowing related variations, an extremely long observation time is needed, which is not totally achieved in the measured data when low probability levels are concerned. This can be seen, for example, in the synthesized series for probability levels slightly below 0.1. Thus, the comparison or goodness of fit can only be verified in subjective terms.

5.4   Conclusions

In this chapter a statistical analysis of the narrow-band UAV propagation channel in urban areas is presented. This is a special link between the purely terrestrial and the land mobile satellite, LMS, channel whose dynamic characteristics are close to those found in the so-called "bad state" of the LMS channel.

Possible modeling of signal variations by the Loo model, commonly employed in satellite links, was analyzed. Several differences occurred in the UAV case, especially regarding the assumption in satellite link modeling of a constant power of the multipath component. Moreover, this parameter was observed to change at a different rate than the direct component.

Results from a statistical analysis, i.e., the model parameters are provided and a time-series synthesizer has been developed implementing the observations from the analysis with sufficiently good fits found between the synthetic and measured time-series. The complete analysis, with time series generator, was published in [43].

Chapter 6

Space diversity

After analyzing the low elevation link propagation channel and developing path-loss and channel models, how to enhance the link and mitigating fades caused by propagation through environment became the focus. Similarly, as in the case of path-loss and channel modeling, the possibilities of using known methods were considered. In this work a space diversity method was chosen as it can be effective in an urban area.

A study of usability of space diversity was based on measurements conducted for a channel model in an urban area (chapter 5). Several parameters determining the usefulness were derived and analyzed.

6.1 Data processing

The processing of received power data was similar as in chapter 5, however, signals from all four channels were used here: First, the free space level was subtracted from the measured received power series for computing the excess path gain, the inverse of the excess loss. Then, the excess path gain was converted to linear units (normalized received voltage or signal envelope) for performing signal combining. The combining was performed ad post in Matlab environment. After combining, the resulting envelopes were converted back to logarithmic units for further analysis.

Three combining methods were tested: selective combining (SC); Maximal Ratio Combining (MRC); Equal Gain Combining (EGC). The resulting envelope is denoted by r_0 and the individual branch envelopes are denoted by r_i as in section 2.5.3.

6.2 Results

In this section measurement results are presented together with an analysis quantifying the values of diversity gain achievable with the setup used. For illustrative purposes "location #3", flight #3 was chosen, i.e. an elevation angle of 4 deg. with the receiver located at the open square in Fig. 5.2, quite close to the buildings in the direction of the transmitter. A priori, the main difference with the other two locations could be extra, smaller multipath contributions from the opposite side which may be missing at this site with respect to the others. Ultimately, no significant differences were observed between sites. Fig. 6.1 shows a 30 m section of the 2 km flight illustrating the variations in the received signal picked up by each of the four diversity branches. The figure plots

several very wide arches in the signal which correspond to varying shadowing conditions, e.g. features on the rooftops, but also to multipath. This is consistent with the very low Doppler spreading present. Superposed on the arches, weaker and faster variations can be observed. The excess path gain oscillates at an average value somewhere between -30 and -25 dB. This corresponds to deep diffraction conditions due mainly to the rooftop-to-street level loss but also includes some diffraction contributions from the rooftops overflown by the radio path.
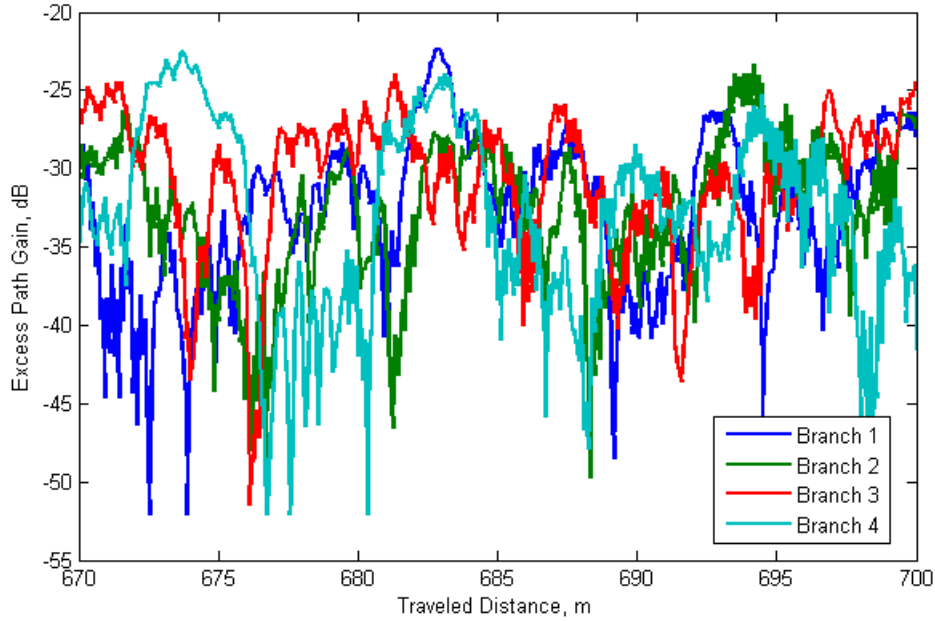

Figure 6.1: Section of 30 m of the 2 km flight #3 and "location #3"

The cumulative distribution functions, CDFs, for the individual diversity branches are presented in Fig. 6.2. From the figure it can be observed how the four branches show quite well-balanced distributions with differences not exceeding 2.5 dB. This is one of the two requirements for achieving significant diversity gains. The other requisite is low cross-correlations. Thus, the correlation between the signal envelopes in the four branches were also analyzed, both in linear and logarithmic units, yielding

$$p = \begin{bmatrix} 1.00 & 0.18 & 0.09 & 0.02 \\ 0.18 & 1.00 & 0.15 & 0.03 \\ 0.09 & 0.15 & 1.00 & 0.06 \\ 0.02 & 0.03 & 0.06 & 1.00 \end{bmatrix} \tag{6.1}$$

$$P = \begin{bmatrix} 1.00 & 0.13 & 0.06 & 0.01 \\ 0.13 & 1.00 & 0.10 & 0.02 \\ 0.06 & 0.10 & 1.00 & 0.07 \\ 0.01 & 0.02 & 0.07 & 1.00 \end{bmatrix} \tag{6.2}$$
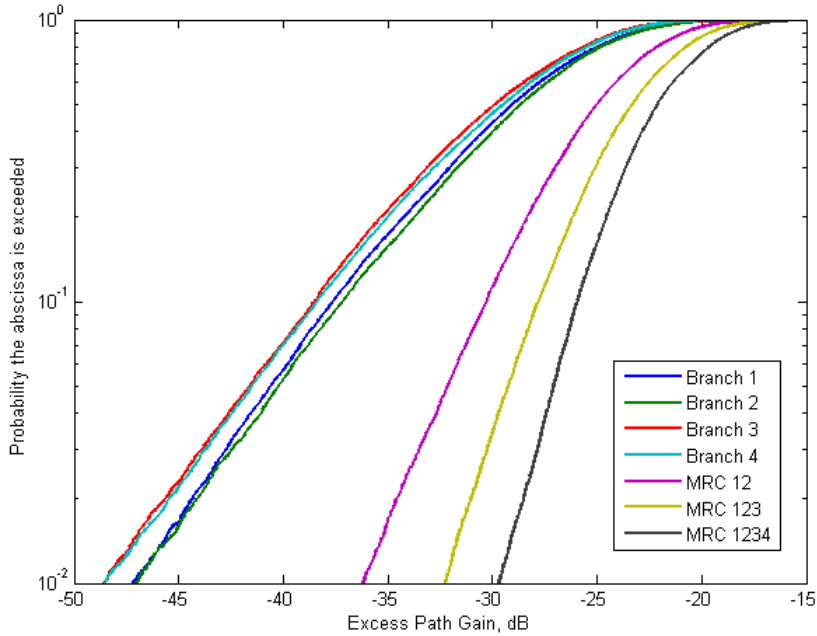
Figure 6.2: CDFs of original series and of incrementally MRC-combined signals.

It is clear that the four envelopes are low correlated, promising significant diversity gains. Fig. 6.3 shows the incremental gains achieved by plotting the envelope time-series corresponding to the same section of data as in Fig. 6.1 for branch-1 and the combination of 1 and 2, 1 through 3 and 1 through 4. Note that the series are normalized with respect to their RMS level (mean power).The order in which the incremental gain was evaluated was by using branches 1 and 2, 1 through 3 and 1 through 4. The results should not change significantly if another order was chosen given the small differences in their CDF.

Also in Fig. 6.2 the CDFs for two- to four-branch MRC space diversity are shown, computed using the expressions discussed in the previous section. The combined signal statistics show substantial incremental gains with higher median values and higher levels, especially for the very low probability levels of exceedance. It is clear, as expected, that the main improvement is achieved when the first diversity branch is introduced and then, a law of diminishing returns is observed when new additional branches are introduced.
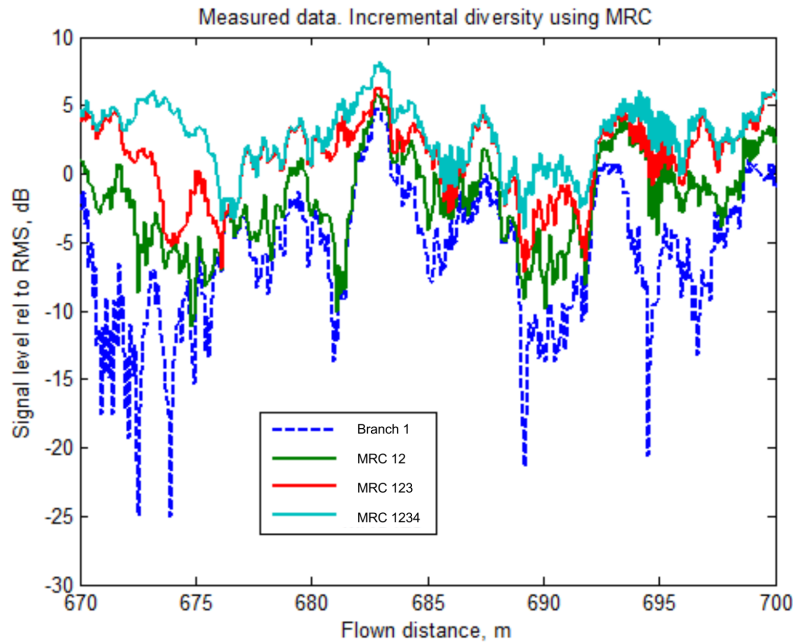
Figure 6.3: Normalized (with respect to RMS level) series in branch-1 and in incrementally MRC-combined series.

Further work regarding the evaluation of the diversity gain was performed on the measured series normalized with respect to their RMS level. Moreover, the normalized series were fitted to a Rayleigh distribution. In Fig 6.4 the CDFs of the normalized envelope in branch 1 can be found and that of the successive incremental combinations. In the current case (flight and location) the fit was quite good indicating that the much more favorable Rice character found for higher elevations corresponding to mobile-satellite links [48] did not fully describe the link. This was the case for all flights and locations. The Rayleigh distribution satisfactorily explains the large-scale behavior of the signal. However, the small-scale, or the details, in the measured signal are somewhat different as was found in the analysis described in previous chapter.

Significant improvements are seen as new branches are introduced to the combiner. At the 0.01 probability level (1%) a gain exceeding 10 dB is obtained for two-branch diversity.
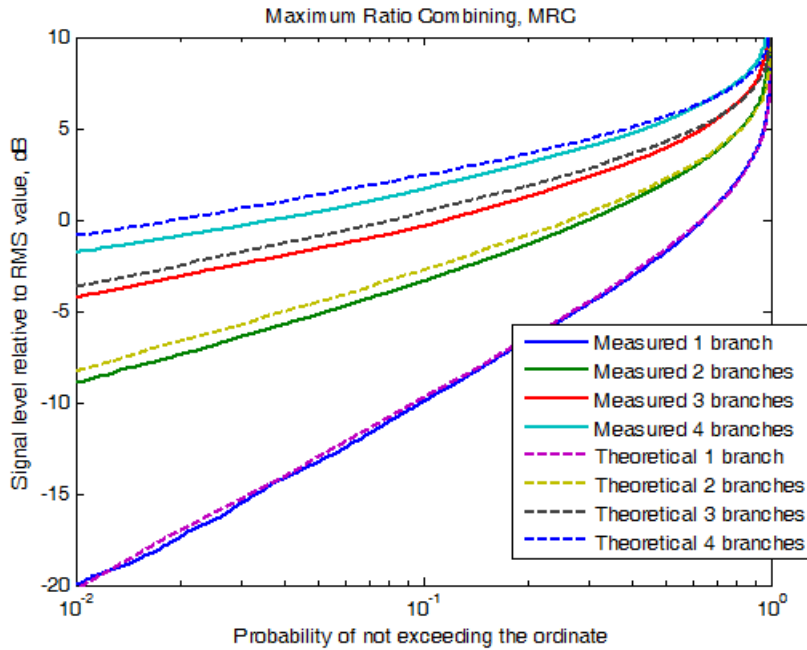
Figure 6.4: Measured and uncorrelated Rayleigh model CDFs for rms level normalized series corresponding to one banch and incremental 4-branch diversity plus MRC.

For reference, a comparison of the measured and predicted (assuming uncorrelated Rayleigh branches) diversity gains is also present [14].

The diversity gain is defined as the dB difference for equal probability levels between the CDF of an individual branch and that of the combined signals.

The received signals were normalized with respect to their rms level and their CDFs compared with those predicted for a Rayleigh fading with rms level equal to one. Fig. 6.4 shows the CDFs for normalized measured and combined signals and those corresponding to the Rayleigh model. The agreement is quite good for the individual signals but shows small differences for the combined signals. From the results presented in Fig. 6.4, the incremental diversity gains assuming MRC are explicitly shown in Fig. 6.5. As expected, the largest increment is achieved when introducing the first diversity branch. Further branches bring about smaller increments but, still, substantial ones, e.g. for the 1% probability level the possible gain is about 12 dB when diversity is introduced and this is incremented to about 18 dB when four branches are used. In the figure the deviation from the uncorrelated Rayleigh fading case are also illustrated , indicating, as mentioned, that the Rayleigh distribution does not explain the overall behavior of the channel.
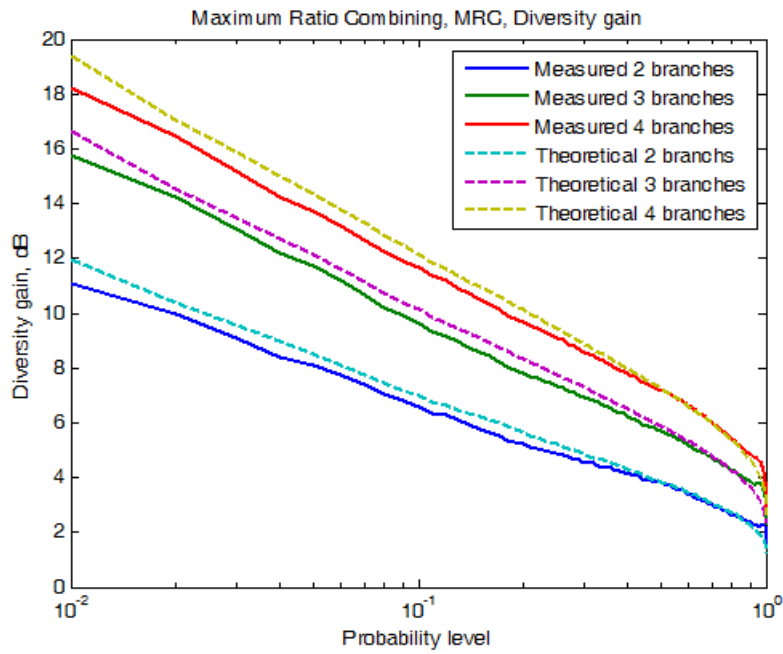
Figure 6.5: Measured and uncorrelated Rayleigh model 4-branch incremental diversity gains with MRC.

In Figs. 6.6 and 6.7 the CDFs and the diversity gains obtained for SC, EGC and MRC for four-branch diversity are shown, together with the predictions from the Rayleigh model, indicating a minor improvement obtained with MRC with respect to EGC and SC at the expense of the needed additional complexity
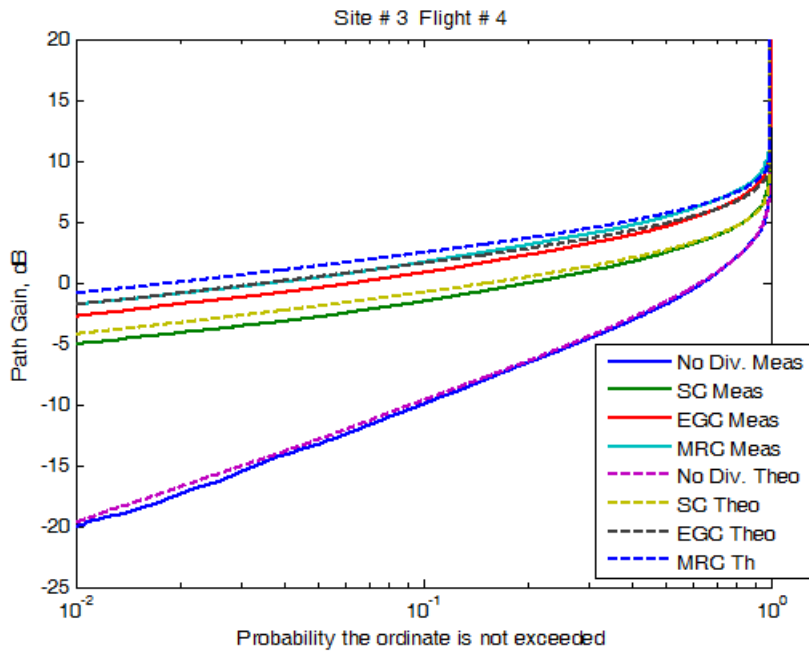
Figure 6.6: Measured and uncorrelated Rayleigh model CDFs for 4-branch diversity and SC, EGC and MRC combining. Signals normalized with respect to rms level.
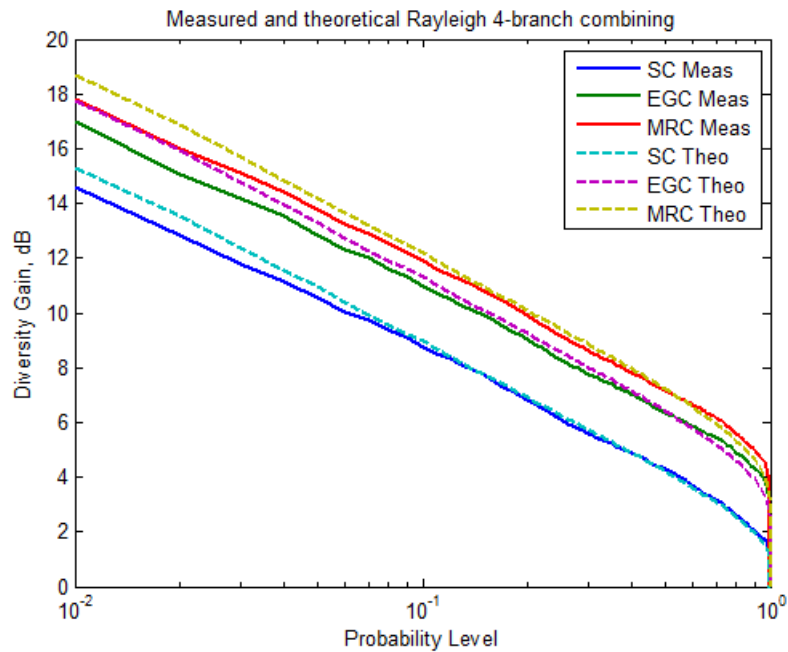

Figure 6.7: Measured and uncorrelated Rayleigh model diversity gains for 4-branch diversity and SC, EGC and MRC combining. Signals normalized with respect to rms level.

The observed behavior, diversity-wise, was similar for all elevations and locations. As for the average received power this only increases marginally with the elevation angle in

an approximately 5 dB range.

Further, the implications of using diversity on a second-order statistic, the average fade duration, AFD were briefly analyzed . The durations were expressed in length of flight units and normalized then with respect to wavelength. In Fig. 6.8 the afds for branch-1 and for the incrementally combined signals from 1 through 4 are shown. Also, the afd for a Rayleigh channel with Clarke Doppler spectrum [14] is shown for reference. It is clear that, in our case, the signal variations are much slower than in the Clarke case given that the Doppler spectrum is much narrower. The introduction of MRC combining results in fades of shorter duration; this helps reduce the length of the codewords and/or interleaver depths necessary to overcome the deep and long fades encountered.
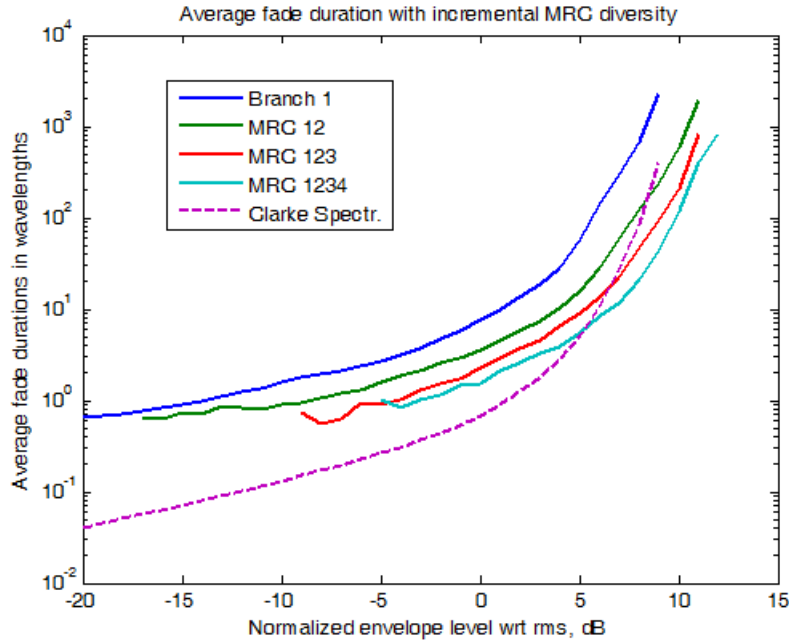

Figure 6.8: Theoretical Rayleigh + Clarke Doppler spectrum AFD, and AFD of experimental single branch and 4-branch incremental MRC.

Also, in Fig. 6.9 the level crossing rate, LCR, in crossings per wavelength is presented for a single branch and various incremental levels of MRC diversity. The LCR is much smaller than that of Clarke's theoretical model (also in the figure). The introduction of incremental diversity gradually shifts the maximum toward higher levels, indicating the reduction in the fade depths brought about by diversity.

The results from this analysis were compared with the results from preliminary experiment in wooded area where the diversity gains achieved are lower but still substantial. This comparison was published in [49].
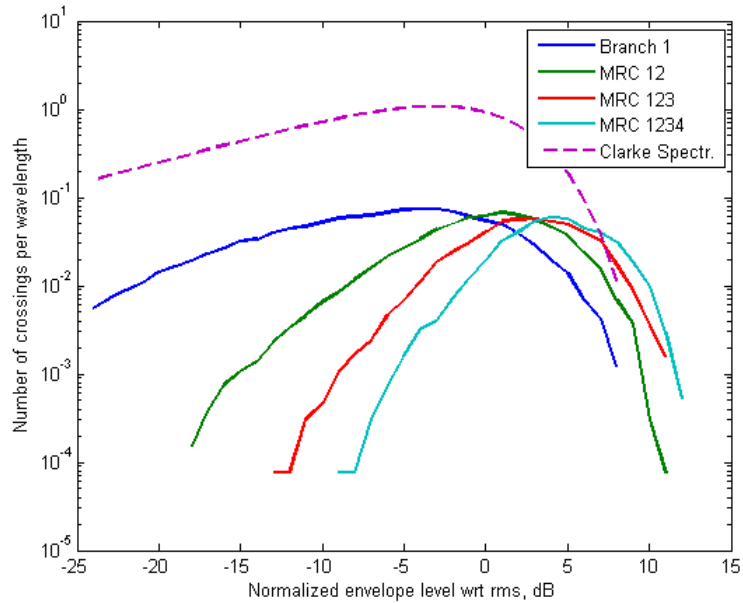
Figure 6.9: Theoretical Rayleigh + Clarke Doppler spectrum LCR, and LCR of experimental single branch and 4-branch incremental MRC

6.3   Conclusions

A quantification of the space diversity gain for low elevation links in urban areas has been presented. The analysis results show that significant gains are possible, especially for the low outage probability levels, though slightly smaller than those obtained for uncorrelated Rayleigh fading channels. The fades are also quite long in duration due to the noticeably low Doppler spread present; this is also partially overcome by the use of diversity as shown in the calculated reductions in the average fade durations. The diversity gain was found not to be significantly dependent on the elevation angle, the street orientation or the street width.

The analysis was presented and published in [50][51].

Chapter 7

Conclusions

UAV systems are nowadays finding the place in many surveillance missions. For developing and testing such systems, modeling and analyzing the link between the UAV and ground receiver station is needed. The link has a geometry different from any satellite or terrestrial system in use, consequently, this does not provide a suitable solution. A full study of loss mechanisms and link statistical characteristics has to be performed and new models have to be developed, based on propagation modeling knowledge, to suit UAV applications properly.

In this work analytical and modeling methods from satellite and terrestrial links were studied and their suitability for UAV links was discussed. Specifically chosen methods and their approximations were then adapted for UAV link specifications. For this purpose a series of measurements was conducted with an unmanned airship as a UAV and a four-channel receiver on the ground. An urban environment was chosen for the modeling and analysis as the large number of obstacles and scatterers are central to the study.

Based on the methods and approximations in correlation with a measurement comparison a new path-loss model was developed. The model uses the Fresnel Integrals approximation of diffraction on the last building before the receiver. The building shape was approximated as two knife-edges on the wall. The influence of other buildings and their rooftops was found to be negligible. The propagation in the street was modeled by a two-ray approach where one ray is direct from the last obstacle and the second is reflected from the rear building. Influence from other rays was also found to be negligible. The model was validated after comparing measurements and the developed path-loss model was published in [38].

A statistical analysis of received signal was next performed. It was found that the amplitudes are Rice distributed and the Loo model was studied for possible usage. Unlike in the Loo model, the average multipath power was observed to be independent of mean power of the direct component and varies randomly. The Doppler spread was also found to be quite narrow due to low angular changes in geometry with transmitter movement. All mechanisms were set together and a new time-series generator was developed and validated by statistical comparison with the measured data. The analysis and new time-series generator were published in [43].

After characterizing the link by means of average path-loss and fade statistics, a study of link enhancement possibilities was conducted. A four-channel space diversity was tested in the urban area and the enhancement quantified by diversity gain value. It was concluded that the channel is low correlated and significant gains can be achieved.

Based on the results it can be stated that the objectives of this work were accomplished. As the main contribution the two new propagation models were developed for planning UHF narrow-band low elevation links between a slow speed UAV and a nomadic user in an urban area.

However, this work is only the first step in the area of UAV link propagation modeling. In this work only one frequency was used, whereas higher frequencies may satisfy higher demands on data rate (for higher resolution or frame speed of video). The usage of higher frequencies raises the need for new models and even new measurements as the propagation in this studied environment is highly frequency dependent. Another method of data rate extension is wide-band link where a completely new analysis will be necessary.

In this work space diversity possibilities were studied for a SIMO type of link. However, other diversity techniques polarization, frequency, angle diversity etc. should be studied together with a full MIMO type of link using the latest research in the MIMO area for satellite and terrestrial links.

The scenario tested represents a worst-case scenario in a Central European city center. Many applications will need a model useful in other types of city and other building densities. Another study is needed on determining the type of UAV where faster movement can provide tactical and safety advantages while changing the amount of Doppler shift will increase demand for new analyses. The position of the receiver, where a receiver in motion can alas provide safety and time-saving advantages is another avenue to explore in the future. Many improvements and deeper analysis must continue to be done on this type of link as occurred in the last fifty years with research done on satellite and terrestrial links for various applications and technologies.

At this moment there is a lack of legislation for using the UAV for commercial purposes in Czech Republic. However, in non-commercial areas the UAV more often covers surveillance missions and if, in the future, UAV traffic is opened, the need for propagation modeling will significantly increase.

Bibliography

[1] H. Al-Helal and J. Sprinkle. UAV Search : Maximizing Target Acquisition. *17th IEEE International Conference and Workshops on Engineering of Computer-Based Systems*, pages 9 – 18, 2010.

[2] G. Zhou and D. Zang. Civil UAV System for Earth Observation. In *Geoscience and Remote Sensing Symposium IGARSS*. IEEE International, 2007.

[3] L. Peng and Q. Geng. Real-time simulation system for UAV based on Matlab/Simulink. In *IEEE 2nd International Conference on Computing, Control and Industrial Engineering (CCIE)*, volume 1, 2011.

[4] C. Cerasoli. An analysis of unmanned airborne vehicle relay coverage in urban environments. In *Military Communications Conference*. MILCOM 2007, 2007.

[5] J. Romeu, A. Aguasca, J. Alonso, S. Blanch, and R. R. Martins. Small UAV radiocommunication channel characterization. In *Proceedings of the Fourth European Conference on Antennas and Propagation (EuCAP)*, 2010.

[6] H. Bertoni. *Radio Propagation for Modern Wireless Systems*. Prentice Hall PTR, 2000.

[7] P. Pechac and S. Zvanovec. *Zaklady sireni vln pro planovani pozemnich radiovych spoju*. BEN Technicka Literatura, 2007.

[8] M. Ait-Ighil, F. P. Fontan, J. Lemorton, F. Lacoste, G. Artaud, C. Bourga, and M. Bousquet. A three components model for simplified building scattering in urban environment. In *6th European Conference on Antennas and Propagation (EUCAP)*, pages 2449–2453, 2012.

[9] George T. Ruck, editor. *Radar cross section handbook*. Plenum Press, 1970.

[10] L. Barclay. *Propagation of Radiowaves*. IEE, 2nd edition, 2003.

[11] ITU-R P.526-11. Propagation by diffraction. 2009.

[12] W. C. Y. Lee. *Mobile Cellular Telecommunications*. McGraw-Hill, Inc., 2nd edition, 1995.

[13] L. E. Vogler. The attenuation of electromagnetic waves by multiple knife-edge diffraction. Technical Report PB82-139239, National Technical Information Service, Springfield V A., 1981.

[14] J. Parsons. *Mobile Radio Propagation Channel*. Wiley, 2nd edition, 2000.

[15] S. Saunders and A. Zavala. *Antennas and propagation for wireless communication systems*. Wiley, 2nd edition, 2007.

[16] D. J. Cichon and T. Kurner. Propagation Prediction Models, Chapter 4. Technical report, COST 231 final report, 1999.

[17] V. Erceg, L. Greenstein, S. Tjandra, S. Parkoff, A. Gupta, B. Kulic, A. Julius, and R. Bianchi. An Empirically Based Path Loss Model for Wireless Channels in Suburban Environments. *IEEE Journal on selected areas in Communications*, 17(7):1205–1211, 1999.

[18] F. Ikegami, S. Yoshida, T. Takeuchi, and M. Umehira. Propagation Factors Controlling Mean Field Strength on Urban Streets. *IEEE Transactions on Antennas and Propagation*, 32(8):822–829, 1984.

[19] J. Walfish and H. Bertoni. A theoretical model of UHF propagation in urban environments. *IEEE Transactions on Antennas and Propagation*, 36(12):1788–1796, 1988.

[20] ITU-R P.1057-1. Probability distributions relevant to radiowave propagation modelling. 1994 - 2001.

[21] M. Patzold. *Mobile Radio Channels*. Wiley, 2nd edition, 2012.

[22] H. Suzuki. A statistical model for urban radio propagation. *IEEE Transactions on Communications*, com-25(7):673 – 680, 1977.

[23] Ch. Loo. A statistical model for a Land Mobile Satellite Link. *IEEE Transactions on Vehicular Technology*, vt-34(3):122 – 127, 1985.

[24] G. E. Corazza and F. Vatalaro. A Statistical Model for Land Mobile Satellite Channels and Its Application to Nongeostacionary Orbit Systems. *IEEE Transactions on Vehicular Technology*, 43(3):738 – 742, 1994.

[25] S. H. Hwang, K. J. Kim, J. Y. Ahn, and K. Ch. Whang. A Channel Model for Nongeostationary Orbiting Satellite System. In *Vehicular Technology Conference IEEE*, 1997.

[26] F. P. Fontan and P. E. Marino. *Modelling the Wireless Propagation Channel. A simulation approach with Matlab*. Wiley, 2008.

[27] C. D. Iskander. A MATLAB -based Object-Oriented Approach to Multipath Fading Channel Simulation. *Hi-Tek Multisystems*, pages 1 – 15, 2008.

[28] R. H. Clarke. A statistical theory of mobile radio reception. *Bell System Technical Journal*, 47:957 – 1000, 1968.

[29] J. Gans. Apower-spectral theory of propagation in the mobile radio environment. *IEEE Transactions on Vehicular Technology*, 21:27 – 38, 1972.

[30] D. C. Cox. Delay Doppler characteristics of multipath propagation at 910 MHz in a suburban mobile radio environment. *IEEE Transactions on Antennas and Propagation*, ap-20:625 – 635, 1972.

[31] Fernando P. Fontan, A. Mayo, D. Marote, R. Prieto-Cerdeira, P. Marino, Fernando D. Machado, and N. Riera. Review of Generative Models for the Narrowband Land Mobile Satellite Propagation Channel. *International Journal of Satellite Communications*, 26:291–316, 2008.

[32] F. P. Fontan, J. P. Gonzales, M. J. Ferreiro, and M. A. Castro. Complex Envelope Three-State Markov Model based simulator for the Narrow-band LMS Channel. *International Journal of Satellite Communications*, 15:1–15, 1997.

[33] ITU-R P.681-6. Propagation data required for design of Earth-space land mobile telecommunications systems. 1990-2003.

[34] E. Lutz, D. Cygan, M. Dippold, F. Dolainsky, and W. Papke. The Land Mobile Satellite Communication Channel - Recording, Statistics, and Channel Model. *IEEE Transactions on Vehicular Technology*, 40(2):375 – 386, 1991.

[35] Y. Karasawa, K. Kimura, and K. Minamisono. Analysis of Availability Improvement in LMSS by Means of Satellite Diversity Based on Three-State Propagation Channel Model. *IEEE Transactions on Vehicular Technology*, 46(4):1047 – 1056, 1997.

[36] J. F. V. Valdez, M. A. G. Fernandez, A. M. M. Gonzales, and D. S. Hernandez. The Role of Polarization Diversity for MIMO Systems Under Rayleigh-Fading Environments. *IEEE Antennas and Wireless Propagation Letters*, 5:534 – 536, 2006.

[37] P. L. Perini and C. L. Holloway. Angle and space diversity comparisons in different mobile radio environments. *IEEE Transactions on Antennas and Propagation*, 46:764 – 775, 1998.

[38] M. Simunek, P. Pechac, and F. P. Fontan. Excess Loss Model for Low Elevation Links in Urban Area for UAVs. *Radioengineering*, 20(3):561–568, 2011.

[39] www.airshipclub.com.

[40] geoportal.cuzk.cz.

[41] S. Saunders and F. Bonar. Explicit Multiple Building Diffraction Attenuation Function for Mobile Radio Wave Propagation. *Electronics Letters*, 27(14):1276–1277, 1991.

[42] J. H. Whitteker. FresnelKirchhoff theory applied to terrain diffraction problems. *Radio Science*, 25(5):837–851, 1990.

[43] M. Simunek, F. P. Fontan, and P. Pechac. The UAV Low Elevation Propagation Channel in Urban Areas: Statistical Analysis and Time- Series Generator. *IEEE Transactions on Antennas and Propagation*, 61(7):3850 – 3858, 2013.

[44] L. Greenstein, D. Michelson, and V. Erceg. A Moment-Method Estimation of the Ricean K-Factor. *IEEE Communications Letters*, 3(6):175–176, 1999.

[45] F. Ikegami and S. Yoshida. Analysis of multipath propagation structure in urban mobile radio environments. *IEEE Transactions on Antennas and Propagation*, ap-28(4):531–537, 1980.

[46] L. E. Braten and T. Tjelta. Semi-Markov multistate modeling of the land mobile propagation channel for geostationary satellites. *IEEE Transactions on Antennas and Propagation*, ap-50(12):1795 – 1802, 2002.

[47] D. Young and N. Beaulieu. The Generation of Correlated Rayleigh Random Variates by Inverse Discrete Fourier Transform. *IEEE Transactions on Communications*, 48(7):1114 – 1127, 2000.

[48] R. P. Cerdeira, F. P. Fontan, P. Burzigottil, A. B. Alamanax, and I. S. Lago. Versatile two-state land mobile satellite channel model with first application to DVB-SH analysis. *International Journal of Satellite Communications Networking*, 28:291 – 315, 2010.

[49] M. Simunek, P. Pechac, and F. P. Fontan. Feasibility of UAV Link Space Diveristy in Wooded Areas. *International Journal of Antennas and Propagation*, 2013.

[50] M. Simunek, P. Pechac, and F. P. Fontan. Space Diversity Analysis for Low Elevation Links in a Urban Area. In *6th European Conference on Antennas and Propagation (EUCAP)*, 2012.

[51] M. Simunek, F. P. Fontan, P. Pechac, and F. J. D. Otero. Space Diversity Gain in Urban Area Low Elevation Links for Surveillance Applications. *IEEE Transactions on Antennas and Propagation*, 2013 submitted.